ABSTRACT

Title of dissertation: Proton and Helium Spectra from the First Flight of the CREAM Balloon-Borne Experiment

Young Soo Yoon, Doctor of Philosophy, 2010

Dissertation directed by: Professor Eun-Suk Seo
Department of Physics and
Institute for Physical Science and Technology

Cosmic-ray proton and helium spectra have been measured with the balloon-borne Cosmic Ray Energetics And Mass (CREAM) experiment flown for 42 days in Antarctica in the 2004-2005 austral summer season. High-energy cosmic-ray data were collected at an average altitude of ∼38.5 km with an average atmospheric overburden of ∼3.9 g/cm^2. Individual elements are clearly separated with a charge resolution of ∼0.15e (in charge units) and ∼0.2e, respectively, for protons and helium nuclei. The measured spectra at the top of the atmosphere are represented by a power law with a spectral index of -2.66 ±0.02 for protons from 2.5 TeV to 250 TeV and -2.58 ±0.02 for helium nuclei from 630 GeV/nucleon to 63 TeV/nucleon. The measured proton and helium spectra are harder than previous measurements at a few tens of GeV/nucleon. Possible explanations of this spectral hardening could be the effect of a relatively nearby source or the effect of spectral concavity caused by interactions of cosmic rays with the accelerating shock. The helium flux is higher than that expected from extrapolation of a power-law fit to the lower-energy data.

The relative abundance of protons to helium nuclei is about 8.8 $\pm$0.5 in the range from 2.5 TeV/nucleon to 63 TeV/nucleon. In this thesis, the analysis of proton and helium spectra will be discussed.

Proton and Helium Spectra from the First Flight of the CREAM Balloon-Borne Experiment

by

Young Soo Yoon

Dissertation submitted to the Faculty of the Graduate School of the
University of Maryland, College Park in partial fulfillment
of the requirements for the degree of
Doctor of Philosophy
2010

Advisory Committee:
Professor Eun-Suk Seo, Chair/Advisor
Dr. Frank McDonald
Professor Douglas C. Hamilton
Professor Jordan Goodman
Professor Michael A. Coplan

Acknowledgments

First of all, I heartly thank my advisor, Professor EunSuk Seo, the principle investigator of the CREAM project, for her guidance and support throughout my graduate work. She gave me not only various opportunities participating in this exciting experiment, but also invaluable lessons in many aspects as a researcher. Without her support and supervision, I could not have accomplished my thesis.

I would like to acknowledge the members of my dissertation committee, Dr. Frank McDonald, Prof. Michael Coplan, Prof. Douglas Hamilton, and Prof. Jordan Goodman for their time and efforts to review my thesis and invaluable comments.

I like to thank former and current Cosmic Ray Physics Group members who worked with me, for teaching me lots of the lessons and instructions. I thank especially Hoseok Ahn for pointing me in the right directions during my analysis whenever I was in trouble; Moohyun Lee for all the lessons about calorimeter physics, principles, and calibrations; Sonny Zinn for showing me how to design programs and organize a project; Opher Ganel for ways of expressions and other lessons such as interaction fractions; Ramin Sina for helpful discussions and lessons about theoretical backgrounds; Jayoung Wu for supporting Monte Carlo simulations; Munhwa Kim for helpful discussions about statistical approaches; SangEun Lee, Sangsu Ryu and Joonhyuk Yoo for helpful discussions in various aspects; Larry Lutz for all the support related to electronics and test setups; Peter Walpole for care and support during CREAM-III integration; Sasha Malinine for support during the beam test; Oluchi Ofoha for reviewing my articles; and Azzi Haque for technical support

and various information. I thank all other members and undergraduate students who worked together at the lab, Prashant Bhoyar, ChinKyung Chang, Jihye Han, Sangkyo Han, George He, Tagil Kang, Chanho Kim, Kichun Kim, Thomas Kim, Hongqiang Zhang. I also thank visiting professors, Hongjoo Kim and Kyungdal Choi for invaluable lessons, discussion, and lots of advice in many aspects.

I thank all the CREAM collaboration members for achieving successful flights of CREAM and supporting my work and paper preparations, Michel Buénerd, Stephane Coutu, Laurent Derome, Mike DuVernois, Scott Nutter, Il Park, the late Simon Swordy, Scott Wakely, Jongman Yang and other collaborators. I thank Linda Thompson, Daivd Stuchlik, Robbi Estep and David Pierce for their hospitality and supports at Wallops, VA. I thank Vernon Jones for care and helps during the last three International Cosmic Ray Conferences in 2005, 2007, and 2009.

During my stay in Maryland, I have had supported from friends and seniors, Kiyong Kim, Hanhee Paik, Min-Young Kim, Sejin Han, Young-Noh Yoon, Zaeill Kim, Hana Hwang, Hyeokshin Kwon, Chaun Jang, Doojin Kim, Dohun Kim, Ken Hsieh and Jungto people. Specially, I thank Junghwan Kim and Prof. Young-Suh Kim for long-lasted supports and advice since my arrival, and Jonghee Lee for sincere friendship and guidance throughout my stay.

I acknowledge all my teachers and mentors from the early days. Last, I deeply thank my parents and sister for everything.

This work was supported by NASA Headquarters under the NASA Earth and Space Science Fellowship Program - Grant NNX07AN54H.

Table of Contents

List of Tables

List of Figures

List of Abbreviations

λ_I	Nuclear interaction length
A	Atomic mass of a particle
ADC	Analog to Digital Conversion
AMS	Alpha Magnetic Spectrometer
ASIC	Application Specific Integrated Circuits
ATIC	Advanced Thin Ionization Calorimeter
BESS	Balloon-borne Experiment with Superconducting Spectrometer
CAL	Calorimeter
CANGAROO	Collaboration of Australia and Nippon for a GAmma Ray Observatory in the Outback
CAPRICE	Cosmic AntiParticle Ring Imaging Cherenkov Experiment
CD	Cherenkov Detector
CDAQ	CREAM Data Acquisition
CERN	European Organization for Nuclear Research
CREAM	Cosmic Ray Energetics And Mass
CRN	Cosmic Ray Nuclei detector
DAC	Digital to Analog Conversion
GOES	Geostationary Operational Environmental Satellites
HEAO-3	High Energy Astronomy Observatory-3
HDS	Hodoscope
HPD	Hybrid Photo-Diode
HV	High Voltage
JACEE	Japanese-American Collaborative Emulsion Experiment
kbps	Kilobits per second
LDB	Long Duration Balloon
LEAP	Low Energy AntiProton
LED	Light Emitting Diode
MC	Monte Carlo
MIP	Minimum Ionization Particle
PMT	Photo-Multiplier Tubes
RMS	Root Mean Square
RQMD	Relativistic Quantum Molecular Dynamics
RUNJOB	RUssia-Nippon JOint Balloon experiment
SCD	Silicon Charge Detector
SFC	Science Flight Computer
SN	Supernova
SNR	Supernova Remnant
STV	Sparsification Threshold Value

TCD	Timing Charge Detector
TDC	Time-to-Digital Converter
TDRSS	Tracking and Data Relay Satellite System
TRACER	Transition Radiation Array for Cosmic Energetic Radiation
TRD	Transition Radiation Detector
ULDB	Ultra Long Duration Balloon
X_0	Radiation length
Z	Atomic number of a particle

Chapter 1

Introduction

1.1 Overview

Cosmic rays, energetic nuclei and electrons, are the product of energetic processes in the universe, and their interactions with matter and fields are the source of much of the diffuse gamma-ray, X-ray, and radio emissions that are observed. Cosmic rays were discovered by V. Hess in 1912 [1]. Prior to the development of high-energy particle accelerators, cosmic rays were the only source of high-energy particles. The study of cosmic rays and their interactions with the atoms of the atmosphere resulted in many new discoveries including the positron and muon. Furthermore, research on cosmic rays has been a source for solving astrophysical questions related to cosmic ray origin, acceleration, and propagation mechanisms.

Cosmic rays are distinguished by their sources, such as solar energetic particles, anomalous cosmic rays, galactic cosmic rays, and extragalactic cosmic rays. Solar energetic particles are nuclei and electrons accelerated in association with solar flares, which were first measured by Forbush in 1942 [2, 3]. Anomalous cosmic rays are ionized interstellar neutral particles streaming into the solar system, which were found in the enhanced helium, oxygen, and nitrogen intensities by Garcia-Munoz *et al.* (1973), McDonald *et al.* (1974), and Hovestadt *et al.* (1973) [4–6]. Once ionized, the charged particles are then swept out of the solar system by the solar wind

and accelerated at the termination shock or within the heliosheath [7, 8]. Galactic cosmic rays are particles that originate from sources within our galaxy outside our solar system. Extragalactic cosmic rays are particles from beyond our galaxy [9, 10]. Besides the source, cosmic rays with energies above 10^{18}eV are called ultrahigh-energy cosmic rays [11]. Due to the fact that cosmic rays have a spectrum which decreases with increasing energy, the contribution of ultrahigh energies to the flux and energy density of all cosmic rays is negligible. Furthermore, the contribution of solar energetic particles is limited to low energies, $\leq \sim$1 GeV. Galactic cosmic rays are the main part of primary radiation reaching us from interstellar space [12].

The origin of cosmic rays and their propagation are fundamental questions that have a major impact on our understanding of the universe. We know of no process in the Galaxy other than supernova shock waves that can provide the power required to sustain the observed galactic cosmic-ray intensity. The shock acceleration mechanism is believed to be prevalent in astrophysical plasmas on all scales throughout the universe. It has been shown in the heliosphere, e.g., at planetary bow shocks, at interplanetary shocks in the solar wind, and at the solar wind termination shock [13–15].

It is characteristic of diffusive shock acceleration [16–20] that the resulting particle energy spectrum is much the same for a wide range of shock properties. This energy spectrum, when corrected for leakage from the galaxy, is consistent with the observed spectrum of galactic cosmic rays. In the most commonly used form of the theory [21], the characteristic limiting energy is about Z $\times 10^{14}$ eV, where Z is the particle charge. The observed composition should begin to change

beyond about 10^{14} eV, the limiting energy for protons, and the iron spectrum would start to steepen at an energy 26 times higher. In this scenario, protons would be the most dominant element at low energies, but heavier elements would become relatively more abundant at higher energies, at least up to the acceleration limit for iron nuclei.

Observations of non-thermal synchrotron radiation from several shell-type remnants [22–24] provide compelling evidence that supernova remnants (SNR) are common sites for shock acceleration of electrons. Non-thermal X-ray spectra indicate the presence of very high-energy electrons which, at least in the case of supernova SN 1006, have energies $> 2 \times 10^{14}$ eV [22]. These electrons were likely accelerated at the remnants because at this energy electrons cannot travel far from their origin before they are attenuated by synchrotron losses. There are other sources of particle acceleration that may also contribute to the cosmic-ray beam [25]. Recent Chandra X-ray observations of Tycho's supernova remnant have shown hot gaseous supernova debris keeping pace with an outward-moving shock wave indicated by high-energy electrons.

Semi-direct evidence for the acceleration of cosmic-ray protons could come in the form of gamma rays from pion decay [26]. Indeed, the observation of TeV gamma rays, possibly of π^0-origin, from the SNR RX J1713.7-3946 [27, 28] may have revealed the first specific site where protons are accelerated to energies typical of the main cosmic-ray component. The gamma rays' hadronic origin is yet to be confirmed, but the CANGAROO collaboration has shown that the energy spectrum of gamma-ray emission from SNR RX J1713.7-3946 matches that expected if the

gamma rays are the decay products of neutral pions generated in proton-proton collisions. Although the proton scenario is favored because of the spectral shape, gamma rays may originate from either electrons or protons. A complete understanding of gamma-ray emission processes may need a broadband approach [29], using all the available measurements in different wavelength regions. It is also possible that direct measurements of nuclear particle composition changes would provide strong corroborating evidence that shocks associated with shell-type supernova remnants provide the acceleration sites for cosmic rays.

Shock acceleration is the generally accepted explanation for the characteristic power-law feature of cosmic-ray energy spectra [30], although ground-based measurements have shown that the all-particle spectrum extends far beyond the highest energy thought possible for supernova shock acceleration. These measurements have also shown that the energy spectrum above 10^{16} eV is steeper than the spectrum below 10^{14} eV, as shown in Figure 1.1, which lends credence to the possibility of a different source. Of course, the "knee" structure might be related to energy-dependent leakage effects during the propagation process [31, 32] or to other effects, such as reacceleration in the galactic wind [33] and acceleration in pulsars [34]. Whether and how the spectral "knee" is related to the mechanisms of acceleration, propagation, and confinement are among the major current questions in particle astrophysics.

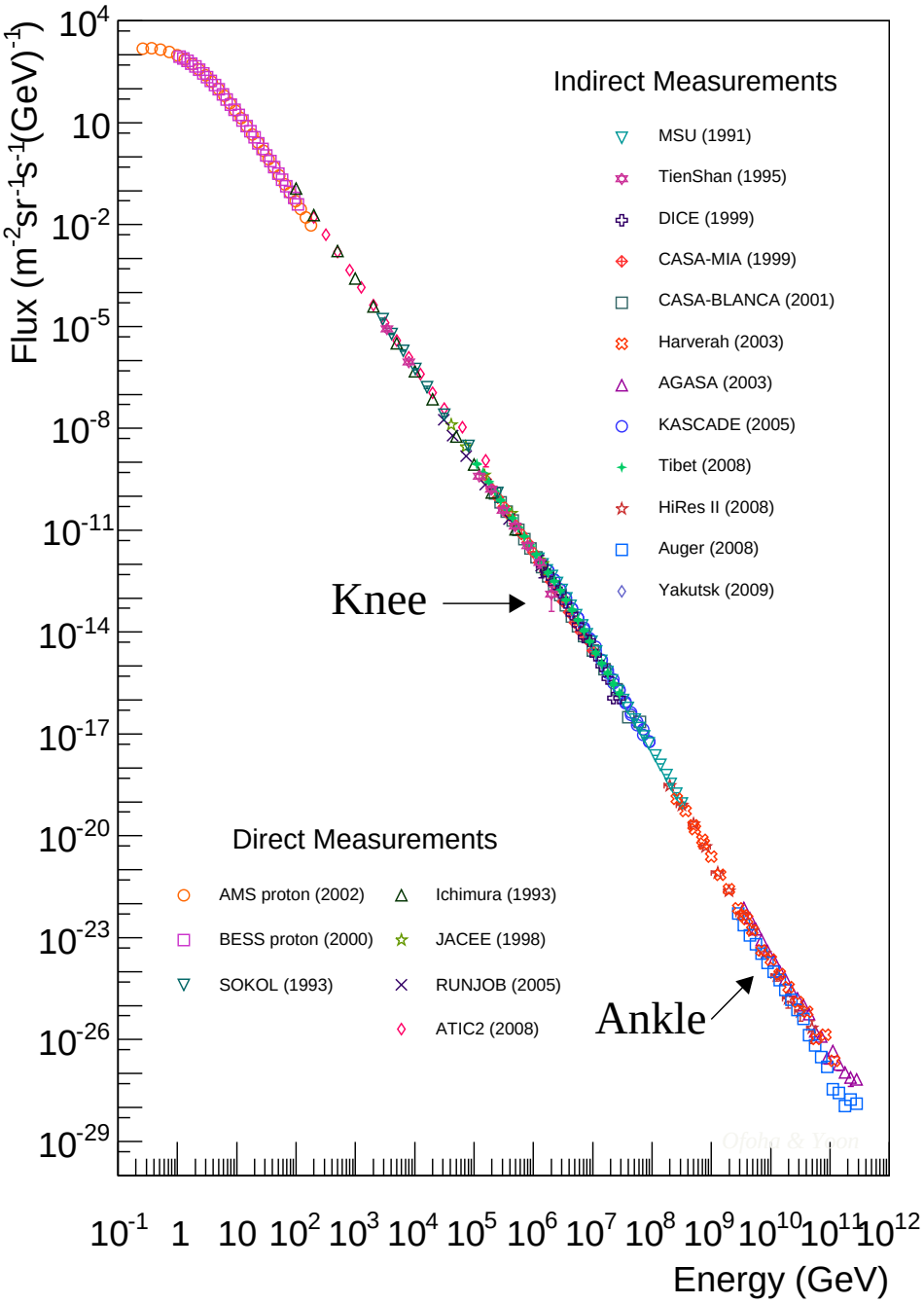

Figure 1.1: Cosmic-ray all particle spectra [35–53]. All-particle spectra have been determined by indirect measurements using ground-based experiments and direct measurements from balloon-borne and space based experiments.

1.2 Cosmic-ray Measurements

The measured cosmic-ray spectrum extends to 10^{11} GeV, as shown in Figure 1.1. Up to about a hundred GeV, the charge and mass of primary cosmic-ray particles have been measured with magnetic spectrometers. Measurements with emulsion chambers and calorimeters provide elemental primary spectra up to about 100 TeV. The indirect measurements of air showers from the ground provide the all particle spectrum around PeV and the anisotropy of cosmic-rays above TeV [54–56].

A relatively large number of measurements of primary cosmic-ray energy spectra have been made with good precision at energies up to $\sim 10^{11}$ eV. Above this energy, the uncertainties of measured results were large, as shown in Figure 1.2, although there have been some pioneering measurements [42, 43, 47, 48, 57–59]. For example, fluxes from Japanese-American Collaborative Emulsion Experiment in Figure 1.2 have larger fluctuation than their statistical uncertainties. In addition, whether or not protons have the same spectrum as heavier nuclei is still unclear, as shown in Figure 1.2. Their different spectral behavior could be interpreted as evidence for different types of sources or different acceleration mechanisms for different elements [60]. These roll-off energies for protons are 1 - 2 orders of magnitude below the "knee" seen in the all-particle spectrum. An overall trend of flatter high energy spectra for heavy elements was indicated in the data compiled by Wiebel-Sooth *et al.* [61] and Hörandel [62].

The Cosmic Ray Energetics And Mass (CREAM) experiment [63] was designed and constructed to measure cosmic ray elemental spectra using a series of

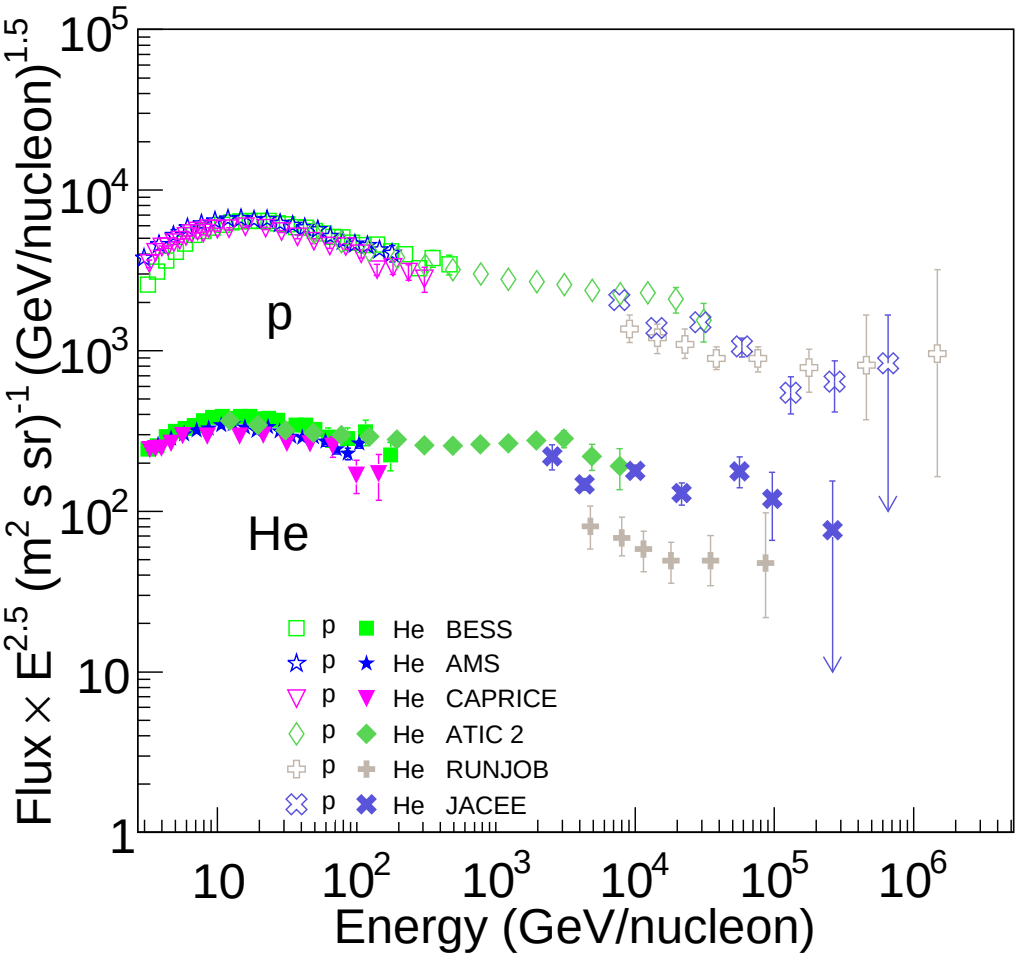

Figure 1.2: Proton and helium spectra have been measured by various experiments [42,43,47,48,58,59]. Whether or not protons have the same spectrum as heavier nuclei is still unclear.

ultra long duration balloon (ULDB) flights [64]. The instrument has redundant and complementary charge identification and energy measurement systems capable of precise measurements of elemental spectra for Z = 1 - 26 nuclei over the energy range $\sim 10^{11}$ - 10^{15} eV (0.1 - 1000 TeV). The energy of incident particles is measured by a sampling tungsten/scintillator calorimeter, that overcomes the limits of the maximum detectable energy in the range of a few tens GeV for magnetic spectrometers and saturation in homogeneous calorimeters. At the highest of these energies, a change in composition occurs which could reflect the rigidity-dependent supernova acceleration limit. Precise measurements of the elemental spectra energy dependence at such energies provide a key to understanding cosmic ray acceleration and propagation.

So far, five successful flights of CREAM have been completed, and the accumulated flight time is about 156 days. The first flight during the 2004-2005 austral season lasted for 42 days. The second, third, fourth, and fifth flight were carried out in the following seasons of 2005-2006, 2007-2008, 2008-2009, and 2009-2010, respectively.

1.3 Outline

This dissertation is based on the author's participation in the CREAM experiments, especially in the following areas: integration, tests, flight operations and data analysis for the first flight and the calorimeter construction and calibration beam test for the third flight. The analysis of proton and helium spectra with the

calorimeter and the silicon charge detector was focused on the calibration of the calorimeter with an electron beam at European Organization for Nuclear Research (CERN), efficiency estimation with Monte Carlo (MC) simulations, and proton and helium differential energy spectra. The first chapter introduces cosmic rays and their investigation with CREAM. Chapter 2 gives a description of the CREAM detectors. Chapter 3 gives a description of the CREAM flight and its operation concepts. Chapter 4 summarizes the data analysis of proton and helium spectra, which includes calibration factors for the flight data, stable data periods, event selection, charge determination, energy measurements, uncertainty estimation and corrections for the absolute fluxes such as efficiencies, backgrounds, and live-time estimations. In Chapter 5, the measured proton and helium fluxes and their ratios are compared with previous measurements. The indices of proton and helium spectra are obtained. In Chapter 6, the results and their implication are discussed briefly.

Chapter 2

CREAM Instrument

The instrument was designed to meet the challenging and conflicting requirements of a large geometry factor to collect adequate statistics for the low flux of high-energy particles, and the weight limit for near-space flight. The instrument was comprised of a suite of particle detectors to determine the charge and energy of the incident particles. As shown schematically in Figure 2.1, the detector configuration included a timing charge detector (TCD), transition radiation detector (TRD), Cherenkov detector (CD), silicon charge detector (SCD), scintillating fiber layers (S0/S1, S2, and S3), and the tungsten/scintillating fiber calorimeter (CAL).

A key feature of the CREAM instrument is its ability to obtain energy measurements simultaneously with calorimeter and TRD techniques. With two independent energy measurements, cross-calibration between the calorimeter and the TRD can be confirmed [66]. In addition, multiple charge measurements with the TCD, CD, SCD and HDS (S0/S1 layers of scintillating fibers) minimize the effect of back-scattered particles from the calorimeter. The detectors are described with more detail in papers [67–69].

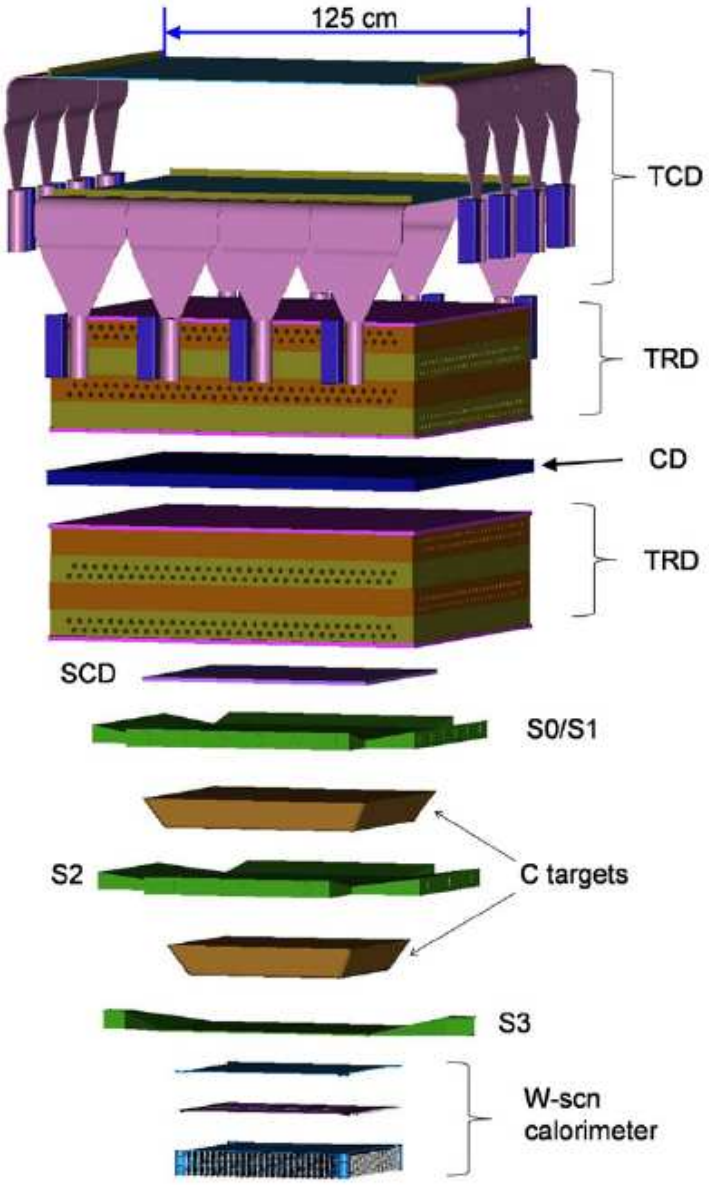

Figure 2.1: Schematic of the CREAM instrument configuration [65]. Placement from top to bottom is as follows: timing charge detector (TCD), transition radiation detector (TRD), Cherenkov detector (CD), silicon charge detector (SCD), scintillating fiber layers (S0/S1, S2, and S3), carbon targets, and the tungsten/scintillating fiber calorimeter.

2.1 Timing Charge Detector and S3

The TCD measures the light output due to energy loss of incident particles in the scintillator. It is designed to measure the charge of particles from helium to iron nuclei with a resolution of $< 0.35e$ [69]. It covers the top of the instrument as shown in Figure 2.2. The TCD consists of two layers, each with four fast scintillator paddles side by side. Each scintillator paddle is 120 cm long, 30 cm wide, and 0.5 cm thick. The long axes of the paddles are in two layers oriented perpendicular to each other. Each paddles has an adiabatically shaped light guide glued to fast photo-multiplier tubes (PMTs) for signal readouts on both ends. For each PMT, both signal amplitude and time are recorded and then used as peak detectors and time-to-digital converters (TDCs) [69]. The PMT pulses are measured from several dynodes within an amplification chain to cover wide dynamic range. Figure 2.3 shows the charge histogram from the first CREAM flight. A resolution better than $0.2e$ is obtained for oxygen and $\sim 0.4e$ for iron.

The S3 is a layer of scintillating fibers with a 115×52 cm^2 active area, positioned directly over the calorimeter, about 1.1 m below the TCD layers. It is sensitive to the incident particles and back-scattered particles from the calorimeter, allowing a time-of-flight measurement with the TCD and albedo rejection. It is also used to generate a trigger for low charge events, which is called ZLO, in coincidence with the TCD.

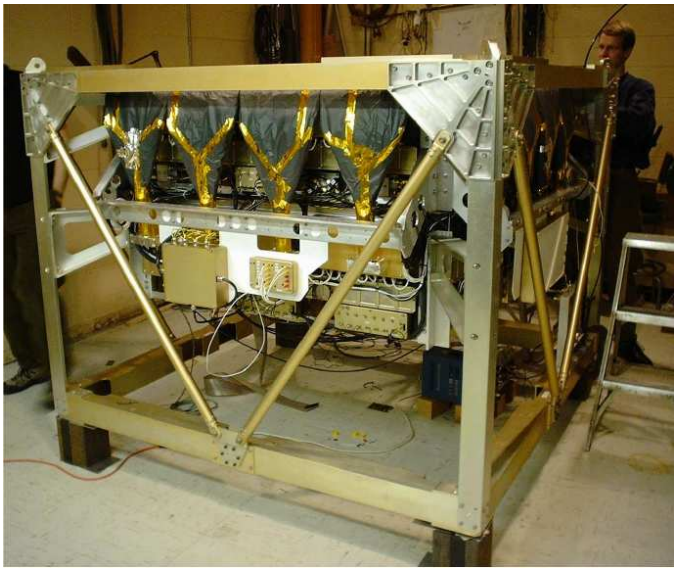

Figure 2.2: Photograph of the TCD and TRD [69] assembled. TCD and TRD were assembled in the instrument supporting structure.

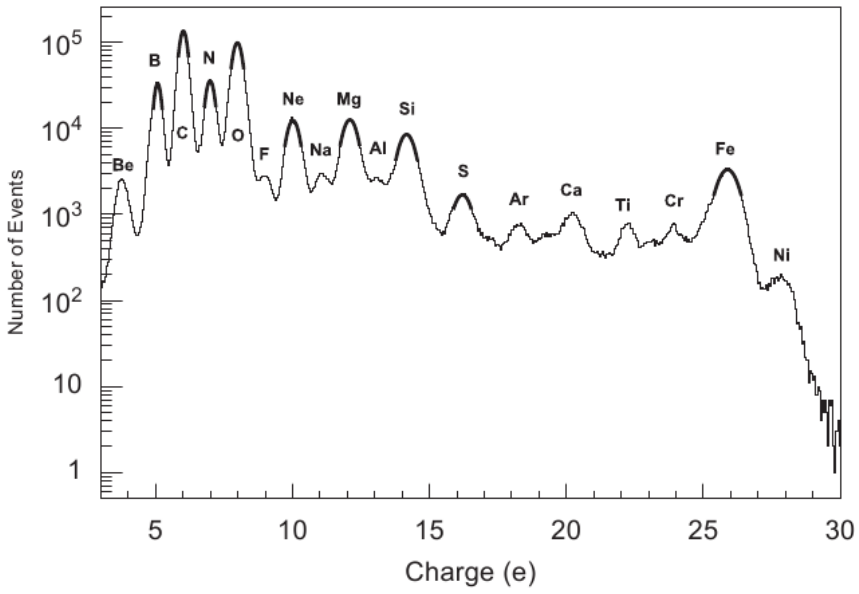

Figure 2.3: TCD charge reconstructed from a fraction of the flight data. The charge resolution is clearly better than $0.2e$ for oxygen and $\sim 0.4e$ for iron [69].

2.2 Transition Radiation Detector and Cherenkov Detector

The TRD measures the transition radiation generated from incident particles moving through media with different dielectric constants. It is designed to provide a measurement of the Lorentz factor (γ) for primary particles. In addition, the TRD can provide particle tracking with a resolution of $\sigma \sim$1 mm [70].

As shown in Figure 2.4, the TRD is comprised of two modules, each with an active volume of $120 \times 120 \times 35$ cm^3. Each module is comprised of four manifolds, with 64 2"-diameter tubes and Dow Ethafoam 220 in each manifold. This polyethylene foam serves as a radiator and light-weight mechanical support. Each foam section holds proportional aluminized tubes filled with a 95% xenon, 5% methane gas mixture. Signals are read out from a sense wire centered in each tube. The readout system covers the dynamic range required to measure particles from lithium to nickel nuclei over the Lorentz factor range $10^3 < \gamma < 10^5$ [70].

The CD is an acrylic plastic slab with the index of refraction n = 1.5, placed between the two TRD modules. It measures Cherenkov radiation, which is generated by incident particles moving faster than the speed of the light in the medium. The anode signal from PMTs attached to each end on four sides is provided to TCD electronics to make a trigger, called a ZHI trigger. The signal from dynodes of all eight PMTs provides another charge measurement, since the Cherenkov signal is proportional to the square of the incident charge.

The ratios of boron to carbon and nitrogen to oxygen using the TCD and TRD during the CREAM flight shown in Figure 2.5 have already been reported [70].

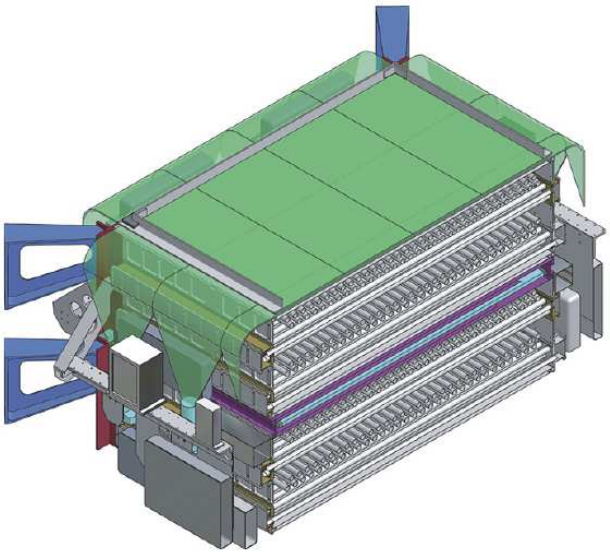

Figure 2.4: Three-dimensional cross section schematic of the TCD, TRD, and CD. Each tube is positioned inside the TRD [68].

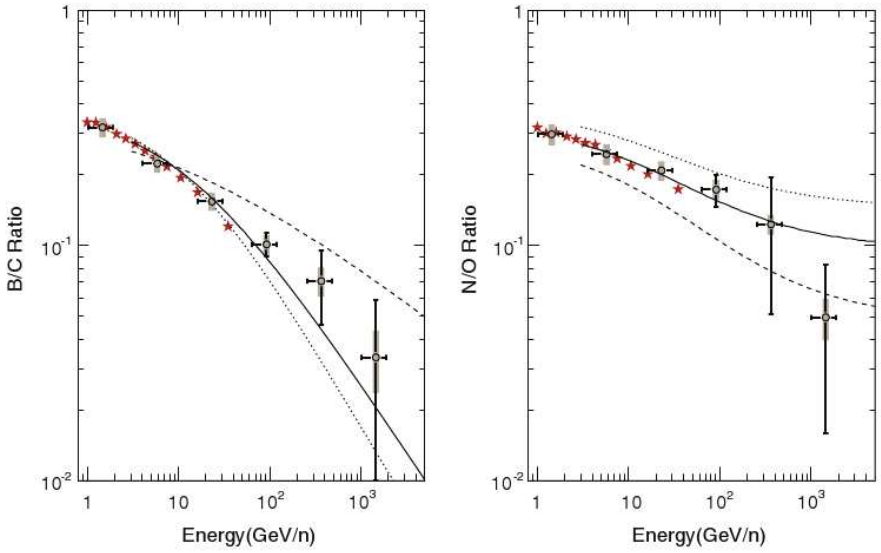

Figure 2.5: B/C and N/O ratios as a function of energy measured by the TCD and TRD [70]. CREAM measurement of the ratios (circles) were compared with HEAO-3-C2 (stars).

2.3 Silicon Charge Detector

The SCD is designed to identify incident particle charge ($Z \leq 28$) by measuring the energy loss of the particle in the silicon. It allows for measurements of incident particles both inside and outside the TCD acceptance, since it is positioned about 25 cm above the top of the calorimeter. It is required that the SCD measure the incident particle charge in the presence of back-scattered secondaries generated by interactions in the carbon targets and the calorimeter. The SCD is segmented into pixels, each with the area of 15.5×13.7 mm^2 to minimize the effect of back-scattered particles. Sixteen silicon pixels compose a sensor module in a 4×4 array. The 182 sensor modules (26 ladders $\times$ 7 sensor modules) are arranged so that edges will overlap at different heights in order to fully cover an active area of 78×79 cm^2 (Figure 2.6).

The readout electronics incorporate a 16-channel CR-1.4A ASIC for each sensor, followed by 16 bit Analog-to-Digital Conversion (ADC), allowing fine charge resolution over a wide dynamic range covering Z = 1 - 33 signals. The SCD revealed clear separation of all peaks with charge resolution < 0.2 e in a nuclear fragmented beam of $A/Z = 2$ and energy of 158 GeV/nucleon at CERN in November 2003 [71]. As shown in Figure 2.7, with minimal corrections at the preliminary stage, the charge peaks for major elements were clearly separated during the flight.

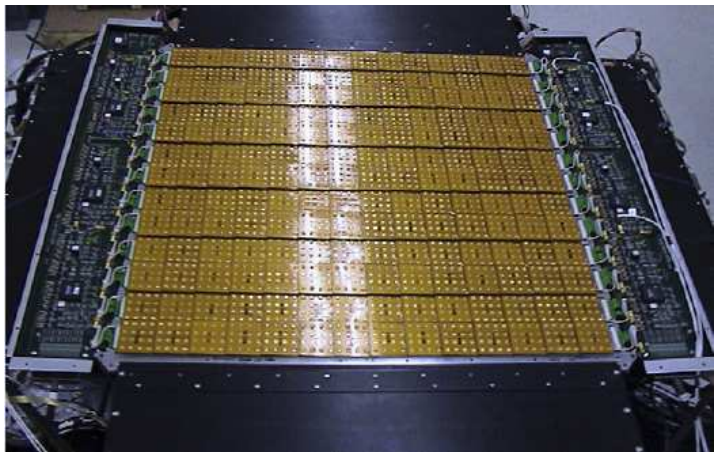

Figure 2.6: Top view of silicon charge detector is shown when covers are opened [68]. Seven sensor modules are connected to the electronics board at both sides along the ladders.

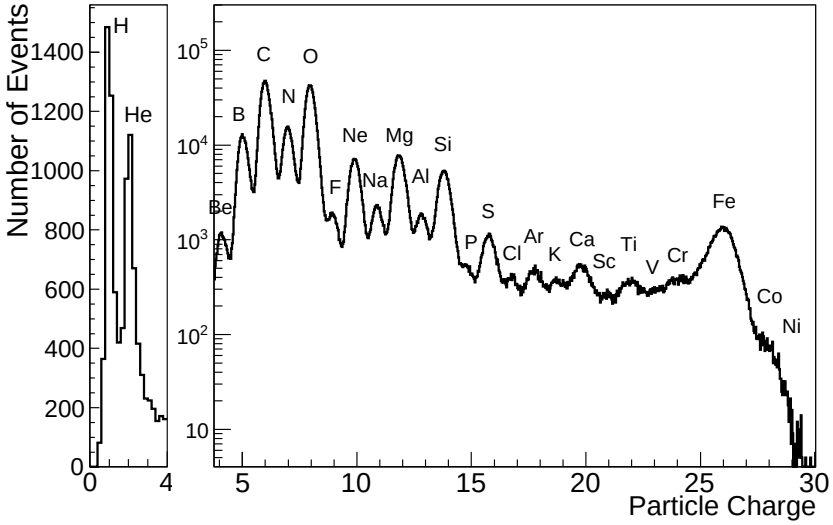

Figure 2.7: The distribution of charge (in units of charge e) of cosmic-ray nuclei measured with the SCD [65]. The individual elements are clearly identified. The left panel for protons and helium nuclei and the right panel for heavier nuclei are from two different triggers (see Section 2.6.1). The relative abundance in this plot has no physical significance, because needed corrections for interactions and propagations have not been applied to these data.

2.4 Hodoscopes

The hodoscopes (HDSs) are designed to provide particle trajectories in order to facilitate accurate charge measurement by measuring energy loss of incident particles in the scintillating fibers. Trajectory reconstruction from the calorimeter to the SCD plane is important for accurate charge measurement due to back-scattered particles. Scintillating fiber hodoscopes (S0/S1 and S2) interleaved with target layers add measurement points above the calorimeter to improve tracking accuracy and thus the accuracy of charge identification.

The HDSs are comprised of square plastic scintillating fibers, and are positioned between (S2) and above (S0/S1) the carbon targets (Figure 2.1). The crossed S0 and S1 layers are each comprised of 360 of 2×2 mm^2 square fibers, covering approximately 78×78 cm^2. The fibers are aluminized on one end to increase the light signal reaching the read out end. The other end, which extends outside the active area, is populated into a cookie connected to a hybrid photo-diode (HPD) for data readout [68].

The S2 located between the upper and lower targets also has a crossed pair of fiber layers. The S2 fibers are the same type and are read out in a similar manner with 3 HPDs per side. The active area of S2 is smaller, 64.6×64.6 cm^2, with 260 shorter scintillating fibers in each layer. Although the HDSs were designed for tracking, they also serve as redundant charge measurement detectors (Figure 2.9).

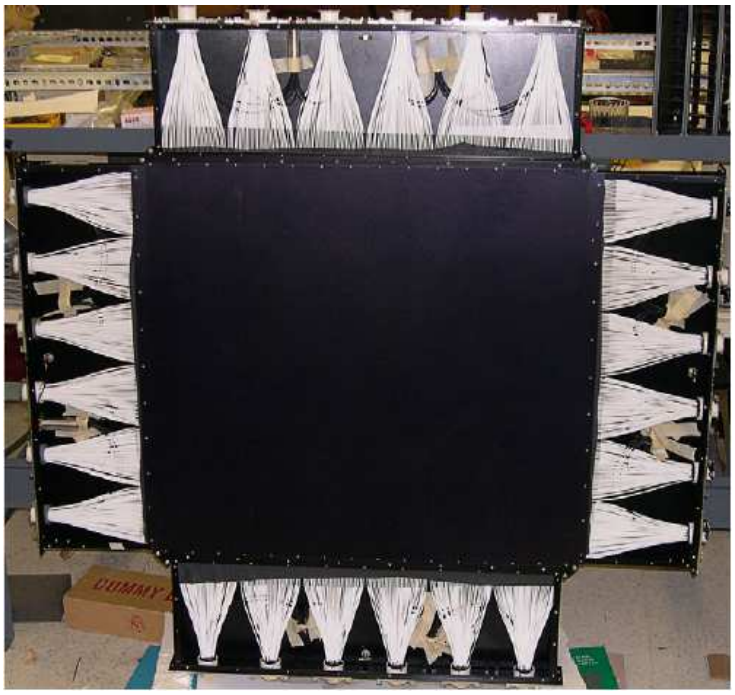

Figure 2.8: A top view of Hodoscope S0/S1. Active area is covered by an aluminum cover [68]. The fibers are converged alternatively to both ends for readout.

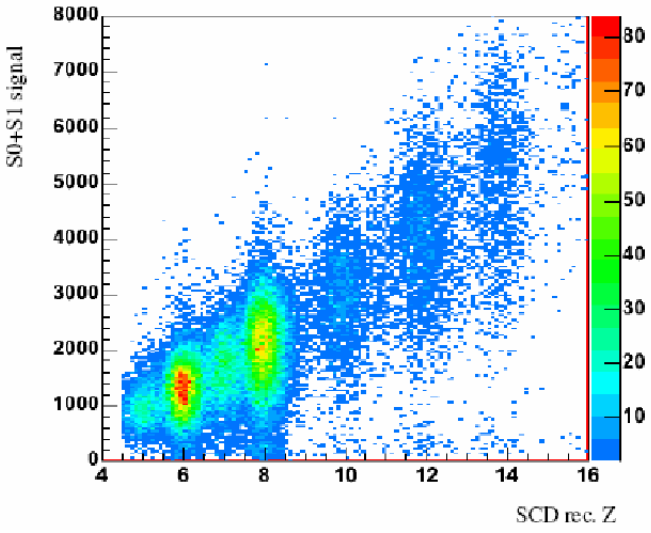

Figure 2.9: Correlation between raw HDS signal and SCD charge with the flight data [72].

2.5 Calorimeter

There are two types of calorimeters - homogeneous and sampling [73]. In a homogeneous calorimeter, the entire detector volume is sensitive to the particles and may contribute to the signals generated by the detector. Some homogeneous calorimeters are built with inorganic heavy scintillating crystals such as BGO, CsI, NaI and PWO. In a sampling calorimeter, the functions of particle absorption and signal generation are exercised by different materials called the passive and active medium. The passive medium is usually a high-density material such as lead, iron, copper or depleted uranium. The active medium may be a scintillator, an ionizing liquid, a gas chamber or a semiconductor [74].

The calorimeter is the only practical instrument for measuring the energy of protons and helium nuclei above 1 TeV, but homogeneous calorimeters are too massive to be incorporated into space-based or balloon-borne experiments [75]. A thin sampling calorimeter offers a practical approach. The CREAM calorimeter is designed to measure the energy of incident particles above 100 GeV [68]. It is a sampling calorimeter with tungsten and plastic scintillating fibers as the passive and active medium, respectively. The sampling fraction is $\sim$0.13% [76], which is sufficient for TeV showers.

Two 9.5 cm-thick targets with a 30° flare angle and about 0.5 nuclear interaction length (λ_I) precede the calorimeter to initiate nuclear interactions for incident particles (Figure 2.10). These targets are comprised of blocks of densified graphite with a density of 1.92 g/cm^3.

Figure 2.10: Side view of targets and the calorimeter for the third flight after assembly. The structure of the calorimeter for the first flight and the third flight are the same. In the calorimeter for the third flight, aluminum wall frames surround the tungsten plates while plastic wall frames were used in the first flight. S2 was located between the two targets.

The calorimeter is comprised of a stack of twenty tungsten plates, each 50 $\times$ 50 $\times$ 0.35 mm^3. Each tungsten plate is approximately one radiation length (X_0) in thickness. The plate is followed by a layer of fifty 10 mm-wide, 503 mm-long scintillating ribbons, each with nineteen 0.5 mm-diameter scintillating fibers. The readout end of each fiber is glued into an acrylic light guide, as shown in Figure 2.11. Neighboring ribbons are read out in opposite directions. Ribbons are oriented perpendicularly to the ribbons in the previous layer. The ribbons from every other ten layers are providing X-Z position data and ribbons in the other ten layers are providing Y-Z position data for a trajectory reconstruction. Figure 2.12 shows twenty layers of tungsten and scintillating fibers that have been stacked up one by one.

A bundle of clear fibers is glued into the light guide. The opposite end of the

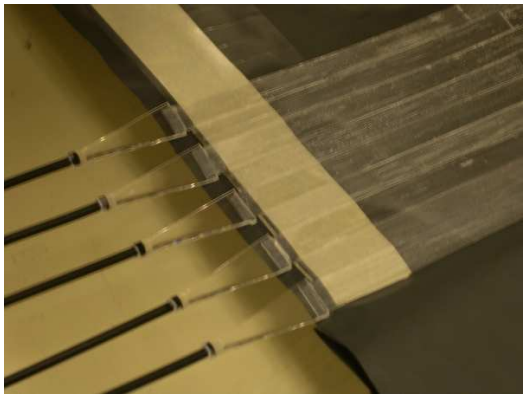

Figure 2.11: Calorimeter scintillating fiber ribbons in the light guide. The ribbon with 19 scintillating fibers is glued to the light guide. On the other side of the light guide, a bundle of clear fibers are glued.

Figure 2.12: Calorimeter after stacking up all 20 layers of tungsten and scintillating fibers.

clear fibers are separated into three groups: low range (37 fibers), middle range (5 fibers) and high range (1 fiber). The three groups are read out by separate pixels on HPDs. Each HPD has 25 low-range and 25 middle-range pixels connected to fibers from every other ribbon in a layer. Five high-range pixels connect to fibers from five of every other ribbon in a layer. There are 3 pixels connected to an LED source for alignment and in-flight calibration, and six pixels without optical inputs for coherent electronics information. An additional neutral density filter was inserted between clear fibers and the middle and high range pixels to increase the dynamic range. The HPD dynamic range of about 1,000,000:1 is enough to cover 200,000:1 required for measuring showers from 10^{12} to 10^{15} eV [68]. Ten HPDs are mounted on top of the readout box (Figure 2.13). Ten front-end electronics boards inside the readout box digitize signals from each HPD, which are connected to every other 25 ribbons in a layer. The digitized signals are sent to the science flight computer.

2.6 Electronics System

2.6.1 Trigger System

The trigger system is comprised of a master trigger, calorimeter trigger and TCD trigger, as shown in Figure 2.14. The calorimeter trigger is designed for high-energy shower events and the TCD trigger is designed for events in which a high-charge nucleus traverses the TCD and TRD.

The master trigger accepts inputs from the calibration system, calorimeter, and TCD. It generates the signal initiating data collection and distributes the trigger

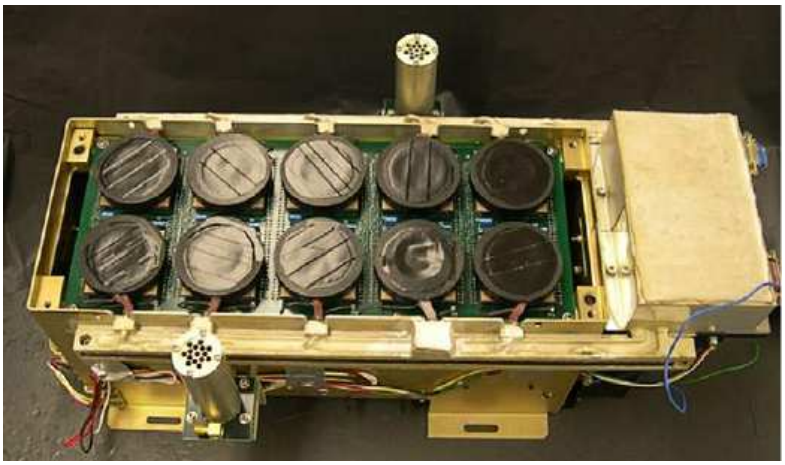

Figure 2.13: Calorimeter readout electronics box. Ten HPDs are mounted on the top of the box [69]. Two high-voltage power supplies are mounted at the right side. LED light sources are contained in the two cylinders at the center area.

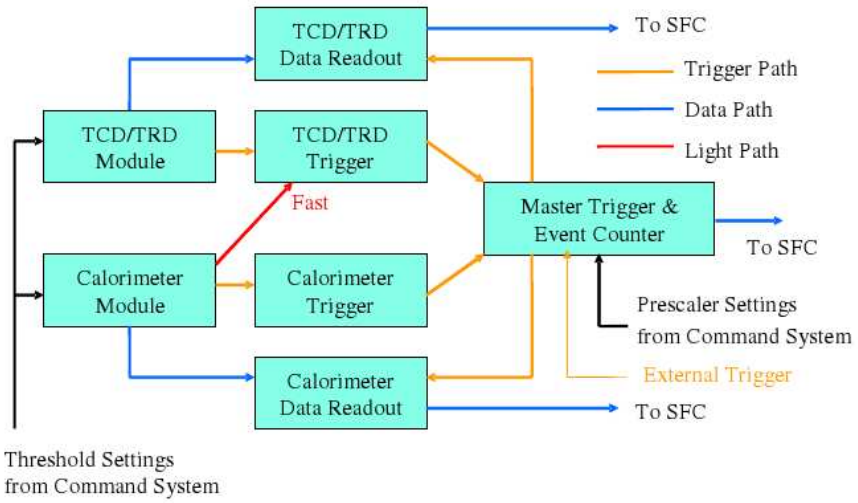

Figure 2.14: Trigger and data flow [68]. The TCD and calorimeter send trigger signals to the master trigger (yellow). After the master trigger distributes the trigger flag, detectors send data to the science flight computer(SFC).

signal to relevant detectors for data collection. The master trigger has an 8-bit prescaler for the calorimeter and TCD to adjust the incoming trigger rates, allowing separate control over the rate of each trigger. The master trigger provides a signal to the housekeeping system for a live-time counter when the SFC and the instrument are ready for incoming particles.

The calorimeter trigger requires the highest signal over the threshold at 4, 6, 8, or 10 consecutive layers to be active. The required number of layers and the calorimeter threshold can be set by the command system. During the CREAM flight, the required number of layers was set to 6 based on the simulation and noise level tests. The calorimeter trigger threshold was adjusted from 70 to 90 Digital-to-Analog Conversion (DAC) values during the flight. The calorimeter trigger threshold value will be presented in Section 3.

The TCD generates two triggers and sends them to the master trigger: a ZLO and ZHI trigger. The ZLO trigger is optimized for $1 \leq Z \leq 5$ and the ZHI trigger is optimized for $Z \geq 5$ [69]. While the single ZHI trigger or calorimeter trigger initiate an event at the master trigger, the single ZLO trigger doesn't initiate an event. The ZLO bit information is provided when an event is initiated by a ZHI or calorimeter trigger.

2.6.2 Science Flight Computer

The science flight computer (SFC) is a single-board computer with a PC/104 interface, which is mounted on the instrument to operate and monitor the instru-

ment. When the trigger flag is distributed from the master trigger to sub-detectors, measured signals from each sub-detector are sent to the SFC through the PC/104 interface, while signals from the TCD are sent to the SFC through the ethernet. All the prioritized data and some portion of the lower priority data are sent to the ground via telemetry. The SFC also has a 43 GB solid-state flash disk for archiving data.

2.6.3 Calibration System

The calibration system generates artificial or random triggers with a frequency from 0.06Hz to 1kHz. The trigger from the calibration system, called calibration trigger, is essential for all the status-check tests during tests on the ground, since the calorimeter trigger is not easily activated by muons or other particles. The calibration trigger is also used during flight to generate calibration events during the pedestal run process, charge-calibration run, and LED run process. The pedestal runs generates events every 5 or 10 minutes for the calorimeter, HDS, and SCD and mean and sigma in each channel were estimate with those pedestal events. The charge-calibration run generates events hourly during the flight to check the status of electronics by measuring each channel's gain with an input pulse for the calorimeter, the HDS and the SCD. The LED run generates events every two hours to check the aliveness of HPDs for the calorimeter and the HDS.

2.6.4 Housekeeping System

The housekeeping system monitors and reports the status of the instrument such as temperatures, currents, bias voltages and sensor high voltage, trigger rates, etc. The reporting frequency of a housekeeping event can be adjusted by command. During flight, housekeeping events were sent about every 5-10s.

In addition, the housekeeping system includes two 48-bit counters, which accumulate total-time and live-time with a resolution of about 3.25μs [77]. The counter for the live time is designed to run according to a status flag from the master trigger.

Chapter 3

CREAM Flight

The CREAM instrument was designed and constructed to meet the challenging requirements of a nominal 100-day ULDB flight. The first CREAM payload was launched with the Long Duration Balloon (LDB) from Williams Field near McMurdo Station, Antarctica on December 16, 2004 (Figure 3.1). It subsequently circumnavigated the South Pole three times for a record breaking duration of 42-days, as shown in Figure 3.2; the flight was terminated on January 27, 2005 (Figure 3.3). The float altitude of the payload remained between 37 and 40 km through most of the flight (Figure 3.4). The corresponding atmospheric overburden was 3.9 $\pm$ 0.4 g/cm^2. The diurnal altitude variation due to the Sun angle change was very small, $<$ 1 km, near the pole, i.e. at high latitude, which increased as the balloon spiraled out to lower latitudes [63]. The temperature of the various instruments stayed within the required operational range with daily variation of a few degrees Celsius, consistent with the Sun angle variation (Figure 3.5). For example, the pedestal mean variation due to temperature change for 5 minutes was less than 1 ADC unit. The 1 ADC unit variation of pedestal mean can cause about 1% of uncertainty in deposited energy at 10 TeV and smaller than 1% at higher energies.

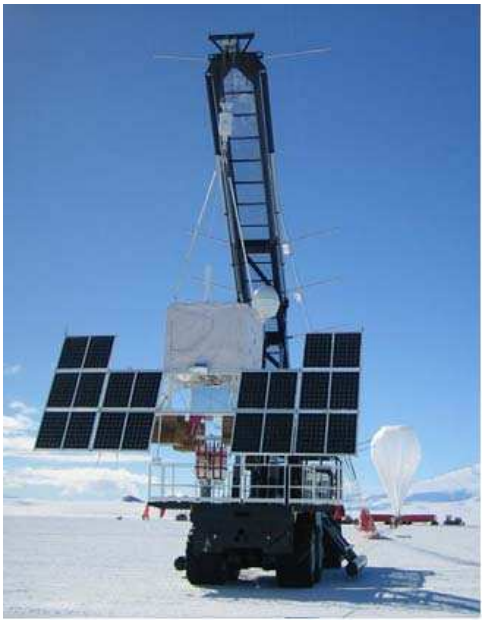

Figure 3.1: Payload at the launch site on Williams Field, Antarctica, while the balloon is being inflated [72].

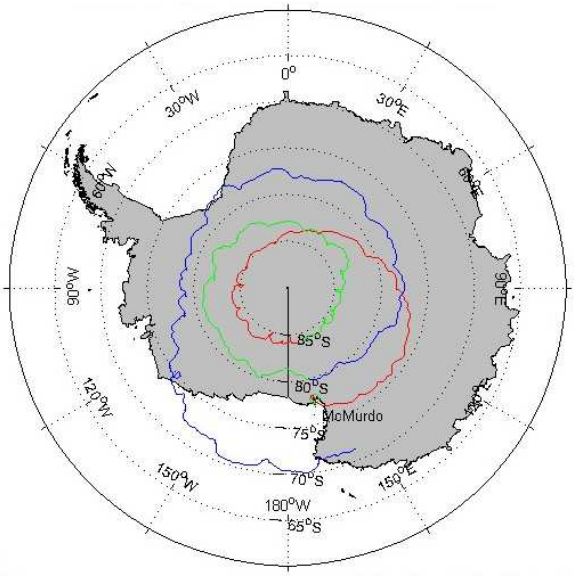

Figure 3.2: Balloon trajectory of the CREAM flight. CREAM broke both distance and duration records for LDB flights [72].

Figure 3.3: Payload after landing on January 27, 2005. All the detectors were recovered safely and shipped back to University of Maryland.

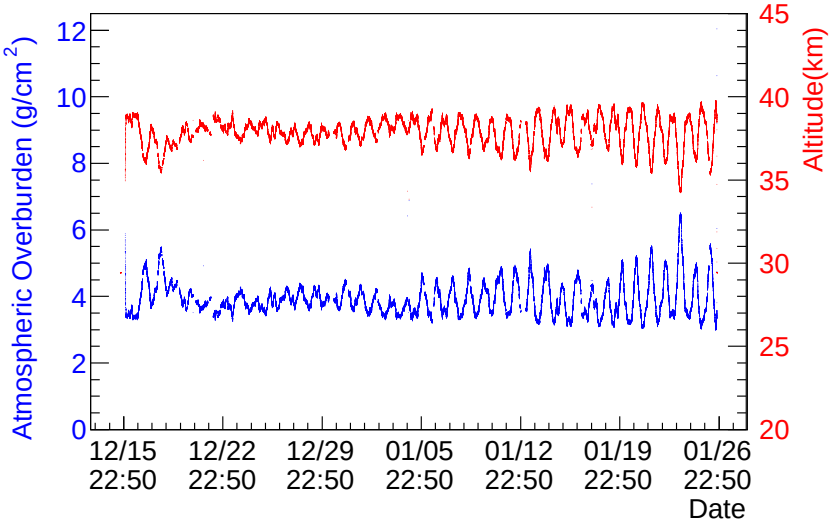

Figure 3.4: Altitude and atmospheric overburden variations during the flight. The atmospheric overburden, showing anti-correlation with the altitude variation, was about 3.9 g/cm^2.

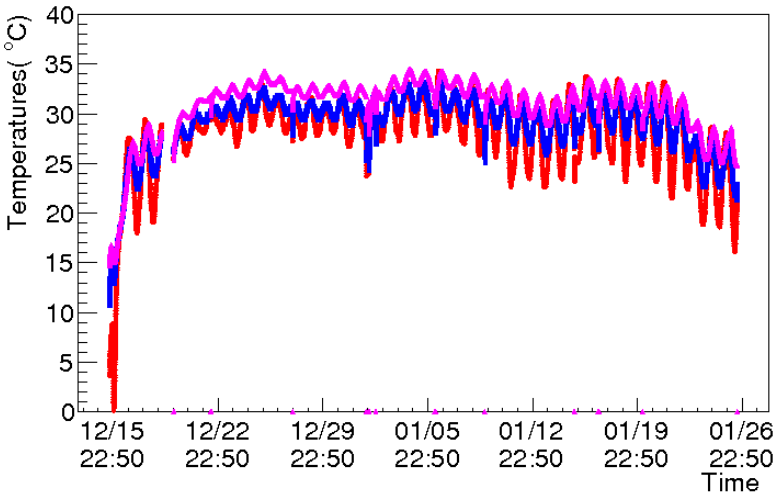

Figure 3.5: Temperature variations of the calorimeter (red), the HDS (blue) and the SCD (pink). These temperature measurements are sensors from electronics boards.

3.1 Flight Operations

The science instrument was supported by the Command and Data Module developed by NASA/Wallops Flight Facility [78]. This is in contrast to typical LDB payloads which utilize the Support Instrumentation Package provided by the Columbia Scientific Balloon Facility. CREAM was the first LDB mission to transmit all the primary science and housekeeping data (up to 85 kbps) in near real-time through the Tracking and Data Relay Satellite System (TDRSS) via a high-gain antenna, in addition to having data archive on an onboard disk. To fit the data into this bandwidth, science event records excluded information from channels that had levels consistent with their pedestal value: this is called "data sparsification." The threshold for this sparsification, called sparsification threshold value (STV),

was determined from a mean of pedestal events from the pedestal run process.

The science instrument was controlled from the Science Operation Center at the University of Maryland throughout the flight after line-of-sight operations ended at the launch site (Figure 3.6). Primary command uplink was via TDRSS, with IRIDIUM (Iridium satellite constellation) serving as backup whenever the primary link was unavailable due to schedule or traversing zones of exclusion. The nearly continuous availability of command uplink and data downlink allowed rapid response to changing conditions on the payload (e.g., altitude dependent effects) throughout the flight. A total of 60 GB of data including $\sim 4 \times 10^7$ science events were collected.

3.2 Detector Performance

The instrument functioned well during the flight, as illustrated by the example of an event in Figure 3.8, with two exceptions. The first was a malfunction of a live-time counter on the Master Trigger System, which provides the live-time fraction of the instruments. Therefore, the dead time of the first CREAM flight was estimated indirectly with the total trigger rate and the relation between the total trigger rate and live-time fraction from the second flight, which will be discussed in detail in Section 4.5.5. The other malfunction was the absence of signal in some channels due to missing HV and bias voltage on the HPDs on half of five layers. This was attributed to damaged soldering on a motherboard. The channels from every other 25 ribbons on 1^{st}, 2^{nd}, 4^{th}, 6^{th}, and 8^{th} layers, did not generate any signals. The deposited energy with no-signal channels was expected to be 10% less than

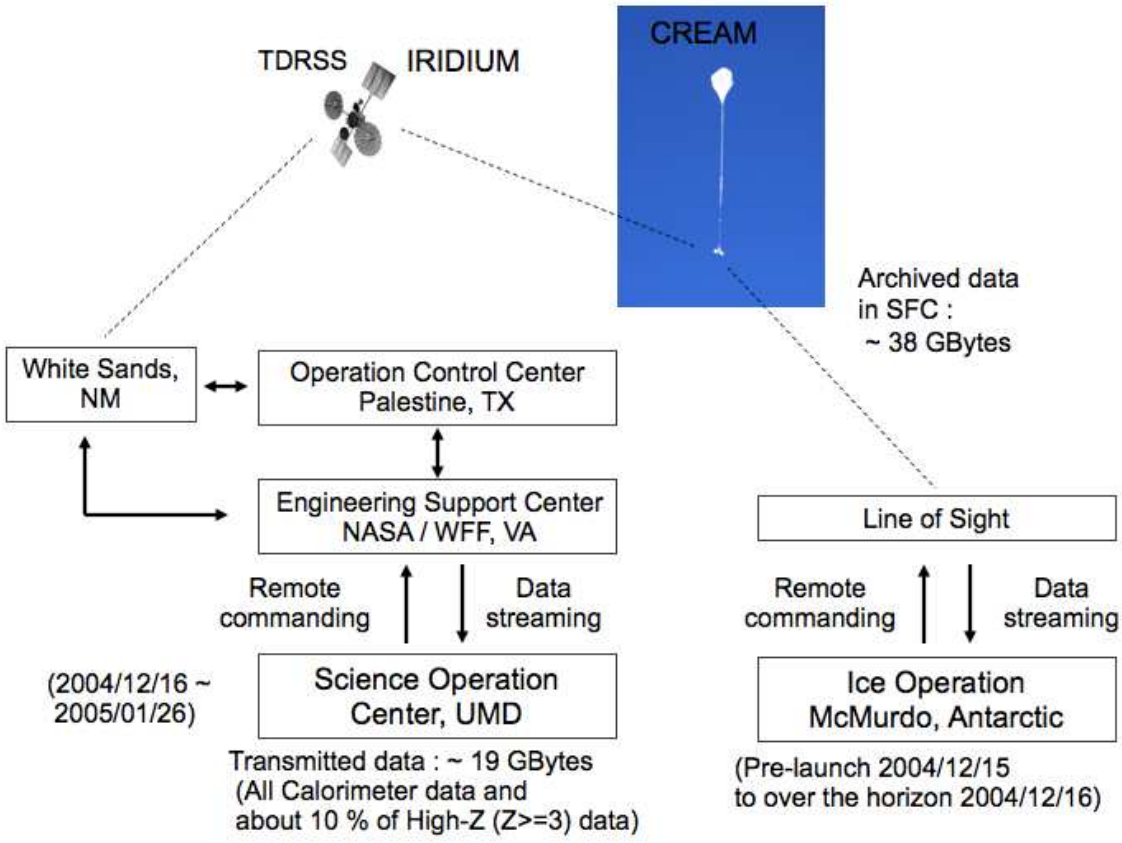

Figure 3.6: Flight operation overview. During the flight all high energy data and 10% of high-Z data (about 19 GB) were transmitted through TDRSS. All high-Z data not transmitted to the ground(about 37 GB) were archived on an on-board flash disk.

that without no-signal channels from MC simulations. This effect was corrected by masking channels in the energy conversion matrix when the deposited energy was converted to the incident energy.

The calorimeter trigger threshold was adjusted to optimize the calorimeter trigger rate during the flight as shown in Figure 3.7. The overall mean of the calorimeter trigger threshold was 75.8 DAC value, which corresponds to 45.2 MeV.

$$75.8 \text{ DAC value} \times 0.32 \text{ (Trigger gain)} \times 0.98 \frac{\text{ADC unit}}{\text{DAC value}}\text{(Electronics gain)} \times 0.93 \frac{\text{MeV}}{\text{ADC unit}}\text{(Calibration)} \times 2 \text{ (HV gain)} = 45.2 \text{ MeV}, \quad (3.1)$$

where the trigger gain, 0.32, was a ratio of a trigger input setting value (DAC value) to a trigger threshold (DAC value) from a trigger gain test, the electronics gain, 0.98 (ADC unit)/(DAC value), was a ratio of a signal input to output value (ADC unit) in electronics from the charge-calibration run, the mean calibration, 0.93 MeV/(ADC unit) was a mean of all channels' calibration constant, which was a ratio of MC simulations to a signal of beam data and the HV gain, 2, was a HPD gain correction due to different HV setting values between calibration test and flight data, which was obtained from LED test at different HV values before and during the flight. Figure 3.9 shows a deposited energy distribution of events with calorimeter trigger regardless of its charge information. The deposited energy distribution showed a reasonable power-law above the threshold. As shown in Figure 2.7, charge peaks for elements are clearly separated in the SCD.

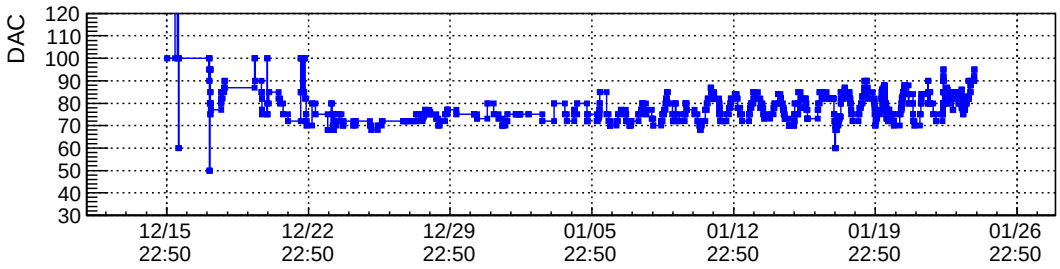

Figure 3.7: Calorimeter trigger threshold during the flight. The average trigger threshold during the flight is about 75.8 DAC value.

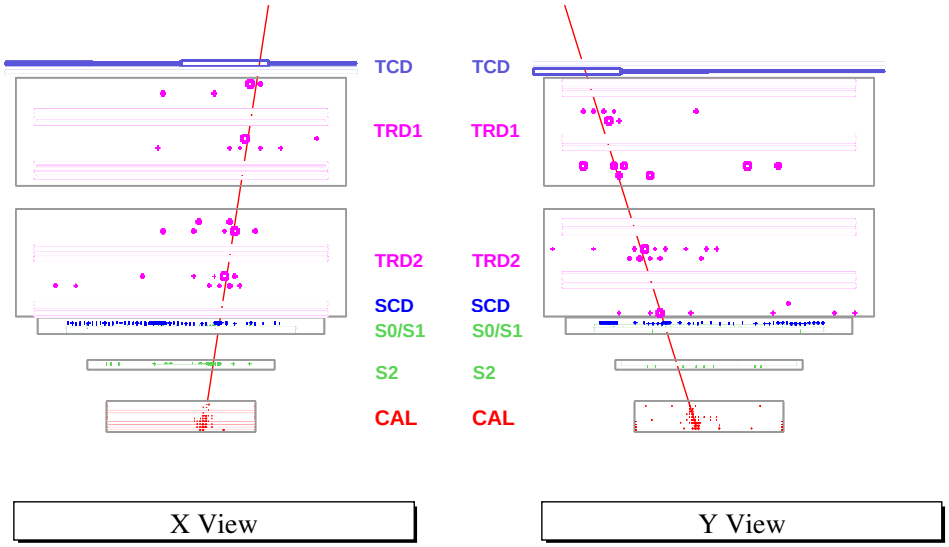

Figure 3.8: Example of an event with reconstructed trajectories from the calorimeter to the top of the instrument.

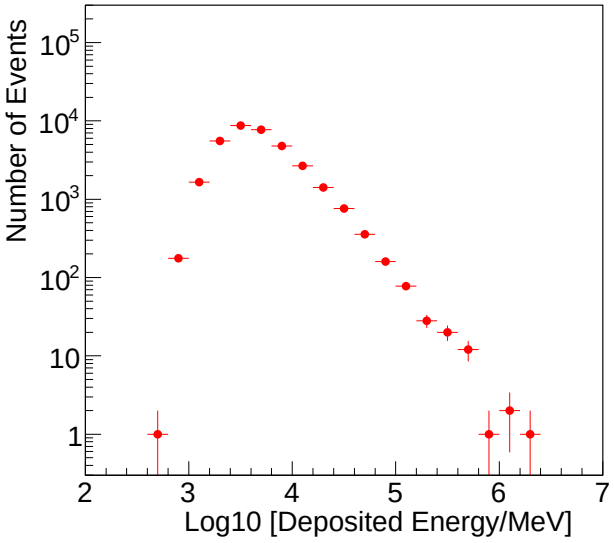

Figure 3.9: Distribution of energy deposited in the calorimeter from the first flight. Events triggered by the calorimeter showed a power-law distribution.

3.3 Solar Activity during the Flight

There was unusual solar activity during the flight, especially on January 20, 2005. The detectors on the payload were sensitive enough to record some effects from the solar activity, as shown in Figure 3.10 [79]. During the periodic pedestal runs of the SCD and HDSs, a sudden increase in pedestal distributions coincided with a reported powerful solar flare and the spike in the proton fluxes from the Geostationary Operational Environmental Satellites (GOES)-11 [80]. Preliminary analysis of those data showed a power-law spectrum up to a few hundred MeV [81].

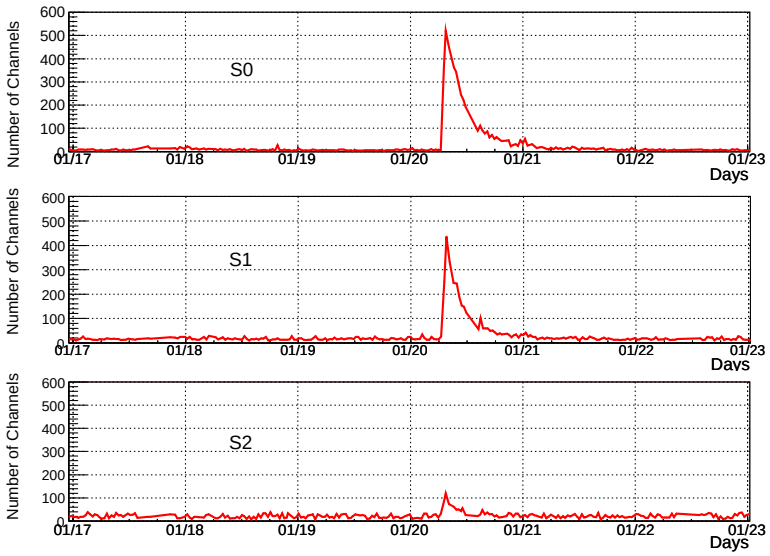

Figure 3.10: Indication of a solar flare on January 20, 2005 [81]. The number of channels with higher noise level in Hodoscope layers, S0, S1, and S2 suddenly increased. The higher noise level means a broad pedestal distribution due to the signal from real particles.

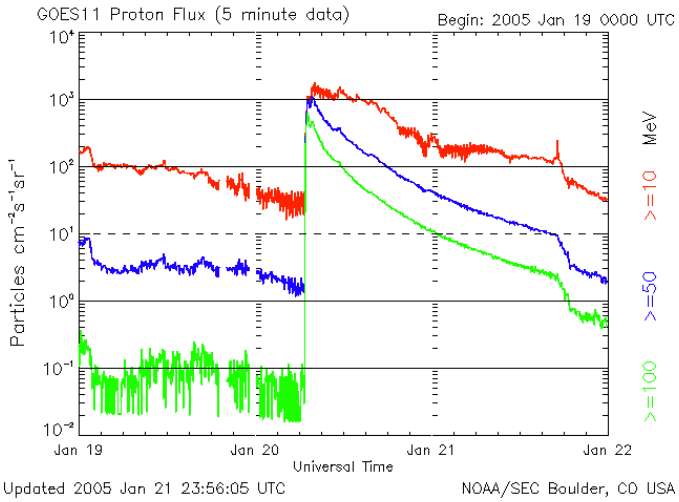

Figure 3.11: Proton flux from GOES satellite on January 20, 2005 [80]. Proton flux above 10 MeV (Red), 50 MeV (Blue), and 100 MeV (Green) were recorded every 5 minutes. The peak indicating an activity on January 20 coincided with the peaks from CREAM data (Figure 3.10).

Chapter 4

Proton and Helium Spectral Analysis

4.1 Event Selection

As shown in Table 4.1, about 24.4 days of data with stable instrument conditions were selected for the analysis. Data including periods of commanding for setting changes, data with abnormally high rates due to anomalous solar activity, and data with HV glitches were not included in this analysis.

Table 4.1: Stable periods of the flight data

From			To	
12/23/2004	18:01:12	-	12/27/2004	14:58:46
12/28/2004	05:30:12	-	12/29/2004	17:26:43
12/29/2005	19:51:09	-	12/30/2004	18:54:55
12/31/2005	03:35:52	-	1/ 1/2005	20:40:38
1/ 2/2005	19:56:58	-	1/ 6/2005	13:15:53
1/ 6/2005	18:53:46	-	1/ 9/2005	21:28:46
1/10/2005	02:31:38	-	1/12/2005	09:03:49
1/12/2005	13:35:15	-	1/15/2005	20:51:08
1/16/2005	03:43:26	-	1/17/2005	13:43:48
1/17/2005	21:40:21	-	1/17/2005	23:11:34
1/17/2005	23:42:15	-	1/20/2005	06:50:00

The event reconstruction requires at least one scintillating fiber ribbon with signals above the sparsification threshold ($\sim$10 MeV) in three layers on each view (XZ and YZ) of the calorimeter. The ribbon with the highest energy deposit and the neighboring ribbons on both sides were used to determine the position in each

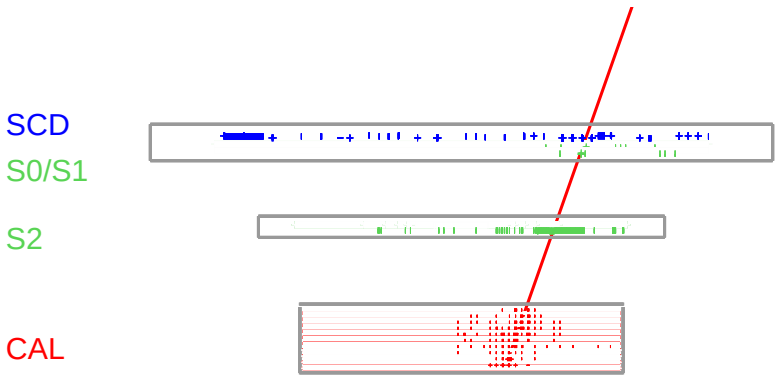

Figure 4.1: Reconstructed trajectory from the calorimeter to the SCD plane.

layer of maximum energy deposits (Figure 4.1). The shower axis was reconstructed by a least-squares fit of a straight line through a combination of these hit positions in the XZ and YZ planes [82]. The resulting trajectory resolution in the XZ plane is $\sim$1 cm when projected to the SCD. The trajectory resolution in the YZ plane is a little larger than 1 cm, due to masked no-signal channels caused by the lack of HV and bias on a HPD. The reconstructed trajectories were required to traverse the SCD active area and the bottom of the calorimeter active area.

Non-interacting particles and some events having their first hadronic interaction in the calorimeter layers instead of the carbon targets were removed from this analysis. These late interacting events could result in an underestimation of deposited energy, or misidentification of charge due to large uncertainties in the trajectory reconstruction. Since their longitudinal shower profiles are different, events with small energy deposits in the top few layers of the calorimeter were removed to ensure that the selected events had their first interactions either in the carbon targets or in the top of the calorimeter (Figure 4.2).

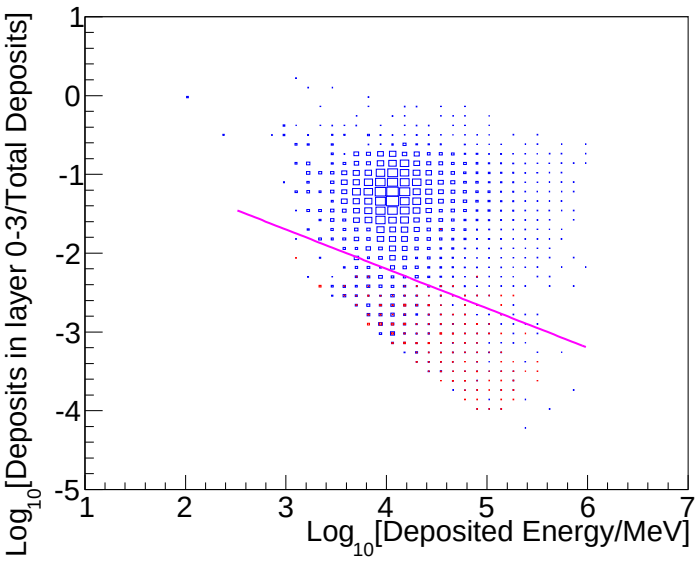

(a) MC proton events with a selection cut

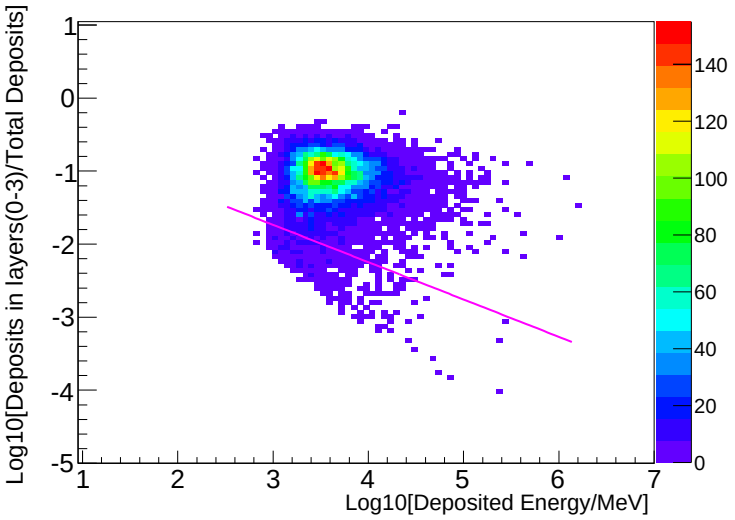

(b) Flight data events

Figure 4.2: Event selection with interaction position for MC simulations and flight data. Events with interactions in either carbon targets or top of the calorimeter were selected by a selection cut with fractions of deposited energy in the top 4 layers (line). In MC simulation (a), about 90% of events (blue) with interaction above the 6^{th} layer were selected and a few percent of events (red) with interaction below the 6^{th} layer were included. The same cut was used for the flight data.

4.2 Charge Determination

In order to determine the incident particle charge, the reconstructed shower axis from the calorimeter was extrapolated to the SCD, and a 7 × 7 pixel area, about 10 × 10 cm^2, centered on the extrapolated position was scanned to search for the highest pixel signal as shown in Figure 4.3. The scanned area was optimized to sustain 100% charge identification efficiency in all energy bins and determined to be a 7 × 7 pixel area, as shown in Figure 4.4, since the flight data have no-signal channels in the calorimeter and masked channels in the SCD.

The highest pixel signal, selected in scanned area, was then corrected for the particle path-length (calculated from the reconstructed incidence angle) in the sensor. Figure 4.5 shows the SCD signal distribution with proton and helium peaks before and after the path-length was corrected for the incident angle. The signal reflects the ionization energy loss per unit path length (dE/dx) of an incident particle in the SCD. The energy loss is proportional to Z^2, which is described in Bethe-Bloch formula [74].

An advantage of the charge measurement with pixelated sensors is the reduced effect of back-scattered particles. According to Monte Carlo (MC) simulations and beam tests, the expected contamination from secondary particles back-scattering from the calorimeter is less than 3% when this tracking-based selection method is used [83]. The effect due to back-scattered particles on the measured protons and helium nuclei in the flight data was corrected in efficiencies and background.

The resulting SCD signal distribution is shown in Figure 2.7. The measured

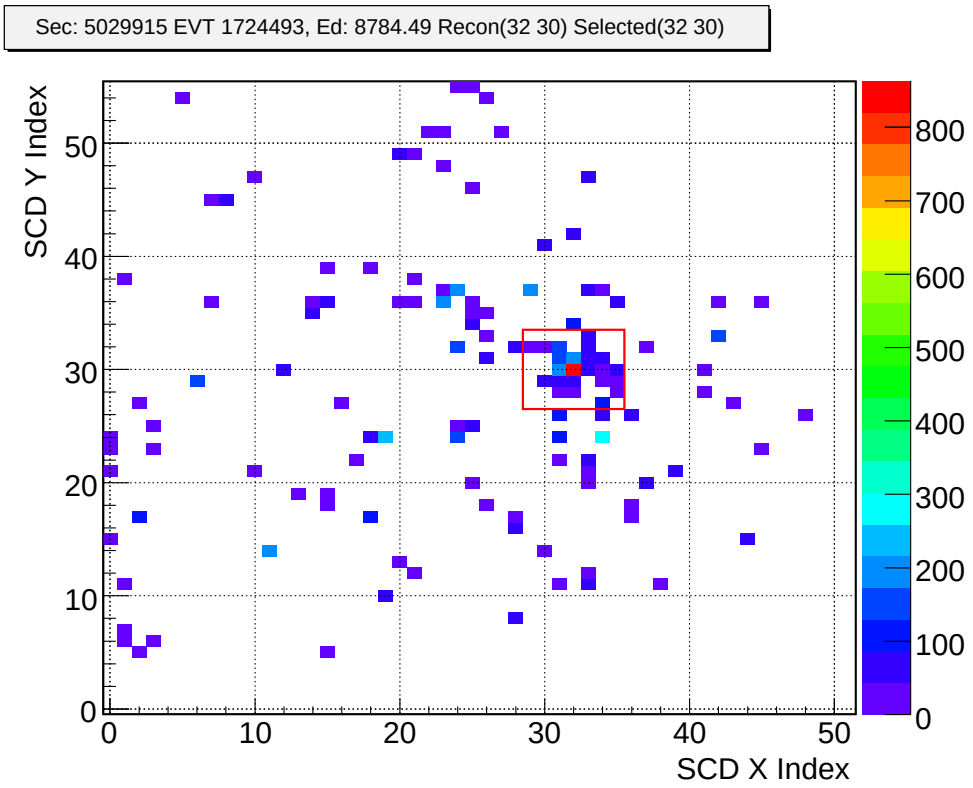

Figure 4.3: Extrapolated hit position from the reconstructed trajectory on SCD plane and signal in the SCD channels. A red square indicates the 7×7 pixel search area for the maximum signal around the hit position from the reconstructed trajectory. In this example, the hit position (x-index, y-index) from the reconstruction is (32, 30) pixel in the SCD, and the maximum signal is in the (32, 30) pixel, as well.

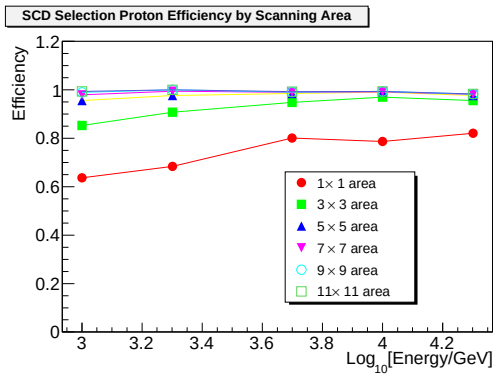

(a) SCD efficiency over energy for search area with proton simulations

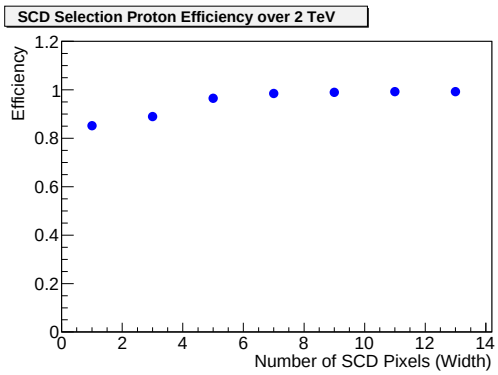

(b) SCD efficiency over search area with proton simulations

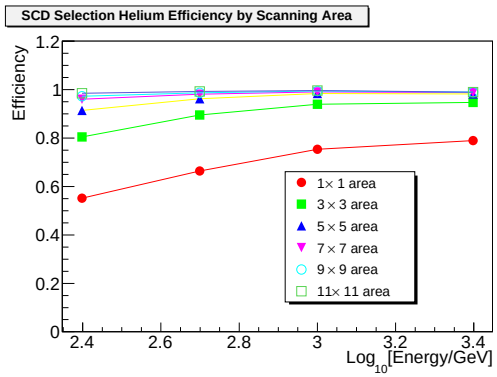

(c) SCD efficiency over energy for search area with helium simulations

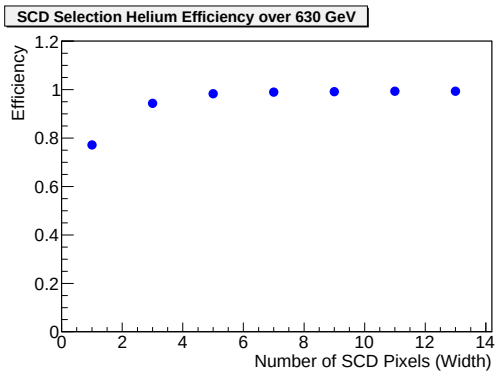

(d) SCD efficiency over search area with helium simulations

Figure 4.4: SCD circle of confusion comparison with MC simulations considering dead layer effects in the calorimeter. With MC proton and helium results, SCD selection efficiency for different searching areas were compared. The dead layer effect in the calorimeter was included in the calorimeter reconstruction. With a search area of 7 × 7 pixels, the selection efficiency is about 99%. To be conservative, a search area with 7 × 7 pixels is used for the analysis.

charge with the SCD can be expressed as,

$$Z_{SCD} = \sqrt{\frac{\text{Path length corrected SCD signal}}{\text{SCD signal at MIP}}}, \tag{4.1}$$

where the path length corrected SCD signal is the signal output normalized to sensor thickness and the SCD signal for a Minimum Ionizing Particle (MIP) was obtained with the most probable value of the Gaussian convoluted Landau function for helium fit, which was found to be 35.5 ADC units. Events with Z $<$ 1.7 were selected as protons, while events with 1.7 $<$ Z $<$ 2.7 were selected as helium nuclei. The charge resolutions, estimated by a full-width-half-maximum of the distribution, are $\sim$0.15 e and $\sim$0.2 e for protons and helium nuclei, respectively.

The proton and helium losses due to dE/dx Landau tails were corrected by charge selection efficiencies, which will be discussed in section 4.5.2. The proton events in the helium range were removed as a background in the helium selection, and the helium events in the proton range were removed as a background in the proton selection, which will be discussed in section 4.5.3. Unstable SCD channels identified by their large root mean square pedestal variations throughout the flight were excluded from the analysis. Including dead and noisy channels, $\sim$15% of the total 2,912 SCD channels were masked, which were included in the charge selection efficiencies.

4.3 Energy Measurement

An ionization calorimeter is the only practical way to measure the energy of protons and helium nuclei above $\sim$1 TeV, but calorimeters with full containment of

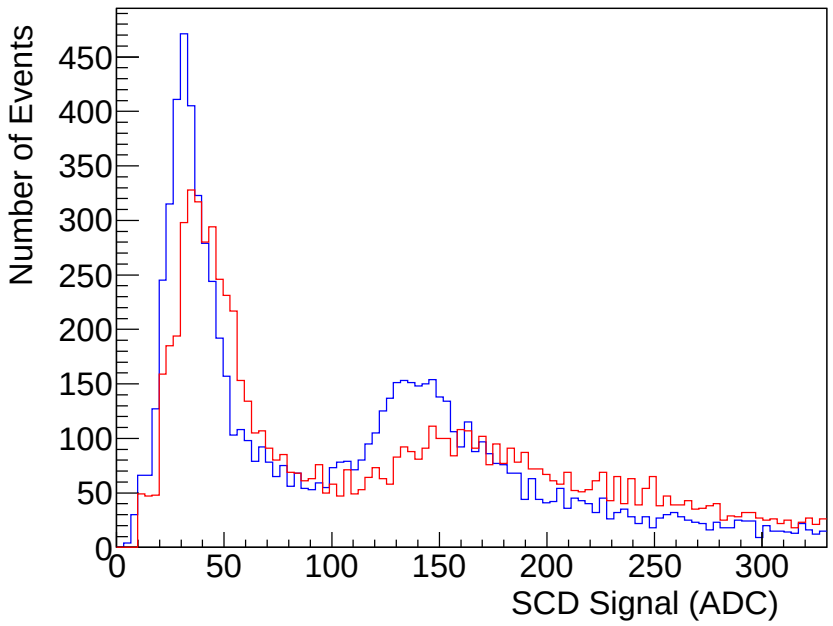

Figure 4.5: The SCD signal distribution for proton and helium before (red) and after (blue) path length correction. After path length correction, the SCD signal distribution shows better charge resolution. The peak around 35 ADC units is for protons and peak around 140 ADC units is for helium nuclei.

hadronic showers are too massive to be incorporated into space-based or balloon-borne experiments [75]. A thin calorimeter offers a practical approach but the calorimeter calibration requires the use of accelerator beam particles having known energy.

The CREAM calorimeter was designed to measure the energy deposit from showers initiated by nuclei with energies up to 10^{15} eV and higher. Its sampling fraction for isotropically incident TeV proton showers initiated in the graphite targets is about 0.13% of the parent's energy in the active media.

The CREAM calorimeter was calibrated before the flight with electron beams at the CERN [84]. The signals from the electron beam were compared with electron MC simulation to check each ribbon's response, since signals of electrons are cleaner than those of protons and the process of electron interaction is well-described in simulations. With electron test beam energies of 150 GeV or less, only 8–10 layers around the shower maximum register enough scintillation to allow calibration. To address this, the calibration scan was carried out in three sets of runs exposing the calorimeter from the bottom with additional targets along the beam line. All 50 ribbons in a given layer were exposed to the electron beams by moving the detector in steps of 1 cm vertically or 1 cm horizontally, so the electron beam is centered each time on a different ribbon in each X or Y layer.

The energy deposit expected along the shower core in each layer was calculated using MC simulations of electron showers. Conversion factors from signals in ADC unit to values in MeV were obtained from the ratio of MC simulations of the energy deposits in each ribbon to the measured signals in ADC unit from the calibration

Table 4.2: Quantum efficiency correction [87]

HPD Position on the Box	Beam Test HPD box Quantum Efficiency @440nm (%)	Flight HPD box Quantum Efficiency @ 440nm (%)	Correction Value
1	17.7	18.9	0.937
2	13.81	19.1	0.7230
3	11.18	19.4	0.576
4	15.7	17.8	0.8820
5	19.2	18.5	1.038
6	14.21	19.6	0.725
7	12.86	13.4	0.9597
8	14.49	18.4	0.7875
9	12.9	20.0	0.645
10	12.6	19.0	0.6632

beam test. Figure 4.6 shows examples of deposits in a ribbon from beam test data and MC simulation results. The MC simulations were based on GEANT/FLUKA 3.21 [85, 86]. The signals of the calorimeter in ADC unit were corrected for the HPD quantum efficiency (QE_i) and gain difference ($G_{HV,i}$) from the different HPD high-voltage settings between the beam test (10.5 kV) and the flight (6 kV). The corrections for HPD quantum efficiency, which was only for 10 HPDs on a replaced HPD box, are shown in Table 4.2. The correction for the gain difference was estimated by a gain ratio with different HVs of 10.5 to 6 kV from the extrapolated test results with several LED inputs at different HV settings (Figure 4.7(a)), and the mean gain correction was found to be 2.0 $\pm$ 0.08 as shown in Figure 4.7(b). The signal in each channel was corrected with the gain correction value from the corresponding HPD.

Inter-calibration between the low- and mid- energy ranges, and between the

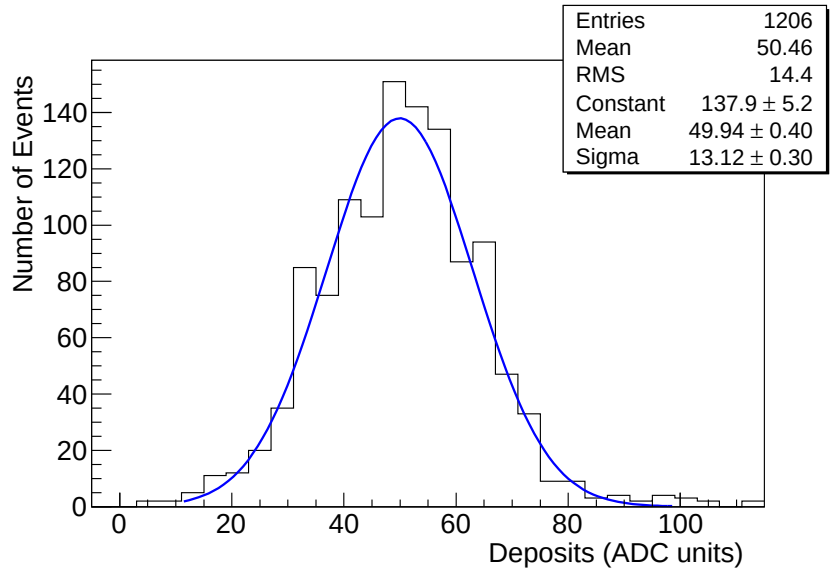

(a) Deposits of 150 GeV electron from beam test data

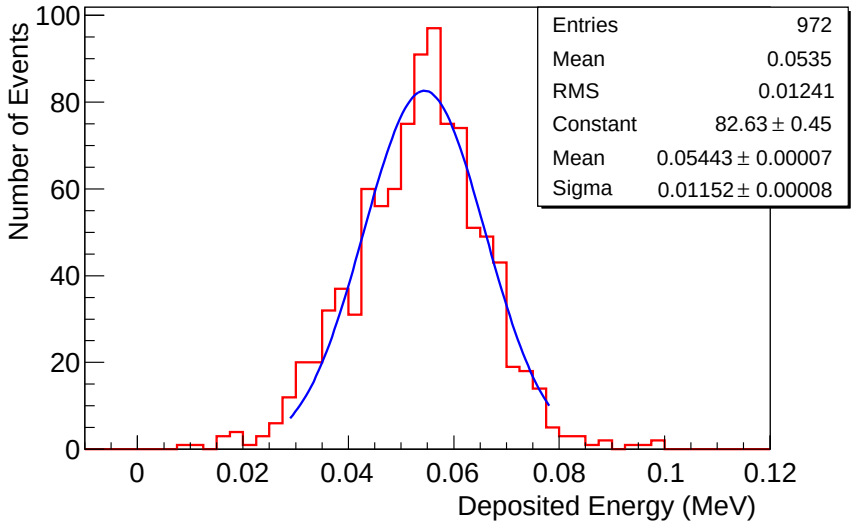

(b) Deposits of 150 GeV electron from MC simulations

Figure 4.6: Examples of deposits in a ribbon from (a) a 150 GeV electron beam and (b) its MC simulations. The energy deposit distributions shown are from a ribbon in the 6^{th} layer with the electron beam incident on the top of the calorimeter.

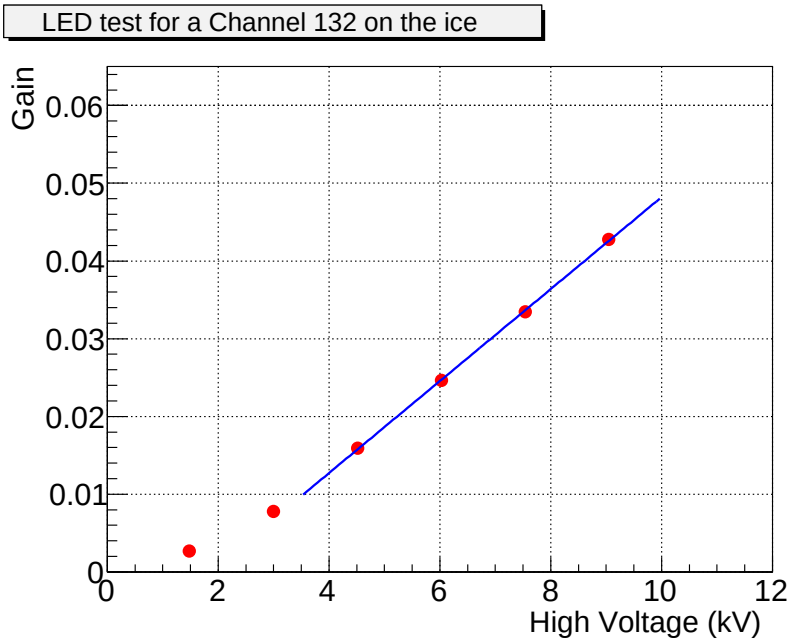

(a) HPD LED gain in a channel with LED input

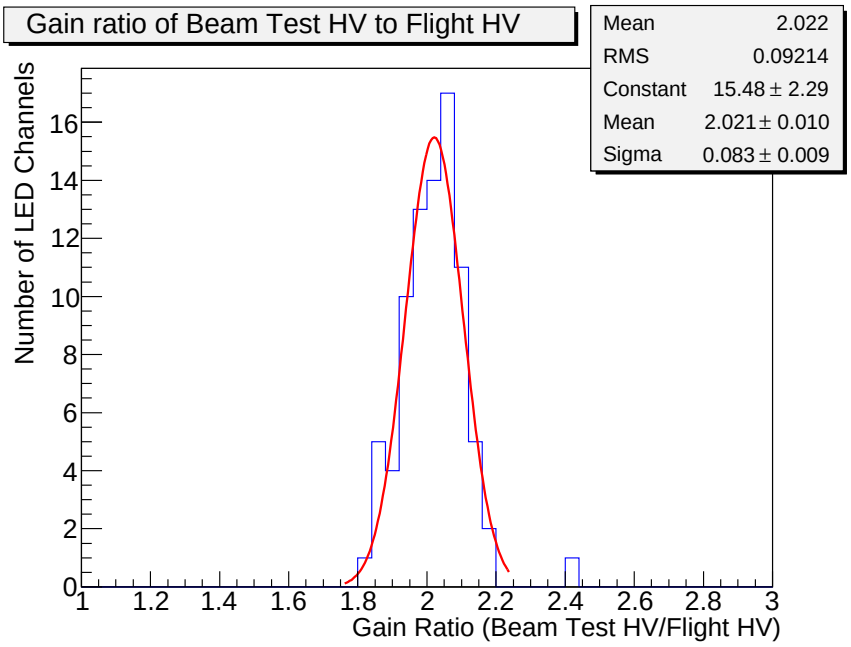

(b) Gain ratio distribution

Figure 4.7: HPD LED gain in a channel with LED input signal and ratio distribution of all LED channels. (a) The HPD gain over different HVs in an LED channel shows good linearity. (b) The gain ratio with HPD HVs of 10.5 kV to 6 kV from extrapolated LED test results was 2.0.

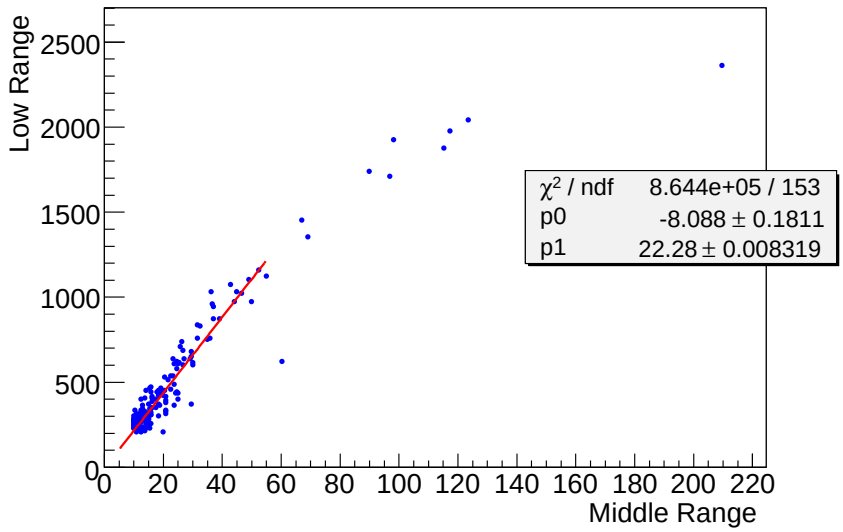

Figure 4.8: Example of a scattered distribution with signals from low and middle range channels at the same event. In each channel, the ratio was estimated with a linear fit in the linear region.

mid- and high- energy ranges were carried out with flight data by comparing the signals from two ranges of the same ribbon generated by the same shower, as shown in Figure 4.8. The correction for middle range channels (R_{LM}) was estimated with a linear fit in the linear region. None of the proton and helium event candidates saturated in the middle range, so high range optical division was not needed for this analysis. Figure 4.9 shows that the energy spectrum is extended to the higher energy ranges when signals from middle range channels are corrected.

The calibration constant in the i^{th} ribbon for the flight data can be expressed as,

$$\text{Calibration Constant} = \frac{\text{MC Deposited Energy (MeV)}}{\text{Deposits in Beam Test (ADC units)}} \cdot \text{QE} \cdot \text{G}_{HV} \cdot \text{R}_{LM}. \quad (4.2)$$

The calorimeter, HDS, and SCD were also exposed to nuclear fragments (A/Z

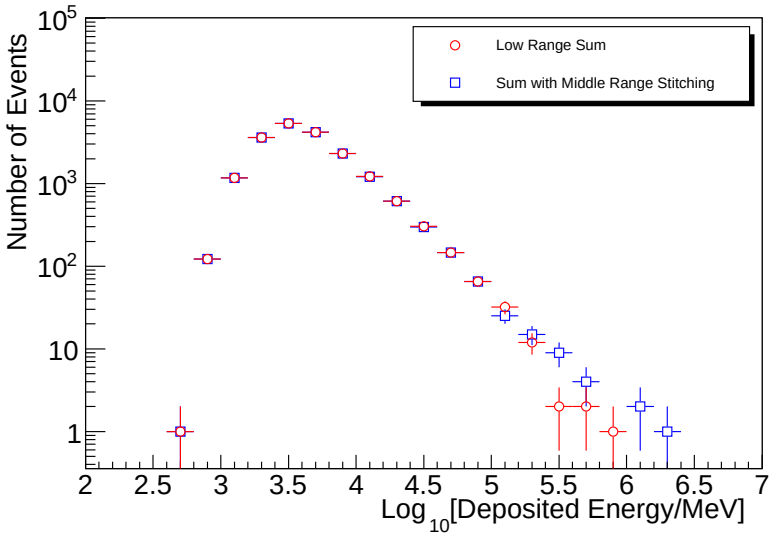

Figure 4.9: Deposited energy distribution of the calorimeter events with and without middle range stitching. After stitching, events are extended to the higher energy bins.

= 2) of a 158 GeV/nucleon Indium beam at CERN [71,88–90]. The energy response was linear up to the maximum beam energy of ∼9 TeV, which corresponds to the energy of heaviest fragments (Figure 4.10). Above the available accelerator beam energy, MC simulations indicate that the calorimeter response is quite linear in the CREAM measurement energy range. The simulations also indicate that the calorimeter energy resolution is nearly energy independent. Nevertheless, our energy deconvolution included corrections for the small energy dependence of the energy resolution due to shower leakage [91].

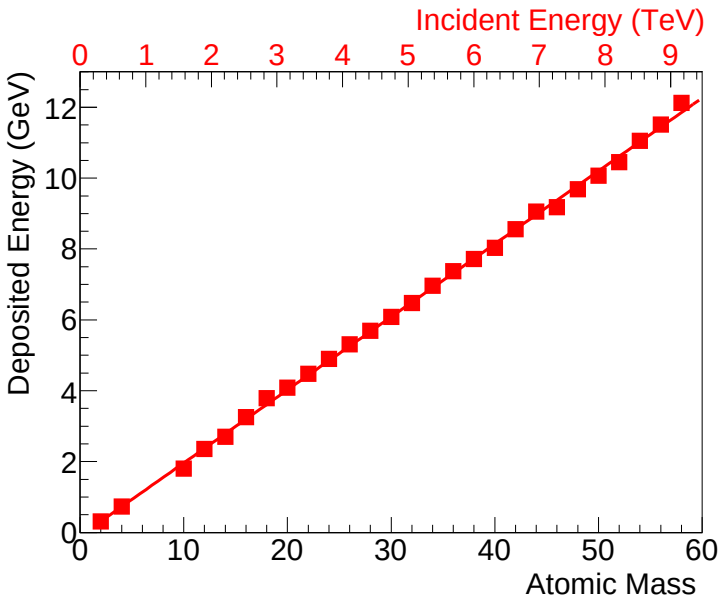

Figure 4.10: Deposited energies from selected charges with fragmented indium beam data versus mass number A. Mass number A in each event corresponds to an incident energy based on the fact that only particles with 158 GeV/nucleon satisfying A/Z=2 are selected. The deposited energy shows good linearity up to ∼9 TeV.

4.4 Spectral Deconvolution

Entries in the deposited energy bins were deconvolved into incident energy bins using matrix relations. The counts, $N_{inc,i}$, in incident energy bin i were estimated from the measured counts, $N_{dep,j}$, in deposited energy bin j by the relation [92, 93],

$$N_{inc,\,i} = \sum_{j} P_{i,j} N_{dep,\,j}, \tag{4.3}$$

where matrix element $P_{i,j}$ is the probability that events in the deposited energy bin j are from incident energy bin i. The matrix element $P_{i,j}$ was estimated from the response matrix generated by MC simulation results obtained separately for protons and helium nuclei (Figure 4.11). The response matrix and corresponding deconvolution matrix were generated and tested by varying the indices between -2.5 and -2.8. We verified that the flux deconvolution process was not sensitive to the assumed spectral index used, within that range, to generate the matrix elements (Figure 4.12).

The MC simulations for helium and heavier nuclei used event generators FRITIOF/RQMD/DPMJET-II [94,95] interfaced to the GEANT/FLUKA 3.21 simulation package. FRITIOF [96] is based upon semi-classical considerations of string dynamics for high-energy hadronic collisions. The relativistic quantum molecular dynamics (RQMD) is a semi-classical microscopic approach which combines classical propagation with stochastic interactions [97]. It was adopted for simulations of heavy ions for energies in the center-of-mass frame less than 5 GeV/nucleon. DPMJET-II [98, 99] was based on the dual parton model, a framework for hadron-hadron interactions and production in hadron-nucleus and nucleus-nucleus collisions

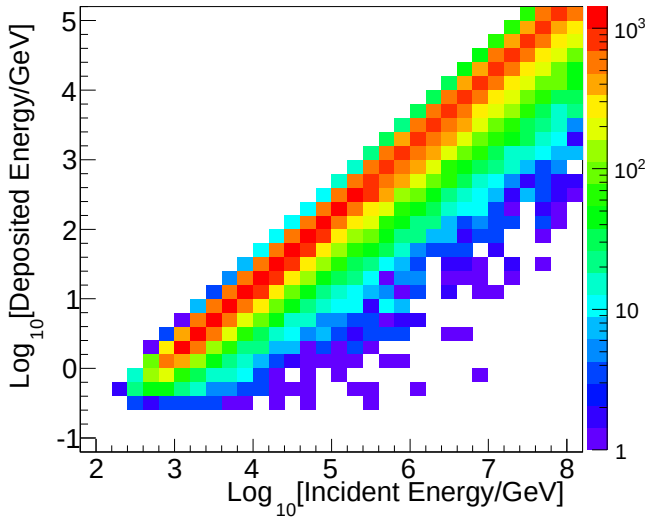

(a) Response matrix with proton MC

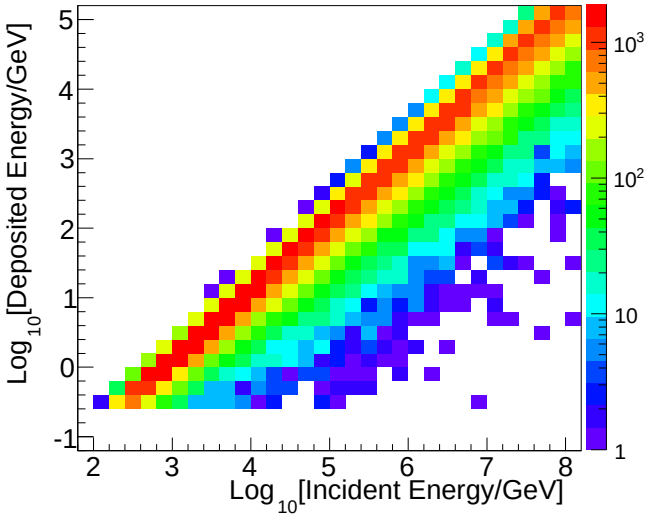

(b) Response matrix with helium MC

Figure 4.11: Response matrices for protons and helium nuclei from MC simulations. The deposited energy distribution for each incident energy bins were generated with MC simulations.

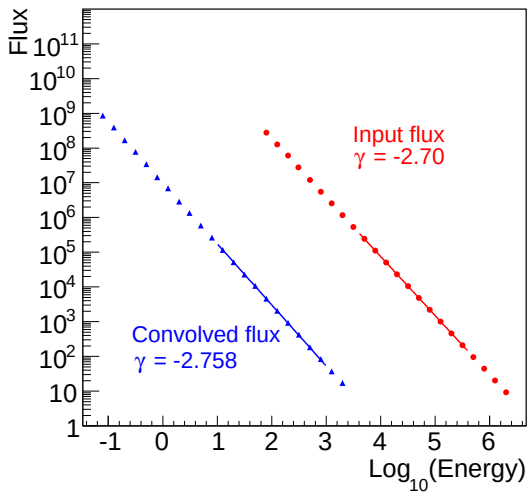

(a) Convolved spectrum and an input spectrum with the index -2.7

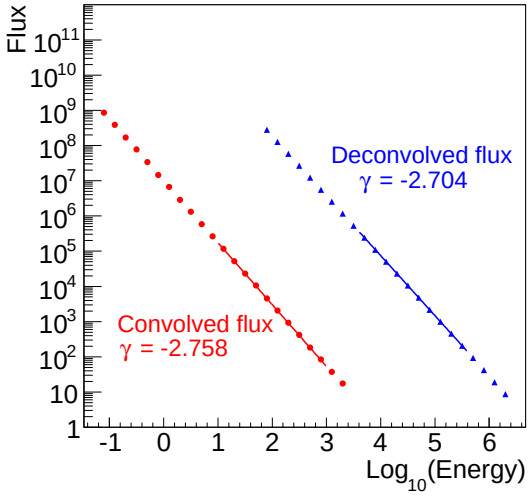

(b) Deconvolved spectrum and the convolved spectrum from (a)

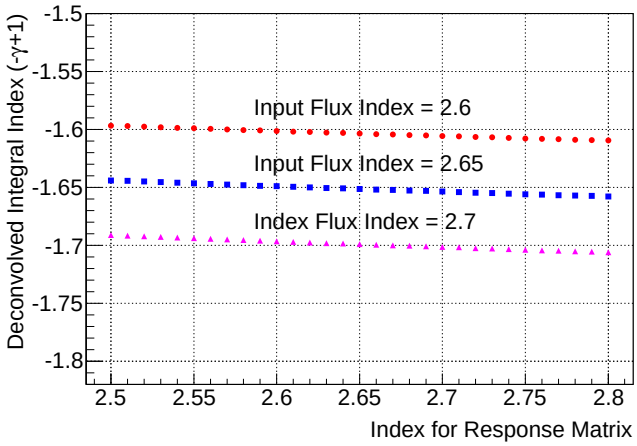

(c) Indices of the deconvolved spectrum for various input spectral indices used in MC event generation

Figure 4.12: Convolved and deconvolved spectra. (a) An input flux (red) with the index of -2.70 was convolved with a response matrix. (b) The convolved flux (red) with index -2.758 was deconvolved with a matrix for deconvolution. The deconvolved flux (blue) has an index of -2.704, which is consistent with the input flux. (c) The deconvolution process was not sensitive to the assumed spectral index used to generate the matrix elements. The index difference ($\sim$0.004) between the deconvolved and input spectra was much smaller than fit uncertainties ($\pm$ 0.02).

at high energies.

4.5 Absolute Flux

The measured spectra were corrected for the instrument acceptance as shown below to obtain the absolute flux F:

$$F = \frac{dN}{dE} \cdot \frac{(1-\delta)}{GF \cdot \varepsilon \cdot T \cdot \eta}, \tag{4.4}$$

where dN is the number of events in an energy bin, dE is the energy bin size, GF is the raw geometry factor, ε is the efficiency, δ is the background, T is the live-time, and η is the survival fraction after accounted for atmospheric attenuation.

4.5.1 Geometry Factor

The raw geometry factor, GF, was calculated to be 0.43 ± 0.01 m^2 sr (Figure 4.13) using 10,000 isotropic events at each energy from MC simulations [100] by requiring the extrapolated calorimeter trajectory of the incident particle to traverse the SCD active area and the bottom of the calorimeter. When the stability of geometry factors were estimated by increasing the number of events up to 600,000 events, the geometry factor became nearly constant after 200,000 events (Figure 4.14), which is consistent to the results with 10,000 events (Figure 4.13).

The geometry factor of a detector with two rectangular areas having sides of length $2X_1$, $2Y_1$ and $2X_2$, $2Y_2$, separated by Z can be calculated analytically [101] by the following integration:

$$GF_{analytical} = Z^4 \int_{-X_1}^{X_1} \int_{-Y_1}^{Y_1} \int_{-X_2}^{X_2} \int_{-Y_2}^{Y_2} \frac{dx_1\, dy_1\, dx_2\, dy_2}{\{Z^2 + (x_2 - x_1)^2 + (y_2 - y_1)^2\}^3}. \tag{4.5}$$

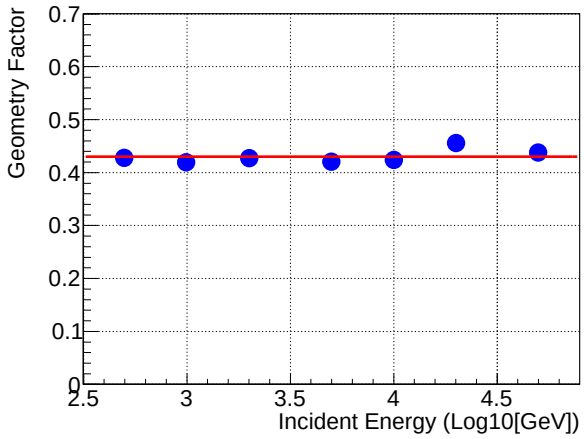

Figure 4.13: Geometry factor from MC simulations at different energies. The geometry factor was estimated by requiring the extrapolated calorimeter trajectory to traverse both the SCD active area and the bottom of the calorimeter. The geometry factors, calculated with 10,000 isotropic events at each energy, was 0.43 ± 0.01 m^2 sr.

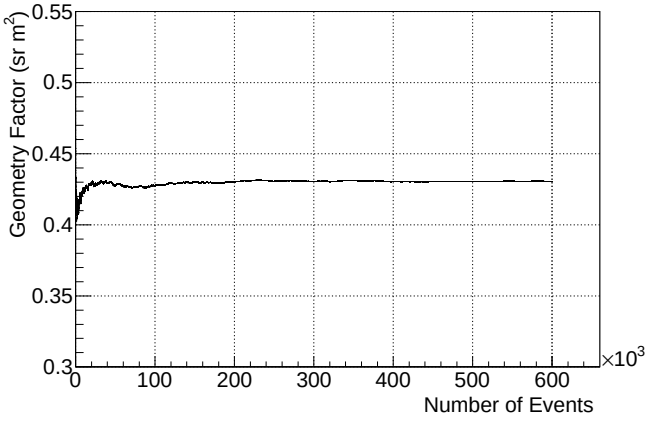

Figure 4.14: Stability of the geometry factor with MC simulations. The geometry factor became constant (0.43 m^2 sr) with more than 200,000 events.

With the CREAM geometry of the bottom of calorimeter (50×50 cm^2), the SCD active area (79.5×77.9 cm^2), and the distance between two planes ($Z = 35.1$ mm), the analytically calculated geometry factor is 0.43 m^2 sr, which is consistent with the result from MC simulations.

4.5.2 Efficiency

The efficiency, ε in Equation 4.4 includes efficiencies from all analysis steps, including trigger condition, reconstruction condition, charge identification, and removal of events with late interactions:

$$\varepsilon = \varepsilon_{trig}\ \varepsilon_{rec}\ \varepsilon_{int}\ \varepsilon_{charge}\,. \tag{4.6}$$

The trigger efficiency, ε_{trig}, was obtained from MC simulations of the fraction of events satisfying the trigger condition among all events within the geometry, i.e., passing through the bottom of the calorimeter and the SCD active area. The trigger efficiency is energy dependent at low energies where the trigger is not fully efficient. Above 3 TeV, it is nearly constant around 76% for protons and 91% for helium nuclei, respectively. The reconstruction efficiency, ε_{rec}, was taken to be the ratio of events satisfying the reconstruction and trigger conditions to events satisfying only the trigger condition. The reconstruction efficiency was 98% for protons and 99% for helium nuclei, respectively, based on MC simulations. The event selection efficiency for removing events with late interactions, ε_{int}, was estimated with the MC simulations, and was 90% protons and 96% for helium nuclei. The charge efficiency, ε_{charge}, takes into account lost events due to noisy or dead SCD channels,

Table 4.3: Efficiencies for protons and helium nuclei

Efficiency	Proton (%)	Helium (%)
Trigger efficiency	76 ± 2	91 ± 1
Reconstruction efficiency	98 ± 1	99 ± 1
Late interaction event efficiency	90 ± 1	96 ± 1
Charge selection efficiency	77 ± 2	67 ± 1

interactions above the SCD, mis-identified charges such as events in Landau tails. It was calculated to be 77% for protons and 67% for helium nuclei, using MC simulations. As shown in Table 4.3, the charge selection efficiency is dominant for both of protons and helium nuclei and the trigger efficiency is another dominant factor for protons.

The trigger efficiency for proton and helium nuclei cannot be estimated with the flight data, since we do not know how many un-triggered events occurred. With flight data, the efficiency of removing events due to late interaction position and charge identification for combined proton and helium nuclei was estimated. It is not as accurate as individual MC simulations because the composition (abundance) of incident particles is unknown. When the abundance ratio of protons and helium nuclei was assumed to be 1:1 and the abundance of heavy nuclei above helium nuclei was ignored, the efficiencies were 68 % from the flight data and 67 % for the MC simulations. The event selection efficiency from the flight data could be compared with that from MC simulations in similar way.

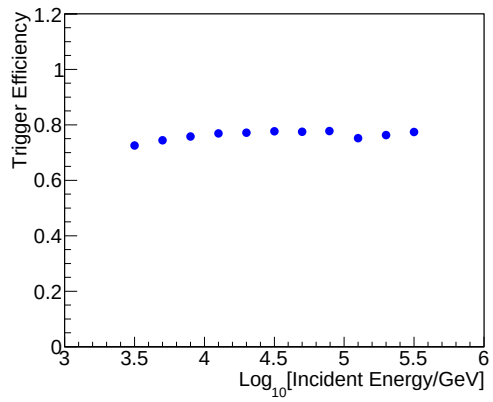

(a) Proton trigger efficiency

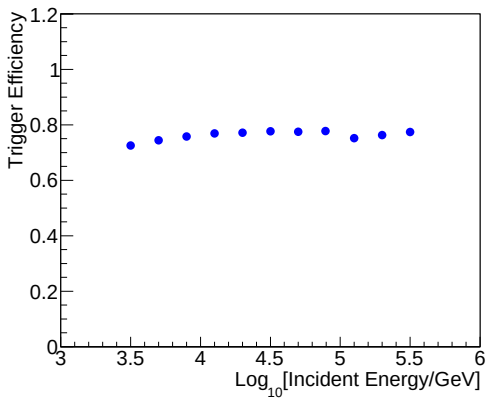

(b) Helium trigger efficiency

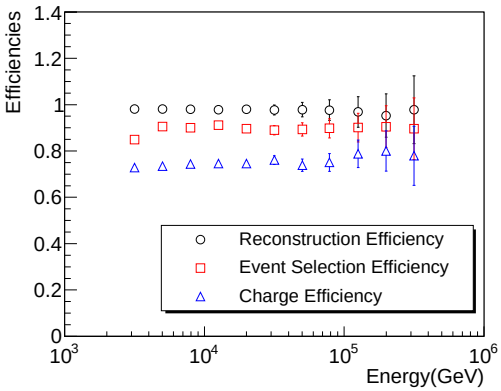

(c) Proton efficiencies

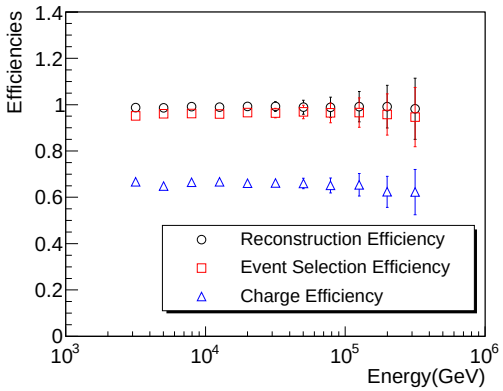

(d) Helium efficiencies

Figure 4.15: Trigger (filled circles), reconstruction (open circles), event selection with interaction position (squares), and charge selection (triangles) efficiencies of protons and helium nuclei with isotropic events from MC simulations, following a power-law distribution. The efficiencies for protons and helium nuclei appear nearly constant above a few TeV.

4.5.3 Background

The primary background is comprised of events with misidentified charge, which result mainly from secondary particles generated by interactions above the SCD, or by particles back-scattered from the calorimeter. This is the case for protons. However, there is an additional cause of misidentified events for helium nuclei, namely, the proton dE/dx Landau tail. Misidentified event counts of protons and helium nuclei were estimated from MC simulations with a power-law input spectrum (Figure 4.16). Due to the Landau tails, back-scattered and secondary particles, 5.1% of measured protons were misidentified helium nuclei and 6.8% of measured helium nuclei were misidentified protons. About 0.2% of incident carbon nuclei were misidentified as protons, and 2.8% of incident carbon nuclei were misidentified as helium nuclei (Figure 4.17). According to the relative elemental abundance of the incoming cosmic rays using the expected energy spectra of individual cosmic-ray nuclei from Wiebel-Sooth (1998) [61], less than 1% of trigger and reconstructed protons and helium events are from secondary particles. Additional background comes from the events that are not within the geometry, but which satisfy the trigger and reconstruction conditions; they are either entering the instrument acceptance from outside the SCD area or exiting the side of the calorimeter instead of the bottom. According to MC simulations, this is about 3.6% and 4.0% of the selected events for protons and helium nuclei, respectively. As shown in Table 4.4, the total background was 9% for protons and 11% for helium nuclei.

Table 4.4: Backgrounds for protons and helium nuclei

Background	Proton (%)	Helium (%)
Background from reconstruction	3.6 ± 0.1	4.0 ± 0.2
Background from mis-identified charge	5.1 ± 0.2	6.8 ± 0.2
Total	8.7 ± 0.2	10.8 ± 0.2

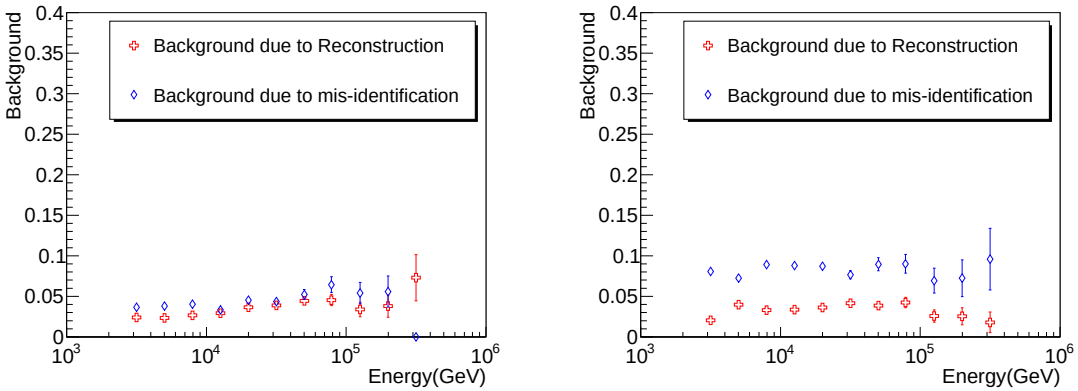

(a) Proton background

(b) Helium background

Figure 4.16: Backgrounds of (a) protons and (b) helium nuclei with MC simulations. Backgrounds due to reconstruction (diamond) and mis-identified charge (cross) were estimated with isotropic events following a power-law distribution.

4.5.4 Interactions in the Air

The attenuation loss due to the atmospheric overburden, 3.9 ± 0.4 g/cm^2, was corrected for survival fractions of protons and helium nuclei. The air depth was measured by pressure sensors during the flight (Figure 3.4). Interaction cross sections have been measured in many fixed target experiments, and cross sections are known up to a few tens of GeV, as shown in Table 4.5 [102–104]. We used the cross section formula from Hagen *et al.* (1977) [102] to calculate interaction lengths

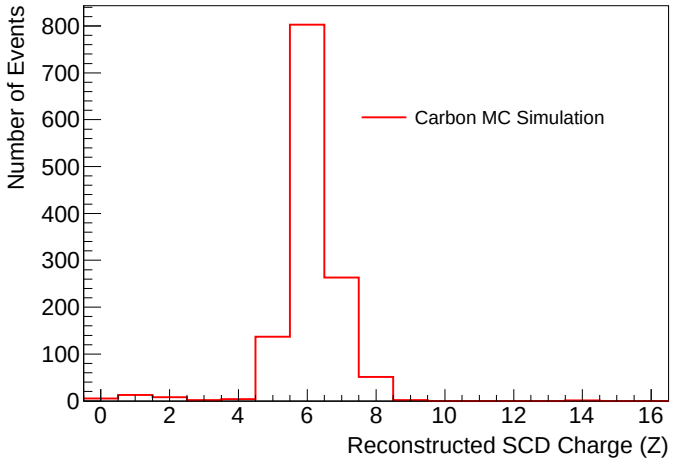

(a) MC 10 TeV carbon reconstructed charge

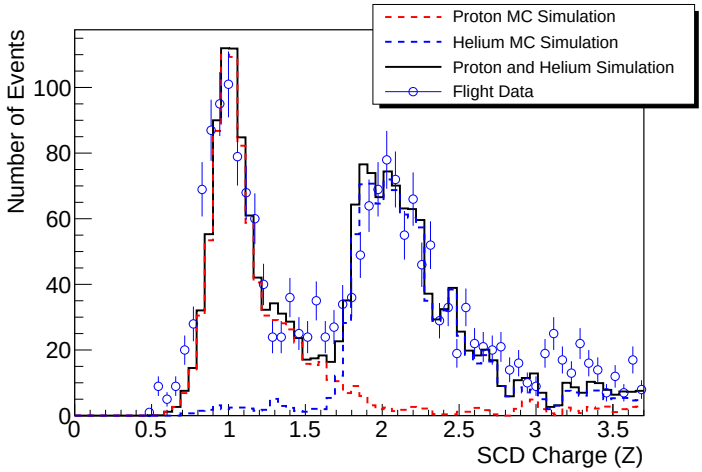

(b) Proton and helium distribution of MC simulations and flight data in an energy bin

Figure 4.17: (a) Examples of reconstructed charge with 10 TeV isotropic carbon MC simulation and (b) protons and helium nuclei distribution in an energy bin from MC simulation and flight data. Mis-identified events as protons or helium nuclei from the carbon nuclei are about 0.2% and 2.8%, respectively. Considering the relative elemental abundance, the effect from carbon to protons and helium nuclei is less than 1%. Most of the backgrounds are from protons and helium nuclei.

and survival fractions for protons and helium nuclei, although results from the three equations in Table 4.6, were fairly close. The mean incident angle of 35°, estimated from the flight data, was used to estimate the losses. The survival fraction, η, used to characterize atmospheric attenuation was determined to be 95% for protons and 91% for helium nuclei. The effect due to the mean incident angle was considered as systematic uncertainty.

The ratio of secondary to primary protons and helium nuclei in the atmosphere above GeV energies has been reported [105,106]. Papini *et al.* (1996) [104] calculated that the secondary to primary proton ratio at an air depth of 3 g/cm^2 was less than 1% above 40 GeV, and the secondary to primary helium nuclei ratio was less than 2% at 10 GeV/nucleon. Our MC simulations showed that the fraction of secondary protons and helium nuclei produced from carbon and iron nuclei interactions in the air was less than 1% at 10 TeV.

Table 4.5: Equations for cross section calculation

Paper	Equation
Hagen *et al.* [102]	$\sigma_R = \pi r_0^2 (A_P^{1/3} + A_T^{1/3} - \kappa)^2$
	where $r_0 = 1.29 \times 10^{-13} cm$
	and $\kappa = 1.189 \exp[-0.05446 \min(A_P, A_T)]$
Webber *et al.* [103]	$\sigma_{p+A} = 40 A^{0.71} (mb)$
	$\sigma_{^4He+A} = (5.69 + 6.58 A^{0.355})^2 \quad (mb)$
Papini *et al.* [104]	$\sigma_{CD}(mb) = 56.7 (A_C^{1/3} + A_D^{1/3} - 1.25)^2$

Table 4.6: Interaction loss for protons and helium nuclei in the air

	Vertical Incidence		35°Incidence Angle	
Method	Proton (%)	Helium (%)	Proton (%)	Helium (%)
Hagen *et al.*	4.4 ±1.3	7.7 ±2.2	5.4 ±1.6	9.3 ±2.6
Webber *et al.*	4.5 ±1.4	8.3 ±2.4	5.5 ±1.6	10.1 ±2.8
Papini *et al.*	4.3 ±1.3	6.9 ±1.8	5.3 ±1.5	8.3 ±2.4

4.5.5 Live Time Fraction Estimation

A finite time is required by the detector to process an event, which is related to the duration of the pulse signal in the detector. During this period, a detector may or may not remain sensitive to other events, depending on the detector type. When the detector is insensitive, events arriving during this period are lost. This period is called dead-time and the periods excluding dead-time are called live-time.

Out of 42 days of the flight, the stable period (Table 4.1) was about 24 days when no commands were sent, e.g. for power-cycle or high-voltage adjustments. After dead-time correction, the live-time, T, of 1,099,760 s was used for this analysis.

In the CREAM instrument, the live-time counter in the housekeeping system is designed to provide the accumulated time over which the detector is sensitive, as mentioned in Section 2.6.1 and Section 2.6.4. However, the live-time counter during the first CREAM flight was not functioning.

The live-time fractions for the first flight were estimated using the total trigger rate and a relation between the live-time fraction and total trigger rate from the second flight. The live-time fractions during the second CREAM flight, were between 60 - 90%, as shown in Figure 4.18(a). As expected, the live-time fractions

were reduced when the total trigger rate increased (Figure 4.18(b)). However, two groups of distributions between the live-time fraction and the total trigger rate were found in the second CREAM flight housekeeping data. As shown in Figure 4.18(c) and 4.18(d), two groups were separated by a packet buffer level value in the housekeeping information and the slopes of the two groups were estimated for the "empty packet buffer" case and "non-zero packet buffer" case. The SFC was packaging and transmitting events from the packet buffer in the SFC memory when the buffer was filled, and when the buffer was empty, the SFC waited for the events while checking the buffer level. These two groups should also appear in the first CREAM flight data, since there was no change in the SFC between the first and second flight. Therefore, the total trigger rate distribution of the first flight was divided into two cases of empty packet buffer and non-zero buffer, as shown in Figure 4.19, in order to use the slopes of the live-time fraction and total trigger rate from the second flight. The ratios of the two cases are 91.1% with an empty packet buffer and 8.9% with non-zero packet buffer.

In addition, two peaks were found in the total trigger rate distributions of the first CREAM flight. The peak around 20 Hz was the expected total trigger rate, and there was another peak near 5 Hz in both cases. It was found that frequent TCD time-out messages are related to those low trigger rate periods, according to the log files. The TCD time-out message was generated when the SFC did not receive the data from the TCD after receiving the TCD trigger signal. This "TCD time-out" only occurred once in a while. However, when it happened repeatedly within 30 s, it caused the trigger rate to drop below 10 Hz. This was fixed for later flights.

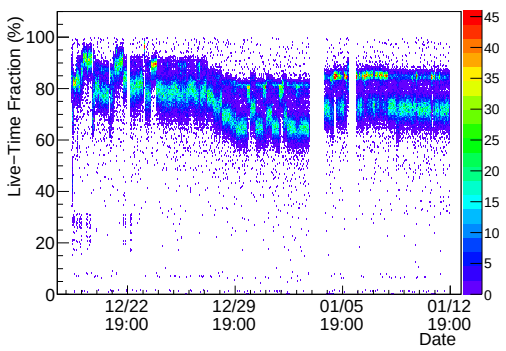

(a) Live-time fraction

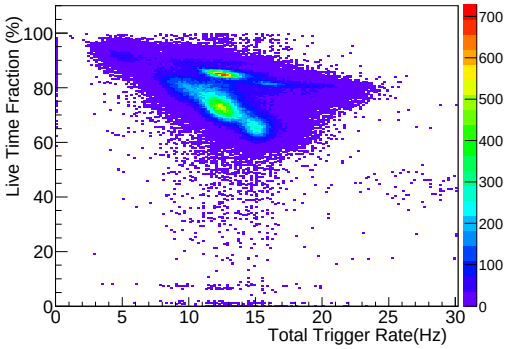

(b) Live-time fraction vs total trigger rate

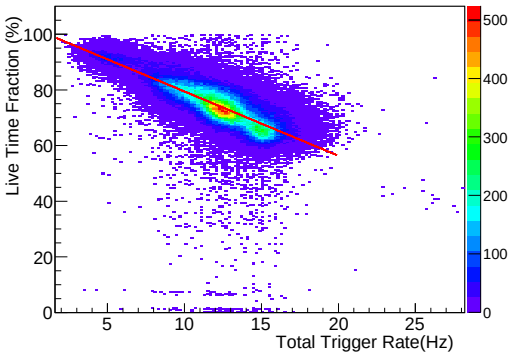

(c) Live-time fraction vs total trigger rate when a packer buffer is empty

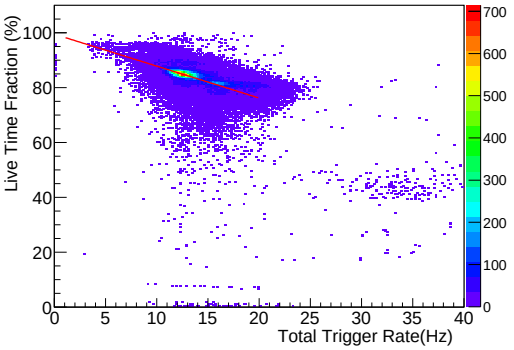

(d) Live-time fraction vs total trigger rate when a packet buffer is filled

Figure 4.18: The live-time fraction and the total trigger rate in the second CREAM flight. (a) The live-time fractions during the second CREAM flight were between 60 - 90%. (b) The live-time fractions were reduced when the total trigger rate increased. (c and d) The two groups of distributions between the live-time fractions and the total trigger rate can be separated by a packet buffer level.

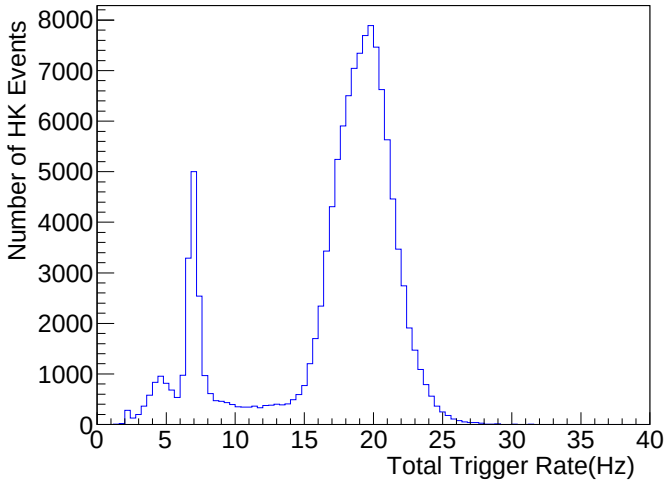

(a) Total trigger rate with empty packet buffer

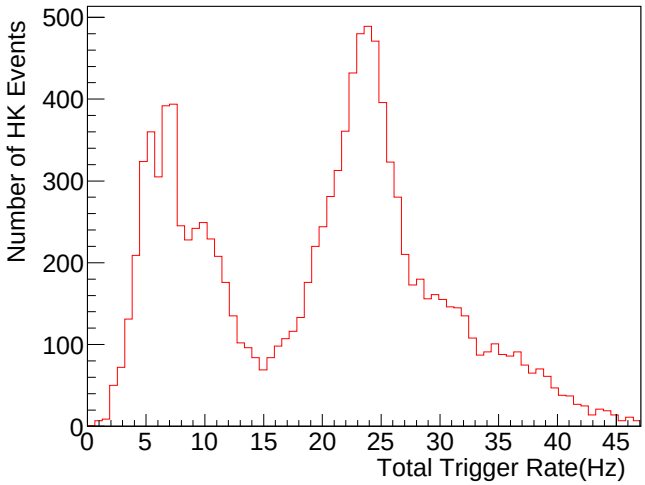

(b) Total trigger rate with non-zero packet buffer

Figure 4.19: The total trigger rate in the first CREAM flight (a) when a packet buffer is empty and (b) when it is filled. Those two cases could be related with the activities of the SFC since SFC is packaging and transmitting events from the packet buffer when the buffer if filled, while SFC is waiting for the events and checking the buffer level when the buffer is empty.

The low-rate periods, which are less than 10 Hz, were not included in the estimated live-time, since no calorimeter events were measured during those time periods. In each data file, the live-time was calculated with data collection time in that data file and the average live-time fraction from the estimated average total trigger rate for two cases: with empty buffer level and non-zero buffer level. For example, a data file, "20041225-000150.dat" with 11788 events for 591 s (19.9 Hz), the live-time fractions were 50.9% for empty buffer periods and 73.8% for non-zero buffer periods, from Figure 4.18. Considering the appearance frequencies of the empty buffer and non-zero buffer periods, 91.1% and 8.9%, respectively, the average live-time fraction for this file is 53% and its live-time is 282 s. The live-time for first CREAM flight was obtained by accumulating a live-time of each data file. The uncertainty from calculating data collection time excluding low-rate periods was about 6%.

4.5.6 Energy-Bin Representation.

For the number of events (dN) in each energy bin with upper and lower energy limits, E_{j+1} and E_j, respectively, ($dE = E_{j+1}$–E_j), the differential flux is dN/dE at E_m, where E_m can be taken as the arithmetic mean of E_j and E_{j+1} in logarithmic range, or else using a suitably weighted average of E_j and E_{j+1}. We also investigated an alternative procedure to determine E_m, as suggested by Lafferty (1995) [107]:

$$f(E_m) = \frac{1}{E_{j+1} - E_j} \int_{E_j}^{E_{j+1}} f(E) dE. \tag{4.7}$$

For a power-law spectrum, $f(E) = AE^{-\gamma}$, E_m can be calculated as,

$$E_m = \Big(\frac{E_{j+1}^{1-\gamma} - E_j^{1-\gamma}}{(E_{j+1} - E_j)(1-\gamma)} \Big)^{-1/\gamma}. \tag{4.8}$$

In our analysis, the difference between E_m and the center of the bin in logarithmic range is less than 1%.

4.6 Uncertainty Estimation

The uncertainty of the flux can be derived from Equation 4.4,

$$\Big|\frac{\Delta F}{F}\Big|^2 = \Big|\frac{\Delta(\frac{dN}{dE})}{(\frac{dN}{dE})}\Big|^2 + \Big|\frac{\Delta\varepsilon}{\varepsilon}\Big|^2 + \Big|\frac{\Delta GF}{GF}\Big|^2 + \Big|\frac{\Delta\delta}{1-\delta}\Big|^2 + \Big|\frac{\Delta T}{T}\Big|^2 + \Big|\frac{\Delta\eta}{\eta}\Big|^2, \tag{4.9}$$

where,

$$\Big|\frac{\Delta\varepsilon}{\varepsilon}\Big|^2 = \Big|\frac{\Delta\varepsilon_{trig}}{\varepsilon_{trig}}\Big|^2 + \Big|\frac{\Delta\varepsilon_{rec}}{\varepsilon_{rec}}\Big|^2 + \Big|\frac{\Delta\varepsilon_{int}}{\varepsilon_{int}}\Big|^2 + \Big|\frac{\Delta\varepsilon_{charge}}{\varepsilon_{charge}}\Big|^2. \tag{4.10}$$

The statistical uncertainty in each energy bin was estimated by the relation $\delta N_{inc,i} = \delta(\sum_j P_{i,j} N_{dep,j})$, considering 68.3% Poisson confidence limits by Feldman and Cousins (1998) [108]. Several sources of systematic uncertainties were identified. The systematic uncertainties for efficiencies and backgrounds were estimated within each energy range to account for the energy-dependent effects determined using MC simulations. They are summarized in Table 4.3 and 4.4. Efficiency uncertainties were about 1-2%, and background uncertainties were about 5%.

The geometry factor uncertainty from MC simulations was 2% for both protons and helium nuclei (Section 4.5.1). The precision of the estimated live-time fraction was about 3.3%. The precision was not varied, but its accuracy was shifted due to the total trigger rate variations or threshold changes. The accuracy of estimated

dead-time for the accumulated data due to irregular detector response was about 2.6%. The overall uncertainties for the estimated live-time were 4% for both protons and helium nuclei.

The systematic uncertainties for the survival fractions in the atmosphere were calculated analytically. The p-p cross section difference between 10 TeV and 100 TeV is about 28%, according to the most recent reference from the Particle Data Group [74]. Using a conservative estimate of 30% for cross section uncertainties, the estimated uncertainties of survival fractions were 2% and 3% for protons and helium nuclei, respectively. In addition, the uncertainties of estimated loss in the atmosphere due to the average of the incident angle were 1% for proton and 1.6% for helium nuclei.

The energy calibration accuracy was found to be 1%. The systematic uncertainties of the measured number in each energy bin, considering 1% of energy calibration accuracy, were 3% for both protons and helium nuclei. Also, the uncertainty due to spectral deconvolution were estimated using matrices from MC simulations with a range of input flux indices, including measured spectral index uncertainties, and found to be less than 1%.

The overall systematic uncertainty was found to be 9% for both protons and helium nuclei. This systematic uncertainty is energy independent. It does not change the spectral shape, but it might shift the normalization of the spectra up or down.

Chapter 5

Results

5.1 Proton and Helium Indices

The measured proton fluxes from 2.5 TeV to 250 TeV and helium fluxes from 630 GeV/nucleon to 63 TeV/nucleon at the top of the atmosphere are given in Tables 5.1 and 5.2. Statistical uncertainties are shown as well. The CREAM proton and helium spectra are each consistent with a single power-law over the measured range, as shown in Figure 5.1. The spectra for protons and helium nuclei are represented by

$$\frac{d\Phi}{dE} = \Phi_0 E^{-\beta} \quad (\mathrm{m}^2\,\mathrm{sr}\,\mathrm{s}\,\mathrm{GeV/nucleon})^{-1}. \tag{5.1}$$

The best-fit parameters for the spectra for protons and helium nuclei, respectively, are given by:

$$\Phi_{0,p} = (7.8 \pm 1.9) \times 10^3 \quad (\mathrm{m}^2\,\mathrm{sr}\,\mathrm{s})^{-1}(\mathrm{GeV/nucleon})^{1.66}, \tag{5.2}$$

$$\beta_p = 2.66 \pm 0.02, \tag{5.3}$$

and

$$\Phi_{0,He} = (4.2 \pm 0.8) \times 10^2 \quad (\mathrm{m}^2\,\mathrm{sr}\,\mathrm{s})^{-1}\,(\mathrm{GeV/nucleon})^{1.58}, \tag{5.4}$$

$$\beta_{He} = 2.58 \pm 0.02. \tag{5.5}$$

The spectral indices were calculated by the weighted least square method

Table 5.1: Measured proton flux

Energy (GeV)	Proton Flux ±Uncertainty $(m^2\ sr\ s\ GeV)^{-1}$
$2.5 \times 10^3 - 4.0 \times 10^3$	$(3.72 \pm 0.10) \times 10^{-6}$
$4.0 \times 10^3 - 6.3 \times 10^3$	$(1.10 \pm 0.04) \times 10^{-6}$
$6.3 \times 10^3 - 1.0 \times 10^4$	$(3.19 \pm 0.19) \times 10^{-7}$
$1.0 \times 10^4 - 1.6 \times 10^4$	$(9.47 \pm 0.80) \times 10^{-8}$
$1.6 \times 10^4 - 2.5 \times 10^4$	$(2.80 \pm 0.35) \times 10^{-8}$
$2.5 \times 10^4 - 4.0 \times 10^4$	$(8.1 \pm 1.5) \times 10^{-9}$
$4.0 \times 10^4 - 6.3 \times 10^4$	$(2.2 \pm 0.6) \times 10^{-9}$
$6.3 \times 10^4 - 1.0 \times 10^5$	$(6.1^{+2.6}_{-2.2}) \times 10^{-10}$
$1.0 \times 10^5 - 1.6 \times 10^5$	$(1.8^{+1.2}_{-0.9}) \times 10^{-10}$
$1.6 \times 10^5 - 2.5 \times 10^5$	$(4.2^{+5.4}_{-3.4}) \times 10^{-11}$

Table 5.2: Measured helium flux

Energy (GeV/nucleon)	Helium Flux ±Uncertainty $(m^2\ sr\ s\ GeV/nucleon)^{-1}$
$6.3 \times 10^2 - 1.0 \times 10^3$	$(1.42 \pm 0.04) \times 10^{-5}$
$1.0 \times 10^3 - 1.6 \times 10^3$	$(4.35 \pm 0.16) \times 10^{-6}$
$1.6 \times 10^3 - 2.5 \times 10^3$	$(1.31 \pm 0.07) \times 10^{-6}$
$2.5 \times 10^3 - 4.0 \times 10^3$	$(3.83 \pm 0.31) \times 10^{-7}$
$4.0 \times 10^3 - 6.3 \times 10^3$	$(1.27 \pm 0.14) \times 10^{-7}$
$6.3 \times 10^3 - 1.0 \times 10^4$	$(4.19 \pm 0.64) \times 10^{-8}$
$1.0 \times 10^4 - 1.6 \times 10^4$	$(1.15 \pm 0.27) \times 10^{-8}$
$1.6 \times 10^4 - 2.5 \times 10^4$	$(3.4^{+1.1}_{-1.0}) \times 10^{-9}$
$2.5 \times 10^4 - 4.0 \times 10^4$	$(8.2^{+4.9}_{-3.8}) \times 10^{-10}$
$4.0 \times 10^4 - 6.3 \times 10^4$	$(2.9^{+2.4}_{-1.5}) \times 10^{-10}$

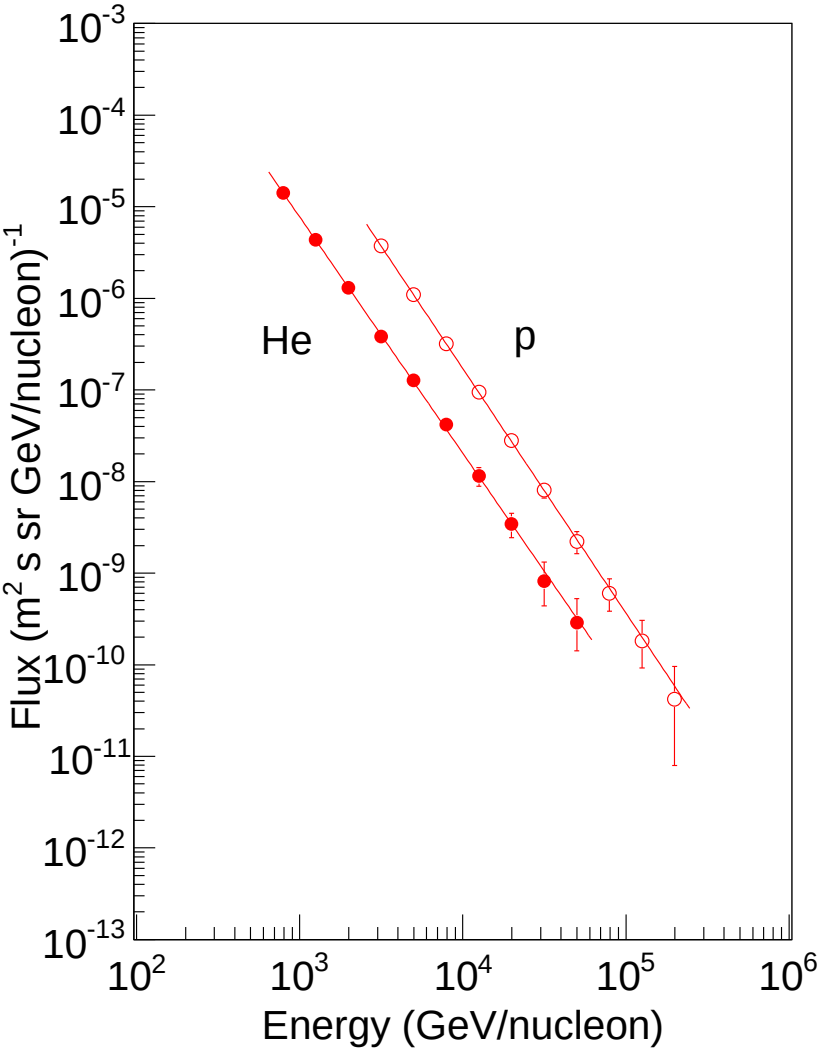

Figure 5.1: Measured CREAM proton and Helium spectra from the CREAM Calorimeter. The statistical uncertainties are shown.

with statistical uncertainties at each energy bin [109] and the maximum likelihood method, which is explained in the following section.

5.2 Maximum Likelihood Method

The maximum likelihood estimator, L, for a Poisson distribution can be expressed by

$$L = \prod_{i=1}^{n} f(n_i, \nu_i), \tag{5.6}$$

where $f(n_i, \nu_i)$ is the Poisson distribution $e^{-\nu_i}\,\nu_i^{n_i}/n_i!$, n_i is the measured number of events in a bin, and ν_i is the expected number of events following a power-law with slope a and intercept b, which can be expressed as

$$\nu_i = \int_{E_i}^{E_{i+1}} \Phi_o E^{-a} dE \tag{5.7}$$

$$= \frac{\Phi_o}{1-a}(E_{i+1}^{1-a} - E_i^{1-a}). \tag{5.8}$$

Then, the likelihood estimator can be expressed as

$$l = \ln L = \ln \prod_{i=1}^{n} f(n_i, \nu_i) \tag{5.9}$$

$$= \sum_{i=1}^{n} \ln \big(\frac{e^{-\nu_i}\,\nu_i^{n_i}}{n_i!}\big) \tag{5.10}$$

$$= \sum_{i=1}^{n} \big(-\nu_i + n_i\,\ln(\nu_i) - \ln(n_i!)\big). \tag{5.11}$$

When L is at maximum, l is also at maximum. At the maximum of L the first derivative of l should be zero,

$$\frac{\partial}{\partial a} l = \frac{\partial}{\partial a} \ln L = 0. \tag{5.12}$$

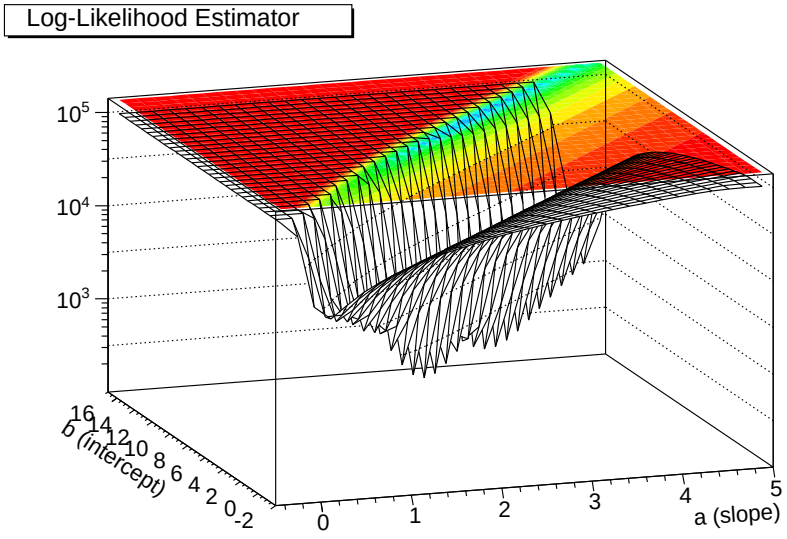

Figure 5.2: An example of maximum likelihood estimator function for proton fluxes. The slope and intercept at the minimum of -ln L was estimated.

$$-\frac{\partial l}{\partial a} = -\sum_{i=1}^{n}\Big[-\frac{10^b}{(1-a)^2}(E_{i+1}^{1-a}-E_i^{1-a})+\frac{10^b}{1-a}\big(-\ln E_{i+1}E_{i+1}^{1-a}+\ln E_iE_i^{1-a}\big) + \frac{n_i}{1-a}-\frac{-\ln E_{i+1}E_{i+1}^{1-a}+\ln E_iE_i^{1-a}}{E_{i+1}^{1-a}-E_i^{1-a}}\Big] \tag{5.13}$$

Finding the exact solution of Equation 5.12 is not simple. The intercept and slope at the minimum of -ln L was found using a minimization function provided by MINUIT2 minimization package [110, 111]. Figure 5.2 shows an example of -ln L with parameters of the slope (a) and the intercept (b).

The uncertainty of the slope was estimated as,

$$\sigma_a = \sqrt{-\frac{\partial^2 l}{\partial a^2}}, \tag{5.14}$$

$$-\frac{\partial^2 l}{\partial a^2} = -\sum_{i=1}^{n}\Big[2\cdot\frac{10^b}{(1-a)^3}(E_{i+1}^{1-a}-E_i^{1-a}) + \frac{10^b}{1-a}\big((\ln E_{i+1})^2E_{i+1}^{1-a}-(\ln E_i)^2E_i^{1-a}\big) - \frac{n_i}{(1-a)^2} - \frac{(\ln E_{i+1})^2E_{i+1}^{1-a}-(\ln E_i)^2E_i^{1-a}}{E_{i+1}^{1-a}-E_i^{1-a}} + \Big(\frac{-(\ln E_{i+1})E_{i+1}^{1-a}+(\ln E_i)E_i^{1-a}}{E_{i+1}^{1-a}-E_i^{1-a}}\Big)^2\Big]. \tag{5.15}$$

5.3 Estimation of Spectral Index and its Uncertainty

The proton and helium spectral indices were estimated with the following minimization methods provided by the MINUIT2 package: SCAN, MIGRAD and SIMPLX minimization methods [110, 112, 113]. As shown in Table 5.3, the indices from all the methods with least square and maximum likelihood methods are consistent. The MIGRAD minimization method of Fletcher [114], works well for nearly all functions. It is a variable-metric method with inexact line search, a stable metric updating scheme, and checks for positive-definiteness. The Nelder and Mead [115] SIMPLX method is a multidimensional minimization routine that is slower than MIGRAD, but it is rather robust with respect to gross fluctuations in the function value. SCAN is intended to minimize and scan one function parameter at a time. It retains the best values after each scan, so it works as a primitive minimization.

Uncertainties of the proton and helium indices were calculated using error estimation methods provided by the MINUIT package: error matrix, MINOS technique, and global minimum search with the IMPROVE function [110, 112, 113, 116]. The error matrix is a by product of the MIGRAD minimizer. This matrix is twice the

inverse of the matrix of second derivatives of the user provided function. MINOS is a generally available program to calculate parameter errors taking into account both parameter correlations and non-linearities. It is applicable only after a good minimum has been found and the error matrix has been calculated. The global minimum search with the IMPROVE function tries to find all local minima with an algorithm of Goldstein and Price [117]. The uncertainties estimated by the error matrix were shown in Table 5.3, and the uncertainties estimated by the MINOS technique, global minimum search, and combination of two are shown in Table 5.4.

As shown in Figure 5.3 and 5.4, the estimated indices for the sub-ranges with two and more consecutive data points show a peak near -2.66 and -2.58 for proton and helium nuclei, respectively. Those peaks, corresponding to the value of constant region (green area) in 2-dimensional plots, were consistent with the indices of proton and helium for the full data range, for both least square and maximum likelihood methods. The results from least square and maximum likelihood methods were consistent, as well. A tendency in the high energy bins can not be concluded at this time, since the statistics are getting sparse in the high energy bins.

Table 5.3: Proton and helium spectral indices and uncertainties from minimization methods

Fit	Minimization Method	Proton Index	Helium Index
Least Square	MIGRAD	2.66 $\pm$0.05	2.58 $\pm$0.03
Least Square	SIMPLX	2.66 $\pm$0.02	2.58 $\pm$0.02
Least Square	SCAN	2.66 $\pm$0.80	2.58 $\pm$0.77
Maximum Likelihood	MIGRAD	2.66 $\pm$0.05	2.58 $\pm$0.04
Maximum Likelihood	SIMPLX	2.66 $\pm$0.02	2.58 $\pm$0.02
Maximum Likelihood	SCAN	2.66 $\pm$n/a	2.58 $\pm$n/a

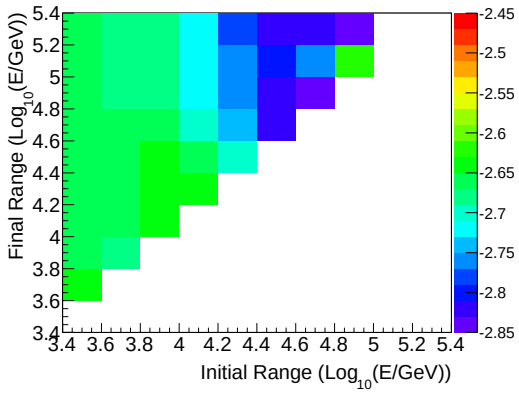

(a) Proton index 2-d map with least square fit

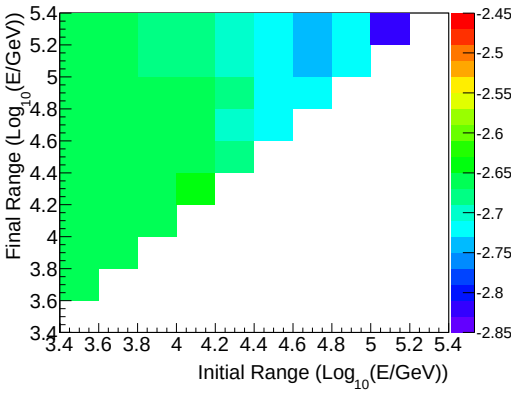

(b) Proton index map with maximum likelihood method

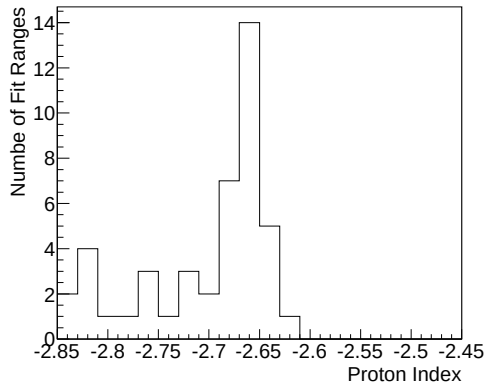

(c) Proton index distribution with least square fit

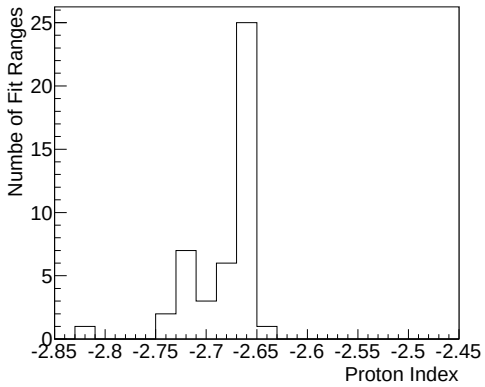

(d) Proton index distribution with maximum likelihood method

Figure 5.3: Proton fit indices map and distribution using least square and maximum likelihood methods. Proton indices using (a) least square and (b) maximum likelihood method from each range with two and more consecutive data points are shown in a 2-d map. The distributions of indices using (c) least square and (d) maximum likelihood method show the most probable index of -2.66.

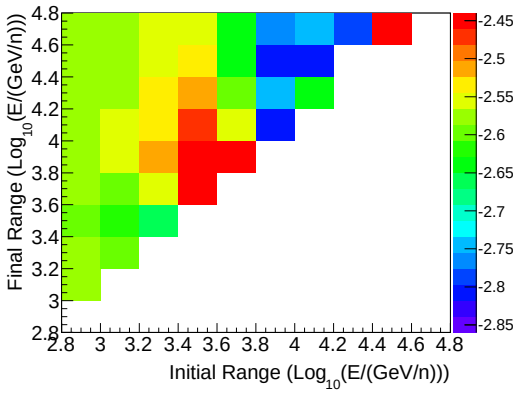

(a) Helium index 2-d map with least square fit

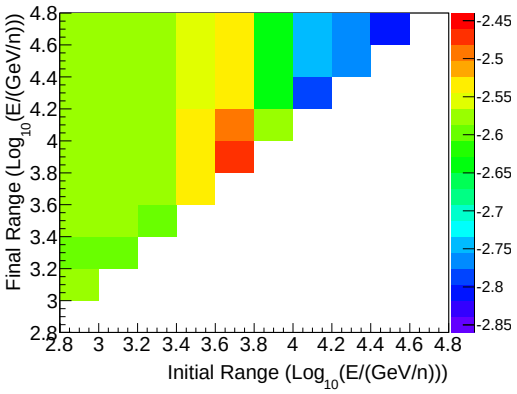

(b) Helium index map with maximum likelihood method

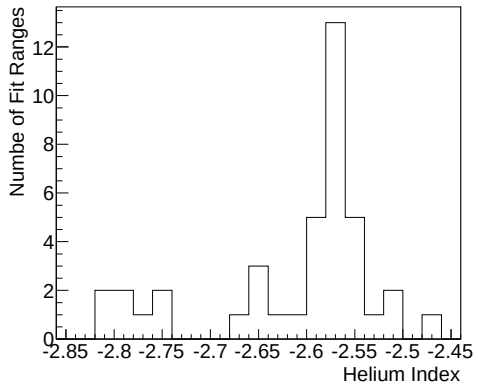

(c) Helium index distribution with least square fit

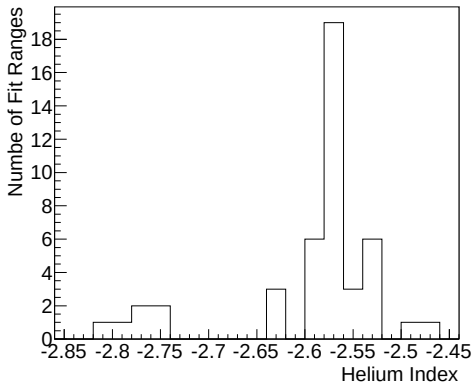

(d) Helium index distribution with maximum likelihood method

Figure 5.4: Helium fit indices map distribution using least square and maximum likelihood method. Helium indices using (a) least square and (b) maximum likelihood method from each range with two and more consecutive data points are shown in a 2-d map. The distribution of indices using (c) least square and (d) maximum likelihood method shows the most probable index of -2.58.

Table 5.4: Proton and helium spectral Indices and uncertainties for uncertainty estimation methods

Error Estimation Method	Proton Index	Helium Index
MINOS error technique	2.66 ±0.03	2.58 ±0.03
IMPROVE function	2.66 ±0.05	2.58 ±0.03
MINOS error & Improved Function	2.66 ±0.03	2.58 ±0.03

The following statistical hypothesis H_0 was used to test the difference of proton and helium spectral indices.

$$H_0 : \beta_p - \beta_{He} = 0 \tag{5.16}$$

Let

$$T = \frac{\beta_p - \beta_{He}}{SE_{\beta_p\beta_{He}}}, \tag{5.17}$$

where $SE_{\beta_p\beta_{He}}$ is an estimator of the common standard deviation for $\beta_p - \beta_{He}$. $SE_{\beta_p\beta_{He}}$ can be expressed as following in terms of standard deviations of proton and helium indices, S_p and S_{He}, from the least square estimation:

$$SE_{\beta_p\beta_{He}} = \sqrt{\frac{{S_p}^2 + {S_{He}}^2}{2}}. \tag{5.18}$$

The random variable T has t-distribution with $2n - 4$ degrees of freedom because each proton and helium data for S_p and S_{he} have $n - 2$ degrees of freedom. The degrees of freedom for CREAM proton and helium fluxes with $n = 10$ are 16. The calculated $SE_{\beta_p\beta_{He}}$ and T value were about 0.03 and 2.67, respectively. The two-tailed p-value was about 0.0169. Therefore, there is less than a 2% chance that our measured proton and helium spectra are consistent with having equal spectral indices.

5.4 Proton to Helium Ratio and Proton plus Helium spectrum

Our proton spectrum is harder (flatter) than previous measurements at lower energies: Alpha Magnetic Spectrometer (AMS) [42], -2.78 ± 0.009 at 10 - 200 GV and Balloon-borne Experiment with Superconducting Spectrometer (BESS) [118], -2.732 ± 0.011 from 30 GeV to a few hundred GeV. Likewise, our helium spectrum is harder than AMS, -2.740 ± 0.01 at 20 - 200 GV and BESS, -2.699 ± 0.040 from 20 GeV/nucleon to a few hundred GeV/nucleon. Figure 5.5 compares our measured spectra with previous measurements: AMS [42][1], BESS [118], Cosmic Anti Particle Ring Imaging Cherenkov Experiment (CAPRICE98) [59], Advanced Thin Ionization Calorimeter (ATIC)-2 [58], Japanese-American Cooperative Emulsion Experiment (JACEE) [119] and Russian-Nippon Joint Balloon experiment (RUNJOB) [48]. The uncertainties shown in the figures represent the statistical uncertainties. Our results are consistent with JACEE where its measurement energy range overlaps with CREAM, but our fluxes are higher, particularly for helium nuclei, than the reported RUNJOB results.

Our proton and helium fluxes are both higher than those expected by extrapolating the power-law fits to the low-energy measurements. Figure 5.6 shows that our TeV spectra are harder than the lower-energy spectra. At 10 TeV/nucleon the helium flux measured by CREAM is about 4 σ higher than the flux expected from a power-law extrapolation of the AMS and BESS helium flux and spectral index,

[1]The published helium flux in GV was converted to the flux in GeV.

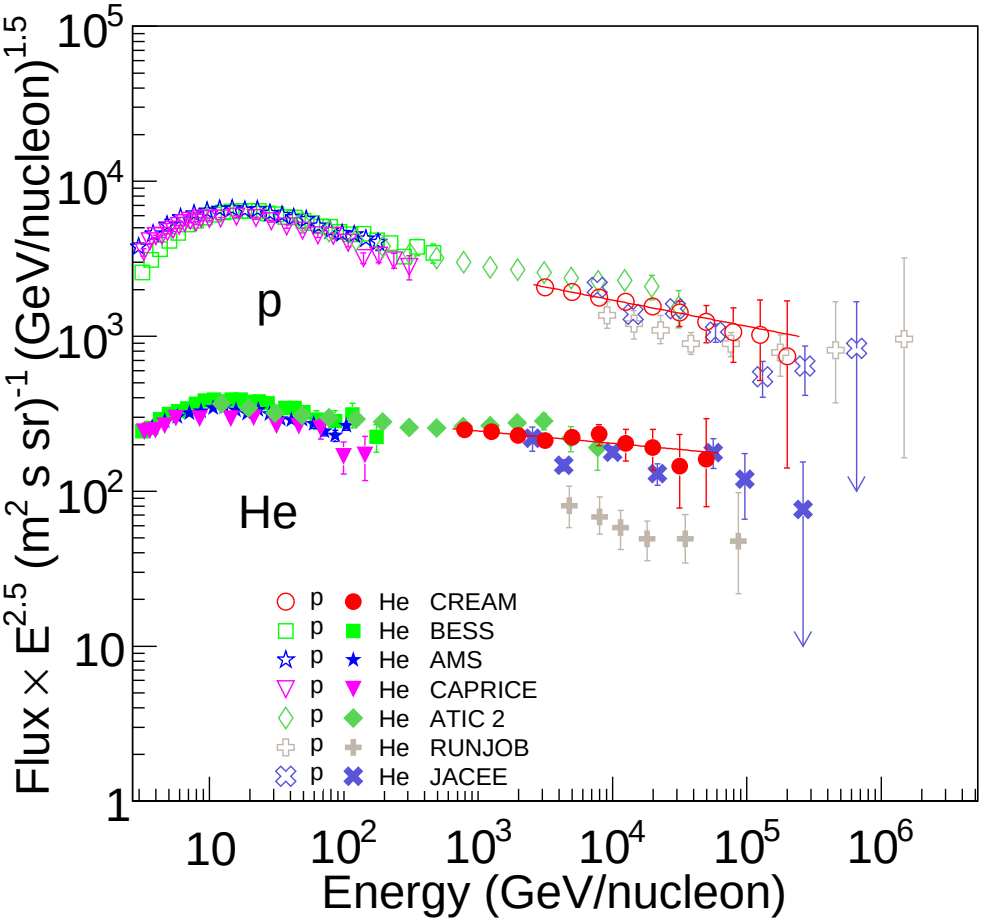

Figure 5.5: Comparison of CREAM proton and helium spectra with previous measurements: AMS [42], ATIC-2 [58], BESS [118], CAPRICE [59], JACEE [119], and RUNJOB [48].

using the definition of significance, S by Li and Ma (1983) [120]:

$$S = \frac{N_S}{\hat{\sigma}(N_S)} = \frac{N_{on} - \alpha N_{off}}{\sqrt{(N_{on} + \alpha^2 N_{off})}}, \tag{5.19}$$

where N_{on} is a count from the expected source, N_{off} is a background count, and α is 1.

Another point is that the proton and helium spectra do not have the same spectral shape. Whether the proton and helium spectra have the same spectral index has been a tantalizing question, mainly because of the limited energy range that individual experiments could cover. The proton to helium ratio as a function of energy can address this question. Our measured ratios (Table 5.5) are compared with previous measurements in Figure 5.7: ATIC-2, CAPRICE94 [121], CAPRICE98, JACEE [122], Low Energy Antiproton experiment (LEAP) [123], and RUNJOB. The CREAM ratios are consistent with JACEE where their energy measurement ranges overlap. Our measured ratio at the top of the atmosphere is 8.8 ± 0.5 for the range from 2.5 TeV/nucleon to 63 TeV/nucleon, which is significantly lower than the ratio of $\sim$20 obtained from the lower-energy measurements.

Table 5.5: Measured proton to helium ratio

Energy (GeV/nucleon)	Ratio $\pm$ Uncertainty
$2.5 \times 10^3 - 4.0 \times 10^3$	(9.6 ± 0.8)
$4.0 \times 10^3 - 6.3 \times 10^3$	(8.8 ± 1.0)
$6.3 \times 10^3 - 1.0 \times 10^4$	(7.6 ± 1.2)
$1.0 \times 10^4 - 1.6 \times 10^4$	(8.2 ± 2.0)
$1.6 \times 10^4 - 2.5 \times 10^4$	$(7.6^{+2.4}_{-2.2})$
$2.5 \times 10^4 - 4.0 \times 10^4$	$(8.8^{+5.0}_{-4.0})$
$4.0 \times 10^4 - 6.3 \times 10^4$	$(7.5^{+6.3}_{-4.2})$

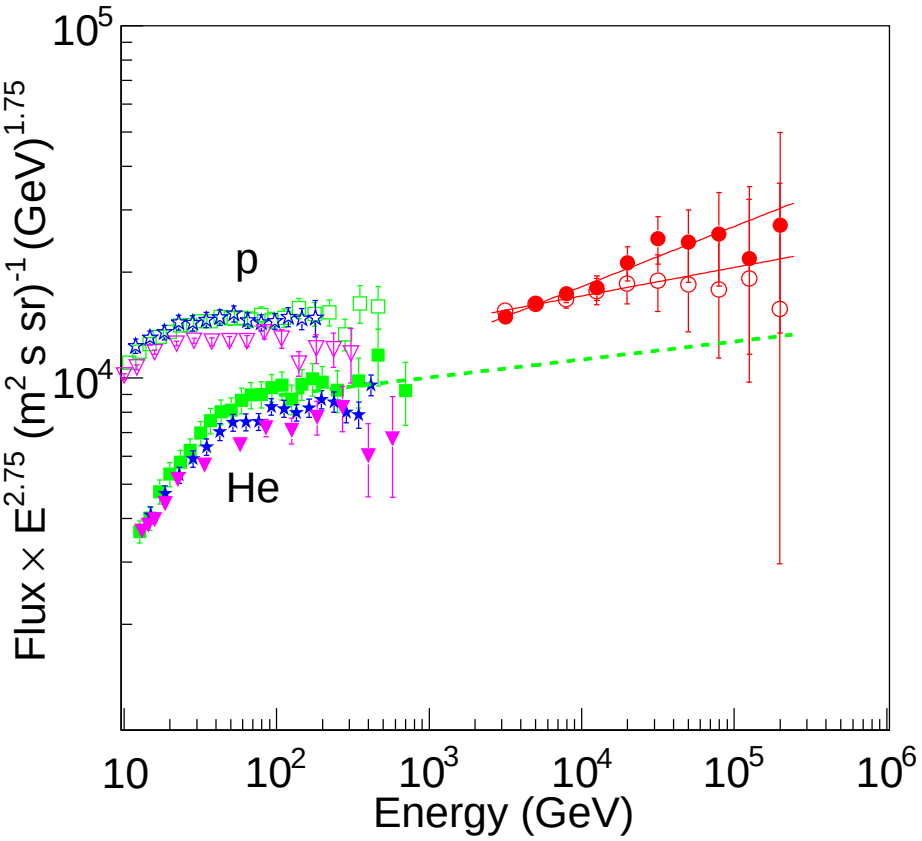

Figure 5.6: Comparison of CREAM proton (open symbols) and helium (filled symbols) spectra with previous measurements [65]: AMS (stars) [42], BESS (squares) [118], and CAPRICE (reversed triangles) [59]. The dashed line represents a power-law extrapolation of the BESS helium flux ($\gamma_{He} = 2.699 \pm 0.040$) through the CREAM energy range.

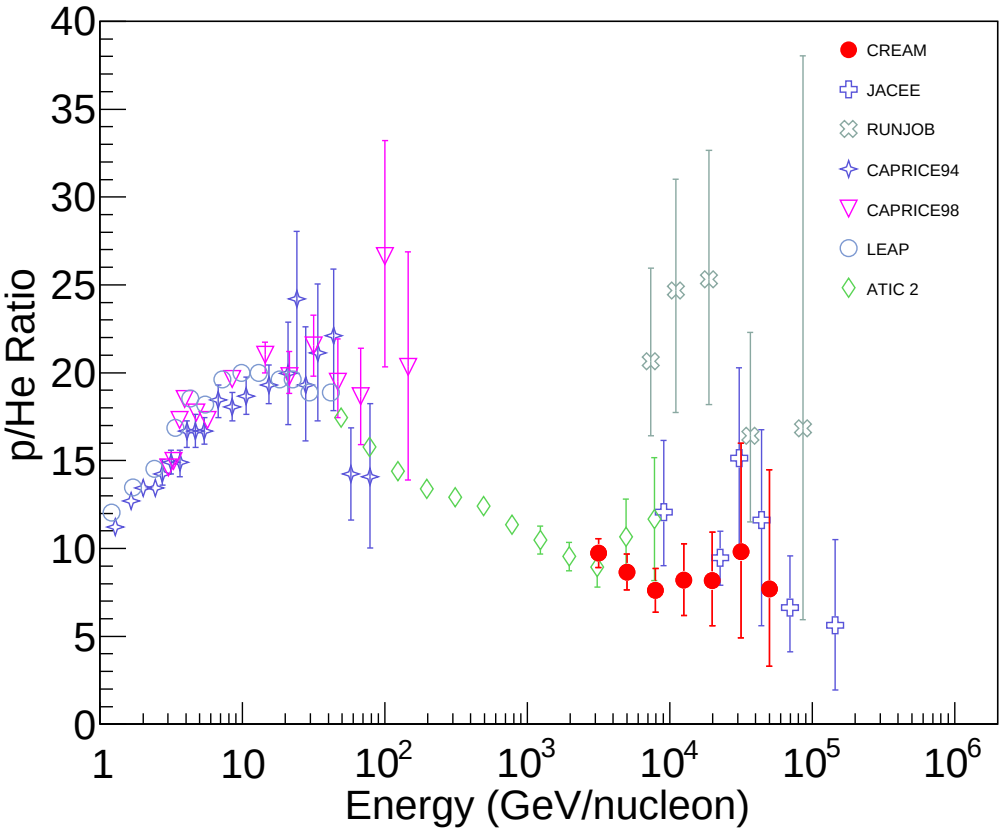

Figure 5.7: Comparison of CREAM proton to helium ratios with previous measurements: ATIC-2 [58], CAPRICE94 [121], CAPRICE98 [59], JACEE [119], LEAP [123] and RUNJOB [48].

Our proton plus helium spectrum is compared with previous direct and indirect all-particle spectra measurements in Figure 5.8 just to check the energy reach. Our flux is lower than other all-particle spectra because heavy nuclei (Z>2) are not included in the plot. CREAM data above 100 TeV have better statistics than previous direct measurements. CREAM data overlap indirect measurements, such as Tibet (2008) [50] and Chicago Air Shower Array-Michigan Anti (1999) [40].

5.5 Helium and Heavier Nuclei Spectra

The CREAM helium spectrum from this analysis and heavier nuclei spectra during the first flight and from the second flight data [70,91] are shown as a function of energy per nucleon and compared with previous measurements in Figure 5.9. The combined data show a harder spectrum for each element above ∼200 GeV/nucleon, which indicates departure from a single power law. Our measured helium flux is consistent with the JACEE results [119]. The CREAM C-Fe data are consistent with the High Energy Astronomy Observatory (HEAO)-3 [124] and Cosmic Ray Nuclei detector (CRN) data [57] at low energies, and the Transition Radiation Array for Cosmic Energetic Radiation (TRACER) data [125] at the energy range where they overlap. A single-power law fit to our data agrees with the TRACER O-Fe power-law fit [91], but the fluxes above 200 GeV/nucleon tend to be higher than a extrapolated single power-law fit. A broken power-law gives a better fit to our heavier nuclei spectra [65].

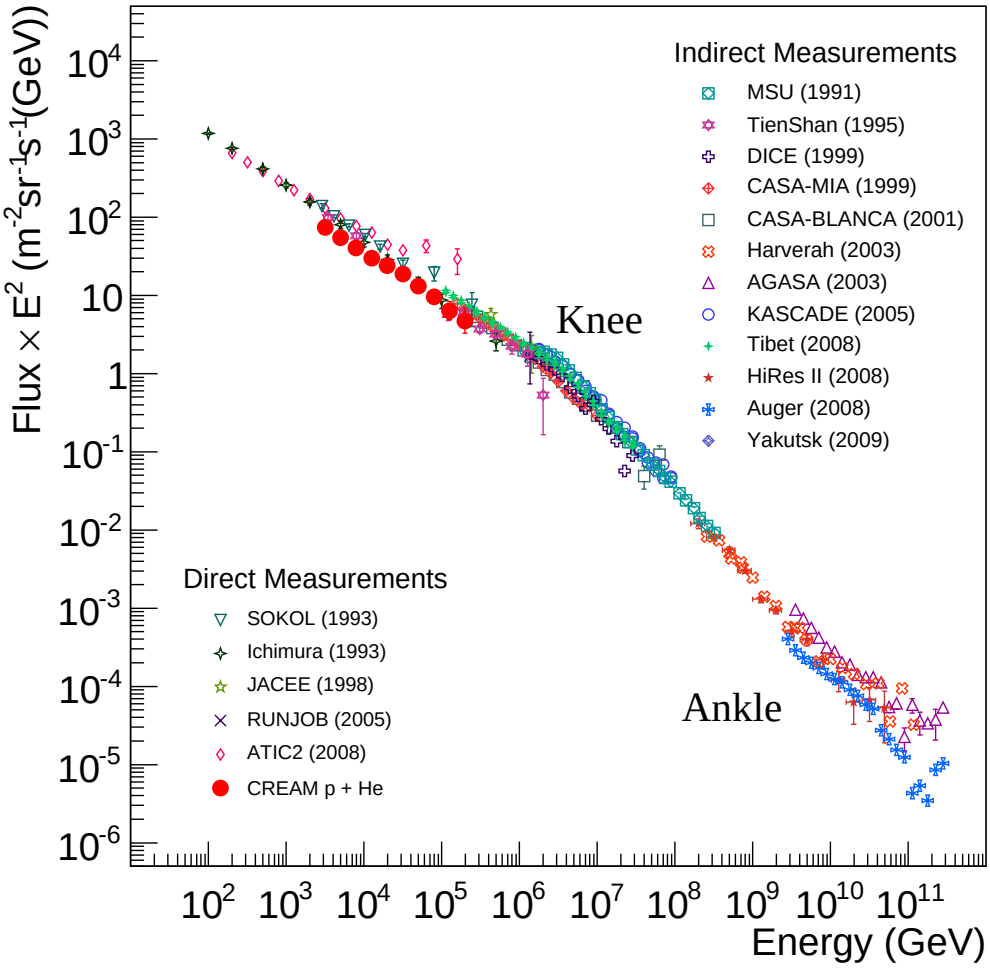

Figure 5.8: Comparison of CREAM proton plus helium spectrum with previous all-particle spectra measurements (references in Figure 1.1).

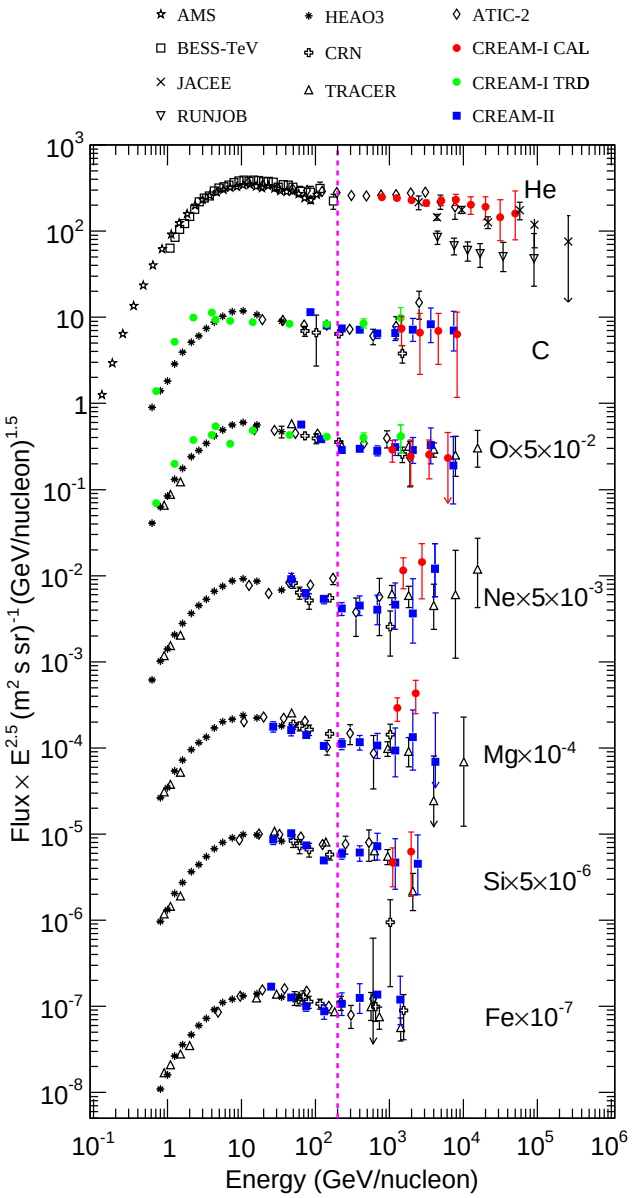

Figure 5.9: Comparison of CREAM helium and heavier nuclei spectra with previous measurements [65]. The CREAM helium spectra (red) from this analysis and heavier nuclei spectra from the calorimeter (red) and TRD (green) analysis in the first flight and calorimeter analysis in the second flight (blue) are compared with selected previous measurements: AMS, BESS, JACEE, RUNJOB, HEAO-3, CRN, TRACER, and ATIC-2. The data for elements heavier than carbon nuclei were multiplied by the indicated factors to separate their fluxes in the figure. The vertical dashed line (pink) indicates 200 GeV/nucleon.

Chapter 6

Discussion

The energy spectra of primary cosmic rays are known with good precision up to energies around 10^{11} eV, from magnetic spectrometers [42, 59, 118]. Above this energy, the composition and energy spectra were not accurately known, although there have been some pioneering measurements [57, 119, 126]. The collecting power of the CREAM calorimeter is about a factor of two larger than that of ATIC for protons and helium nuclei and, considering the much larger geometry factor of the TRD, about a factor of ten larger for heavier nuclei. The CREAM flight duration exceeds the cumulative flight time of JACEE and RUNJOB. The number of protons and helium nuclei reported in this thesis exceed the number of particles reported by either JACEE or RUNJOB [119, 127] The CREAM calorimeter is much deeper than that of either JACEE or RUNJOB, so it provides better energy measurements. CREAM also has excellent charge resolution to separate individual nuclei, whereas JACEE and RUNJOB reported elemental groups.

The observed indices were -2.66 $\pm$ 0.02 for protons from 2.5 TeV to 250 TeV and -2.58 $\pm$ 0.02 for helium nuclei from 63 TeV/nucleon to 630 GeV/nucleon. Different sources or acceleration sites as proposed in Reference [60] could be an explanation for this difference in proton and helium spectra. Most protons are likely to come from the supernova explosion of a low-mass star directly into the interstel-

lar medium. Most helium and heavier nuclei might come from the explosion of a massive star into the progenitor star's wind [60]. The stellar wind of the massive star, enriched by mass ejections that expose its deep layers, would be magnetic. The acceleration rate could be determined by the magnetic field of the progenitor's wind. The magnetic field in the progenitor's wind might be significantly higher than the magnetic field in the interstellar medium. Therefore, the spectra of helium and heavier nuclei from the progenitor's wind would be harder than the spectrum of protons from a low-mass star explosion into the interstellar medium.

As reported in Section 5.5, our measured spectra above ∼200 GeV/nucleon are harder than spectra below 200 GeV/nucleon. One possible explanation of this spectral hardening is the effect of nearby isolated supernova remnants [128]. The steady-state spectrum of cosmic rays produced by SNRs in the galaxy, with the escape length describing the propagation of cosmic rays in the leaky-box approximation, was calculated by Ptuskin *et al.*(2010) assuming that charge composition of accelerated particles was the same in all types of SNRs, except that the highest-energy part of the spectrum produced by Type Ib/c supernovae had no hydrogen. The calculated spectra showed a good overall fit to the observed all-particle spectrum up to $\sim 5 \times 10^9$ GeV, including the bending around the "knee" energy 3×10^6 GeV. The combined effect of the summation over different types of SNRs and over different types of accelerated nuclei could naturally explain the spectral features.

Another possibility for the harder spectra is the effect of distributed acceleration by multiple remnants embedded in a turbulent stellar association [129]. Most massive stars with spectral types of O and B are usually found in groups, called OB

associations. They evolve quickly and explode as supernovae in the vicinity of their parent molecular cloud. The strong stellar wind from massive stars and blast waves from supernova explosions blow large bubbles, called superbubbles. Superbubbles have been proposed as the acceleration site for Galactic cosmic rays [130,131]. Moreover, observations of heavy and ultra-heavy (Z>30) nuclei elemental abundances support the theory of cosmic-ray acceleration in OB associations [132].

A third possibility is that the spectral hardening could reflect the predicted concavity in the spectra before the "knee" [133]. In diffusive shock acceleration, particle interactions with the shock create cosmic-ray pressure. This pressure causes higher energy particles to gain energy faster and could broaden the shock transition region. The result can be spectral hardening with increasing energy and deviations from a pure power-law. The observable effect of concavity is expected to be small when summed over multiple sources and propagated over galactic distances [134], but the possible observation of concavity would be an interesting result in the cosmic-ray acceleration process.

A fourth possibility for the harder spectra above ∼200 GeV/nucleon is that the source spectra could be harder than previously thought based on the low-energy data [135]. In this case, the low energy spectrum has to steepen due to some propagation effect, such as reacceleration.

However, as shown in Figure 6.1, the boron to carbon ratios measured during the first CREAM flight [70], including all the compiled data, do not indicate changes in the propagation. Boron nuclei are produced from spallation of primary nuclei, are dominantly carbon nuclei, during the propagation in the interstellar medium.

The mean escape pathlength can be determined from measurement of the boron to carbon ratios. A typical form for the rigidity dependence of this quantity is $\lambda = \lambda_0(R/R_0)^{-\delta}$, where λ is the mean escape pathlength, R is the nucleus magnetic rigidity, and λ_0 ($\sim$10 g/cm^2) is the pathlength at the threshold rigidity R_0. In Figure 6.1, CREAM measurements of boron to carbon ratio are compared with the measurements by the HEAO-C2-3 experiment (stars) [124], and three lines that represent the results of a simple leaky-box model of cosmic-ray propagation: the dashed line uses the magnetic-rigidity dependent parameter, $\delta = 0.33$, the solid line uses $\delta = 0.6$, and the dotted line uses $\delta = 0.7$. These results show that the interstellar propagation path-length decreases rapidly with energy, with an energy dependence in the range $\delta \sim$0.5-0.6 [70]. The propagation path-length of cosmic nuclei is smaller by an order of magnitude for particles in the TeV/nucleon region, compared to those at lower energies below 10 GeV/nucleon. This path-length in the TeV/nucleon region is still large compared with the typical grammage of the Galactic disk, which is $\lesssim$ 0.002 g/cm^2. The current boron to carbon ratio data above 100 GeV/nucleon show uncertainties that are still quite large. Future flight data will reduce uncertainties at high energies where propagation models can be distinguished.

Up to now, five successful flights with 156 days of accumulated time have been completed. Although the data from the first flight were analyzed here for proton and helium spectra, Figure 6.2 shows all-particle counts from four flights as a function of the incident energy without assigning charge from the SCD. Data from the third and fourth CREAM flights indicate an energy threshold significantly lower than in

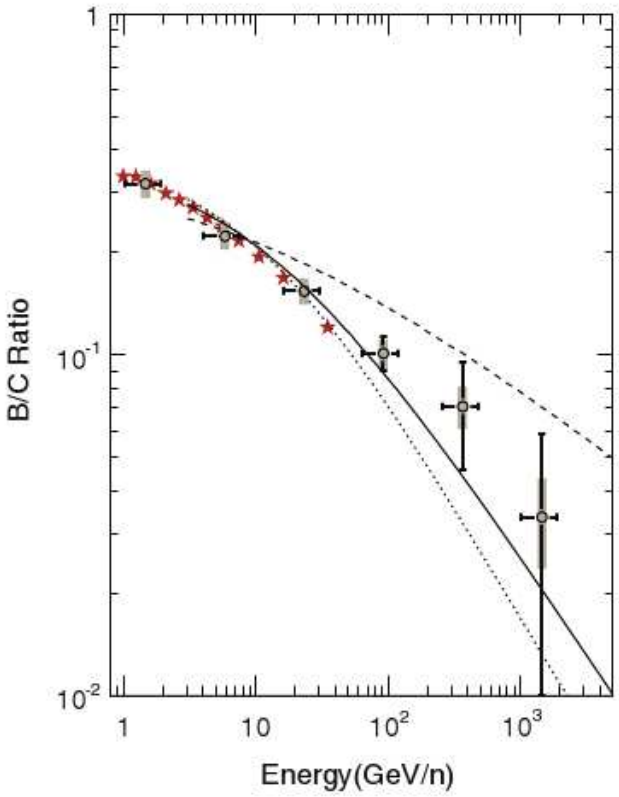

Figure 6.1: Boron to carbon ratios measured during the first CREAM flight [70]. The B/C ratios from the first CREAM flight (circles) are compared with the space experiment, HEAO-3-C2 (stars) [124]. The horizontal errors are an estimate of the systematic error in the overall energy scale. The vertical lines correspond to the statistical error of the ratio, and the gray bars show the systematic uncertainty in the ratio. The lines represent model calculations for various values of the magnetic-rigidity dependent parameter, δ, in escape from the Galaxy. The solid line, dashed line, and dotted lines represent a model with $\delta = 0.6$, $\delta = 0.333$, and $\delta = 0.7$, respectively.

the previous two fights, due to improved readout electronics [136]. The data from all four flights follow a consistent power law above the calorimeter threshold. The data from each flight will reduce the statistical uncertainties and extends the reach of measurements to energies higher than previously possible. The current energy reach of 250 TeV will be increased to 600 TeV with the accumulated data from five flights.

The CREAM experiment was planned for ULDB flights lasting about 100 days with super-pressure balloons [64]. While waiting for development of these exceptionally long flights, the CREAM instrument has flown five times on LDB flights in Antarctica. It should be noted that a 7 million cubic foot ($\sim$0.2 million cubic meters) super-pressure balloon was flown successfully for 54 days during the 2008-2009 austral summer season. As ULDB flights become available for large science payloads, long-duration exposures can be achieved faster and more efficiently with reduced payload refurbishment and launch efforts.

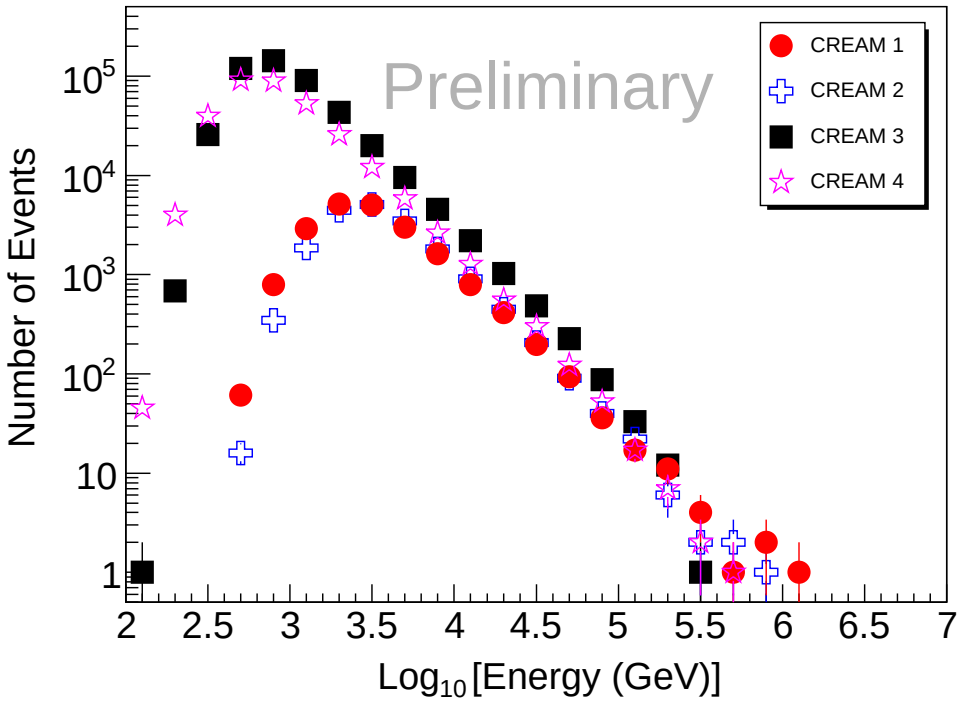

Figure 6.2: Comparison of the preliminary all-particle counts of four CREAM flights as a function of the incident energy. The calibration of the calorimeter for the third and fourth flights are not finalized yet. The preliminary incident energy of particles was estimated using the incident to deposited energy ratio from the MC simulations for each flight condition, instead of spectral deconvolution.

Bibliography

[1] V. F. Hess, "Über Beobachtungen der durchdringenden Strahlung bei sieben Freiballonfahrten (Trans. On observations of the penetrating radiation in seven balloon flights)," *Physikalische Zeitschrift* (1912) **13**, 1084.

[2] S. E. Forbush, "Three Unusual Cosmic-Ray Increases Possibly Due to Charged Particles from the Sun," *Phys. Rev.* (1946) **70**, 771.

[3] M. A. Pomerantz and S. P. Duggal, "The Sun and Cosmic Rays," *Reviews of Geophysics* (1974) **12**, 343.

[4] M. Garcia-Munoz, G. M. Mason, and J. A. Simpson, "A New Test for Solar Modulation Theory: the 1972 May-July Low-Energy Galactic Cosmic-Ray Proton and Helium Spectra," *Astrophysical Journal Letter* (1973) **182**, L81+.

[5] D. Hovestadt, O. Vollmer, G. Gloeckler, and C. Y. Fan, "Differential Energy Spectra of Low-Energy (<8.5 MeV per Nucleon) Heavy Cosmic Rays during Solar Quiet Times," *Phys. Rev. Lett.* (1973) **31**, 650.

[6] F. B. McDonald, B. J. Teegarden, J. H. Trainor, and W. R. Webber, "The Anomalous Abundance of Cosmic-Ray Nitrogen and Oxygen Nuclei at Low Energies," *Astrophysical Journal Letter* (1974) **187**, L105.

[7] L. A. Fisk, B. Kozlovsky, and R. Ramaty, "An Interpretation of the Observed Oxygen and Nitrogen Enhancements in Low-Energy Cosmic Rays," *Astrophysical Journal Letter* (1974) **190**, L35.

[8] J. R. Jokipii, "Constraints on the acceleration of anomalous cosmic rays," *Astrophysical Journal Letter* (1992) **393**, L41.

[9] K. Brecher and G. R. Burbidge, "Extragalactic Cosmic Rays," *Astrophysical Journal* (1972) **174**, 253.

[10] J. Wdowczyk and A. W. Wolfendale, "Highest energy cosmic rays," *Annu. Rev. Nucl. Part. Sci.* (1989) **39**, 43.

[11] M. Nagano and A. A. Watson, "Observations and implications of the ultrahigh-energy cosmic rays," *Rev. Mod. Phys.* (2000) **72**, 689.

[12] V. S. Berezinskii, S. V. Bulanov, V. A. Dogiel, and V. S. Ptuskin, "Astrophysics of cosmic rays," (Amsterdam: North-Holland, edited by Ginzburg, V.L., 1990).

[13] M. M. Hoppe and C. T. Russell, "Particle acceleration at planetary bow shock waves," *Nature* (1982) **295**, 41.

[14] G. P. Zank, G. Li, and O. Verkhoglyadova, "Particle Acceleration at Interplanetary Shocks," *Spa. Sci. Rev.* (2007) **130**, 255.

[15] J. R. Jokipii, "Particle acceleration at a termination shock. I - Application to the solar wind and the anomalous component," *J. of Geophys. Res.* (1986) **91**, 2929.

[16] G. F. Krymskii, "A regular mechanism for the acceleration of charged particles on the front of a shock wave," *Soviet Physics Doklady* (1977) **22**, 327. (Dokl. Akad. Nauk SSSR 234 1306-1308).

[17] W. I. Axford, E. Leer, and G. Skadron, "The acceleration of cosmic rays by shock waves," *Proc. of the 15th International Cosmic-Ray Conference, Plovdiv* (1977) vol. 11, pp. 132–137.

[18] A. R. Bell, "The acceleration of cosmic rays in shock fronts. I," *Mon. Not. R. Astron. Soc.* (1978) **182**, 147.

[19] A. R. Bell, "The acceleration of cosmic rays in shock fronts. II," *Mon. Not. R. Astron. Soc.* (1978) **182**, 443.

[20] R. D. Blandford and J. P. Ostriker, "Particle acceleration by astrophysical shocks," *Astrophysical Journal Letter* (1978) **221**, L29.

[21] P. O. Lagage and C. J. Cesarsky, "The maximum energy of cosmic rays accelerated by supernova shocks," *Astronomy & Astrophysics* (1983) **125**, 249.

[22] K. Koyama, R. Petre, E. V. Gotthelf, U. Hwang, M. Matsuura, M. Ozaki, and S. S. Holt, "Evidence for shock acceleration of high-energy electrons in the supernova remnant SN1006," *Nature* (1995) **378**, 255.

[23] G. E. Allen *et al.*, "Evidence of X-Ray Synchrotron Emission from Electrons Accelerated to 40 TeV in the Supernova Remnant Cassiopeia A," *Astrophysical Journal Letter* (1997) **487**, L97.

[24] S. LeBohec *et al.*, "Gamma-Ray Observations of the Galactic Plane at Energies E $>$ 500 GeV," *Astrophysical Journal* (2000) **539**, 209.

[25] C. D. Dermer, "Maximum Particle Energies by Fermi Acceleration in Nonrelativistic and Relativistic Flows," *Proc. of the 27th International Cosmic-Ray Conference, Hamburg* (2001) vol. 6, pp. 2039–2042.

[26] D. C. Ellison and G. Cassam-Chenaï, "Radio and X-Ray Profiles in Supernova Remnants Undergoing Efficient Cosmic-Ray Production," *Astrophysical Journal* (2005) **632**, 920.

[27] R. Enomoto *et al.*, "The acceleration of cosmic-ray protons in the supernova remnant RX J1713.7-3946," *Nature* (2002) **416**, 823.

[28] F. Aharonian *et al.* (HESS Collaboration), "Primary particle acceleration above 100 TeV in the shell-type supernova remnant RX J1713.7-3946 with deep HESS observations," *Astronomy & Astrophysics* (2007) **464**, 235.

[29] F. Aharonian *et al.* (HESS Collaboration), "A detailed spectral and morphological study of the gamma-ray supernova remnant RX J1713.7-3946 with HESS," *Astronomy & Astrophysics* (2006) **449**, 223.

[30] E. Fermi, "On the Origin of the Cosmic Radiation," *Phys. Rev.* (1949) **75**, 1169.

[31] V. S. Ptuskin and V. N. Zirakashvili, "Wind Driven by Cosmic Rays in a Rotating Galaxy. II. Propagation of Cosmic Rays," *Proc. of the 23rd International Cosmic-Ray Conference, Calgary* (1993) vol. 2, pp. 290–292.

[32] P. S. Swordy, "Expectations for Cosmic Ray Composition Changes in the Region 10^{14} to 10^{16} eV," *Proc. of the 24th International Cosmic-Ray Conference, Rome* (1995) vol. 2, pp. 697–700.

[33] H. J. Völk and V. N. Zirakashvili, "Cosmic Ray Acceleration by Spiral Shocks in the Galactic Wind," *Proc. of the 28th International Cosmic-Ray Conference, Tsukuba* (2003) vol. 4, pp. 2031–2034.

[34] W. Bednarek and R. J. Protheroe, "Contribution of nuclei accelerated by gamma-ray pulsars to cosmic rays in the Galaxy," *Astroparticle Physics* (2002) **16**, 397.

[35] Y. A. Fomin, G. B. Khristiansen, G. B. Kulikov, V. G. Pogprely, V. I. Solovjeva, V. P. Sulakov, and A. V. Trubitsyn, "Energy Spectrum of Cosmic Rays at Energies of 5×10^{15} - 5×10^{17} eV," *Proc. of the 22nd International Cosmic-Ray Conference, Durbin* (1991) vol. 2, pp. 85–88.

[36] I. P. Ivanenko *et al.*, "Energy Spectra of Cosmic Rays above 2 TeV as Measured by the SOKOL Apparatus," *Proc. of the 23rd International Cosmic-Ray Conference, Calgary* (1993) vol. 2, pp. 17–20.

[37] M. Ichimura *et al.*, "Observation of heavy cosmic-ray primaries over the wide energy range from $\sim$ 100 GeV/particle to $\sim$ 100 TeV/particle: Is the celebrated "knee" actually so prominent?" *Phys. Rev. D* (1993) **48**, 1949.

[38] R. A. Antonov *et al.*, "The new Tien-Shan Atmospheric Cerenkov Telescope (TACT). Contemporary status: all-particle spectrum measured," *Astroparticle Physics* (1995) **3**, 231.

[39] Y. Takahashi for JACEE Collaboration, "Elemental Abundance of High Energy Cosmic Rays," *Nucl. Phys. B Proc. Suppl.* (1998) **60**, 83.

[40] M. A. K. Glasmacher *et al.*, "The cosmic ray energy spectrum between 10ˆ14 and 10ˆ16 eV," *Astroparticle Physics* (1999) **10**, 291.

[41] D. Kieda and S. P. Swordy, "The Energy Spectrum in the Knee Region from DICE," *Proc. of the 26th International Cosmic-Ray Conference, Salt Lake City* (1999) vol. 3, pp. 191–194.

[42] M. Aguilar *et al.* (AMS Collaboration), "The Alpha Magnetic Spectrometer (AMS) on the International Space Station: Part I - results from the test flight on the space shuttle," *Phys. Rep.* (2002) **366**, 331.

[43] T. Sanuki *et al.*, "Precise Measurement of Cosmic-Ray Proton and Helium Spectra with the BESS Spectrometer," *Astrophysical Journal* (2000) **545**, 1135.

[44] J. W. Fowler, L. F. Fortson, C. C. H. Jui, D. B. Kieda, R. A. Ong, C. L. Pryke, and P. Sommers, "A measurement of the cosmic ray spectrum and composition at the knee," *Astroparticle Physics* (2001) **15**, 49.

[45] M. Ave, L. Cazón, J. A. Hinton, J. Knapp, J. Lloyd-Evans, and A. A. Watson, "Mass composition of cosmic rays in the range $2 \times 10^{17} - 3 \times 10^{18}$ eV measured with the Haverah Park array," *Astroparticle Physics* (2003) **19**, 61.

[46] M. Takeda *et al.*, "Energy determination in the Akeno Giant Air Shower Array experiment," *Astroparticle Physics* (2003) **19**, 447.

[47] T. Antoni *et al.*, "KASCADE measurements of energy spectra for elemental groups of cosmic rays: Results and open problems," *Astroparticle Physics* (2005) **24**, 1.

[48] V. A. Derbina *et al.*, "Cosmic-Ray Spectra and Composition in the Energy Range of 10-1000 TeV per Particle Obtained by the RUNJOB Experiment," *Astrophysical Journal Letter* (2005) **628**, L41.

[49] J. P. Wefel *et al.*, "Revised Energy Spectra for Primary Elements (H – Si) above 50 GeV from the ATIC-2 Science Flight," *Proc. of the 30th International Cosmic-Ray Conference, Merida* (2008) vol. 2, pp. 31–34.

[50] M. Amenomori *et al.*, "The All-Particle Spectrum of Primary Cosmic Rays in the Wide Energy Range from 10^{14} to 10^{17} eV Observed with the Tibet-III Air-Shower Array," *Astrophysical Journal* (2008) **678**, 1165.

[51] R. U. Abbasi *et al.*, "First Observation of the Greisen-Zatsepin-Kuzmin Suppression," *Phys. Rev. Lett.* (2008) **100**, 101101.

[52] J. Abraham *et al.*, "Observation of the Suppression of the Flux of Cosmic Rays above 4×10^{19} eV," *Phys. Rev. Lett.* (2008) **101**, 061101.

[53] A. A. Ivanov, S. P. Knurenko, and I. Y. Sleptsov, "Measuring extensive air showers with Cherenkov light detectors of the Yakutsk array: the energy spectrum of cosmic rays," *New J. Phys.* (2009) **11**, 065008.

[54] M. Amenomori *et al.*, "Anisotropy and Corotation of Galactic Cosmic Rays," *Science* (2006) **314**, 439.

[55] A. A. Abdo *et al.*, "Discovery of Localized Regions of Excess 10-TeV Cosmic Rays," *Physical Review Letters* (2008) **101**, 221101.

[56] R. Abbasi *et al.*, "Measurement of the Anisotropy of Cosmic-ray Arrival Directions with IceCube," *Astrophysical Journal Letter* (2010) **718**, L194.

[57] D. Müller, S. P. Swordy, P. Meyer, J. L'Heureux, and J. M. Grunsfeld, "Energy spectra and composition of primary cosmic rays," *Astrophysical Journal* (1991) **374**, 356.

[58] A. D. Panov *et al.*, "Energy spectra of abundant nuclei of primary cosmic rays from the data of ATIC-2 experiment: Final results," *Bull. Rus. Acad. Sci. Phys.* (2009) **73**, 564.

[59] M. Boezio *et al.*, "The cosmic-ray proton and helium spectra measured with the CAPRICE98 balloon experiment," *Astroparticle Physics* (2003) **19**, 583.

[60] P. L. Biermann, "Cosmic rays. 1. The cosmic ray spectrum between 10^4 GeV and 3×10^9 GeV," *Astronomy & Astrophysics* (1993) **271**, 649.

[61] B. Wiebel-Sooth, P. L. Biermann, and H. Meyer, "Cosmic rays. VII. Individual element spectra: prediction and data," *Astronomy & Astrophysics* (1998) **330**, 389.

[62] J. R. Hörandel, "On the knee in the energy spectrum of cosmic rays," *Astroparticle Physics* (2003) **19**, 193.

[63] E. Seo *et al.*, "CREAM: 70 days of flight from 2 launches in Antarctica," *Advanves in Space Research* (2008) **42**, 1656.

[64] W. V. Jones *et al.*, "Ultra Long Duration Ballooning Technology Development," *Proc. of the 29th International Cosmic-Ray Conference, Pune* (2005) vol. 3, pp. 405–408.

[65] H. S. Ahn *et al.*, "Discrepant Hardening Observed in Cosmic-ray Elemental Spectra," *Astrophysical Journal Letter* (2010) **714**, L89.

[66] P. Maestro *et al.*, "Energy cross-calibration from the first CREAM flight: transition radiation detector versus calorimeter," *Proc. of the 30th International Cosmic-Ray Conference, Merida* (2007) vol. 2, p. 333.

[67] E. Seo *et al.*, "Cosmic-ray energetics and mass (CREAM) balloon project," *Advanves in Space Research* (2004) **33**, 1777.

[68] H. S. Ahn *et al.*, "The Cosmic Ray Energetics And Mass (CREAM) instrument," *Nucl. Instrum. Methods Phys. Res. A* (2007) **579**, 1034.

[69] H. S. Ahn *et al.*, "The Cosmic Ray Energetics and Mass (CREAM) timing charge detector," *Nucl. Instrum. Methods Phys. Res. A* (2009) **602**, 525.

[70] H. S. Ahn *et al.*, "Measurements of cosmic-ray secondary nuclei at high energies with the first flight of the CREAM balloon-borne experiment," *Astroparticle Physics* (2008) **30**, 133.

[71] I. H. Park *et al.*, "Heavy ion beam test results of the silicon charge detector for the CREAM cosmic ray balloon mission," *Nucl. Instrum. Methods Phys. Res. A* (2004) **535**, 158.

[72] E. Seo *et al.* for the CREAM Collaboration, "The Record Breaking 42-day Balloon Flight of CREAM," *Proc. of the 29th International Cosmic-Ray Conference, Pune* (2005) vol. 3, p. 101.

[73] R. Wigmans, "Calorimetry: Energy measurement in particle physics," *Int. Ser. Monogr. Phys.* (2000) **107**, 1.

[74] C. Amsler *et al.* Particle Data Group, "Review of Particle Physics," *Phys. Lett. B* (2008) **667**, 1.

[75] O. Ganel, E. Seo, and Z. Wang, "On the Use of Low-Z Targets in Space-Based Hadron Calorimetry," *Proc. of the 26th International Cosmic-Ray Conference, Salt Lake* (1999) vol. 5, pp. 33–36.

[76] Y. S. Yoon *et al. Astrophysical Journal* (2010) Submitted.

[77] Lutz, L., "CREAM Housekeeping System Description," *Tech. rep.*, Institute of Physical Science and Technoledge, University of Maryland (2003).

[78] L. D. Thompson and D. W. Stuchlik, "Balloon support systems performance for the cosmic rays energetics and mass mission," *Advanves in Space Research* (2008) **42**, 1698.

[79] E. Seo *et al.*, "Approaching the Knee with Direct Measurements," *Nucl. Phys. B Proc. Suppl.* (2007) **175**, 155.

[80] "Historical SWP Products from 1996," SWPC Anonymous FTP Server (2005) `http://www.swpc.noaa.gov/ftpmenu/warehouse/2005/2005_plots.html`.

[81] Y. Yoon *et al.*, "CREAM Observation of January 20th Solar Flare," (2005) pp. A314+. AGU Fall Meeting Abstracts.

[82] H. S. Ahn *et al.*, "Elemental Spectra from the CREAM-I Flight," *Proc. of the 30th International Cosmic-Ray Conference, Merida* (2007) vol. 2, pp. 63–66.

[83] N. H. Park *et al.*, "Effect of albedo particles on charge measurement," *Proc. of the 30th International Cosmic-Ray Conference, Merida* (2007) vol. 2, p. 381.

[84] M. H. Lee *et al.*, "The CREAM Calorimeter: Performance In Tests And Flights," *Calorimetry in High Energy Physics: XII*, S. R. Magill & R. Yoshida, ed. (2006) vol. 867 of *AIP Conf. Ser.*, pp. 167–174.

[85] R. Brun, "GEANT User Guide," (1984) CERN DD/EE/84-1, Geneva.

[86] A. Fasso, A. Ferrari, J. Ranft, and P. R. Sala, "FLUKA: Present status and future developments," *Proc. IV Int. Conf. on Calorimetry in High Energy Physics, La Biodola, Italy, 21-26 September 1993*, A. Menzione and A. Scribano, eds. (World Scientific, 1993) (1993) pp. 493–502.

[87] M. H. Lee, Y. S. Yoon, and T.-G. Kang, "Calorimeter calibration and analysis status for CREAM 2004 flight data at UMD," CREAM Collaboration Meeting June 13th, 2005 (Presentation) (2005) .

[88] Y. S. Yoon *et al.*, "Calibration of the CREAM-I calorimeter," *Proc. of the 30th International Cosmic-Ray Conference, Merida* (2007) vol. 2, pp. 421–424.

[89] H. S. Ahn *et al.*, "Performance of CREAM Calorimeter: Results of Beam Tests," *Nucl. Phys. B Proc. Suppl.* (2006) **150**, 272.

[90] P. S. Marrocchesi *et al.*, "Construction and test of a scintillator hodoscope for the CREAM experiment," *Nucl. Phys. B Proc. Suppl.* (2004) **134**, 75.

[91] H. S. Ahn *et al.*, "Energy Spectra of Cosmic-ray Nuclei at High Energies," *Astrophysical Journal* (2009) **707**, 593.

[92] J. Buckley, J. Dwyer, D. Müller, S. Swordy, and K. K. Tang, "A new measurement of the flux of the light cosmic-ray nuclei at high energies," *Astrophysical Journal* (1994) **429**, 736.

[93] H. S. Ahn *et al.*, "The energy spectra of protons and helium measured with the ATIC experiment," *Advanves in Space Research* (2006) **37**, 1950.

[94] H. J. Kim *et al.*, "Simulation of the ion interactions for the ATIC experiment," *Proc. of the 26th International Cosmic-Ray Conference, Salt Lake City* (1999) vol. 1, pp. 17–25.

[95] J. Z. Wang *et al.*, "Space based calorimeters: Heavy ion simulations," *Proc. of the 27th International Cosmic-Ray Conference, Hamburg* (2001) vol. 4, pp. 1445–1448.

[96] B. Andersson, G. Gustafson, and H. Pi, "The FRITIOF model for very high energy hadronic collisions," *Z. Phys. C Part. Fields* (1993) **57**, 485.

[97] H. Sorge, "Flavor production in Pb(160A GeV) on Pb collisions: Effect of color ropes and hadronic rescattering," *Phys. Rev. C* (1995) **52**, 3291.

[98] J. Ranft, "Dual parton model at cosmic ray energies," *Phys. Rev. D* (1995) **51**, 64.

[99] A. Ferrari, J. Ranft, S. Roesler, and P. R. Sala, "The production of residual nuclei in peripheral high energy nucleus-nucleus interactions," *Z. Phys. C Part. Fields* (1996) **71**, 75.

[100] J. D. Sullivan, "Geometrical factor and directional response of single and multi-element particle telescopes," *Nucl. Instrum. Methods* (1971) **95**, 5.

[101] G. R. Thomas and D. M. Willis, "Analytical derivation of the geometric factor of a particle detector having circular or rectangular geometry," *J. Phys. E Sci. Instrum.* (1972) **5**, 260.

[102] F. A. Hagen, A. J. Fisher, and J. F. Ormes, "Be-10 abundance and the age of cosmic rays - A balloon measurement," *Astrophysical Journal* (1977) **212**, 262.

[103] W. R. Webber, J. C. Kish, and D. A. Schrier, "Total charge and mass changing cross sections of relativistic nuclei in hydrogen, helium, and carbon targets," *Phys. Rev. C* (1990) **41**, 520.

[104] P. Papini, C. Grimani, and S. A. Stephens, "An estimate of the secondary-proton spectrum at small atmospheric depths," *Nuovo Cimento C* (1996) **19**, 367.

[105] Y. Kawamura *et al.*, ""Quasidirect" observations of cosmic-ray primaries in the energy region 10^{12}-10^{14} eV," *Phys. Rev. D* (1989) **40**, 729.

[106] K. Abe *et al.*, "Measurements of proton, helium and muon spectra at small atmospheric depths with the BESS spectrometer," *Phys. Lett. B* (2003) **564**, 8.

[107] G. D. Lafferty and T. R. Wyatt, "Where to stick your data points: The treatment of measurements within wide bins," *Nucl. Instrum. Methods Phys. Res. A* (1995) **355**, 541.

[108] G. J. Feldman and R. D. Cousins, "Unified approach to the classical statistical analysis of small signals," *Phys. Rev. D* (1998) **57**, 3873.

[109] J. R. Taylor, "Introduction to Error Analysis," (University Science Books, 1997), second edition.

[110] F. James and M. Roos, "Minuit - a system for function minimization and analysis of the parameter errors and correlations," *Computer Physics Communications* (1975) **10**, 343.

[111] F. James and M. Winkler `http://www.cern.ch/minuit` (2004) CERN.

[112] F. James and M. Winkler, "MINUIT User's Guide," (2004) CERN manual, Geneva.

[113] F. James, "MINUIT Tutorial," (2004) Repring from the Proceeding of the 1972 CERN Computing and Data Processing School, 1972 (CERN 72-21).

[114] R. Fletcher and R. Mead, "A new approach to variable metric algorithms," *Comput. J.* (1970) **13**, 317.

[115] J. Nelder and R. Mead, "A Simplex Method for Function Minimization," *Comput. J.* (1965) **7**, 308.

[116] F. James, "The Interpretation of Errors," (2004) CERN manual, Geneva.

[117] A. A. Goldstein and J. F. Price, "On Descent from Local Minima," *Math. Comput.* (1971) **25**, 569.

[118] S. Haino *et al.*, "Measurements of primary and atmospheric cosmic-ray spectra with the BESS-TeV spectrometer," *Phys. Lett. B* (2004) **594**, 35.

[119] K. Asakimori *et al.*, "Cosmic-Ray Proton and Helium Spectra: Results from the JACEE Experiment," *Astrophysical Journal* (1998) **502**, 278.

[120] T. Li and Y. Ma, "Analysis methods for results in gamma-ray astronomy," *Astrophysical Journal* (1983) **272**, 317.

[121] M. Boezio *et al.*, "The Cosmic-Ray Proton and Helium Spectra between 0.4 and 200 GV," *Astrophysical Journal* (1999) **518**, 457.

[122] K. Asakimori *et al.* JACEE Collaboration, "Cosmic Ray Composition and Spectra: (II) Helium and Z>2," *Proc. of the 23rd International Cosmic-Ray Conference, Calgary* (1993) vol. 2, pp. 25–29.

[123] E. Seo, J. F. Ormes, R. E. Streitmatter, S. J. Stochaj, W. V. Jones, S. A. Stephens, and T. Bowen, "Measurement of cosmic-ray proton and helium spectra during the 1987 solar minimum," *Astrophysical Journal* (1991) **378**, 763.

[124] J. J. Engelmann, P. Ferrando, A. Soutoul, P. Goret, and E. Juliusson, "Charge composition and energy spectra of cosmic-ray nuclei for elements from Be to NI - Results from HEAO-3-C2," *Astronomy & Astrophysics* (1990) **233**, 96.

[125] M. Ave, P. J. Boyle, F. Gahbauer, C. Höppner, J. R. Hörandel, M. Ichimura, D. Müller, and A. Romero-Wolf, "Composition of Primary Cosmic-Ray Nuclei at High Energies," *Astrophysical Journal* (2008) **678**, 262.

[126] A. V. Apanasenko *et al.* (RUNJOB Collaboration), "Composition and energy spectra of cosmic-ray primaries in the energy range 10^{13}-10^{15} eV/particle observed by Japanese-Russian joint balloon experiment," *Astroparticle Physics* (2001) **16**, 13.

[127] V. Kopenkin and T. Sinzi, "Cosmic ray primary composition in the energy range 10-1000TeV obtained by passive balloon-borne detector: Reanalysis of the RUNJOB experiment," *Phys. Rev. D* (2009) **79**, 072011.

[128] V. Ptuskin, V. Zirakashvili, and E. Seo, "Spectrum of Galactic Cosmic Rays Accelerated in Supernova Remnants," *Astrophysical Journal* (2010) **718**, 31.

[129] G. A. Medina-Tanco and R. Opher, "Spatial and temporal distributed acceleration of cosmic rays by supernova remnants three-dimensional simulations," *Astrophysical Journal* (1993) **411**, 690.

[130] W. I. Axford, "Acceleration of Cosmic Rays by Shock Waves," *Proc. of the 17th International Cosmic-Ray Conference, Paris* (1981) vol. 12, pp. 155–+.

[131] Y. M. Butt and A. M. Bykov, "A Cosmic-Ray Resolution to the Superbubble Energy Crisis," *Astrophysical Journal Letter* (2008) **677**, L21.

[132] W. R. Binns *et al.*, "OB Associations, Wolf Rayet Stars, and the Origin of Galactic Cosmic Rays," *Spa. Sci. Rev.* (2007) **130**, 439.

[133] D. C. Ellison, E. G. Berezhko, and M. G. Baring, "Nonlinear Shock Acceleration and Photon Emission in Supernova Remnants," *Astrophysical Journal* (2000) **540**, 292.

[134] G. E. Allen, J. C. Houck, and S. J. Sturner, "Evidence of a Curved Synchrotron Spectrum in the Supernova Remnant SN 1006," *Astrophysical Journal* (2008) **683**, 773.

[135] A. M. Hillas, "TOPICAL REVIEW: Can diffusive shock acceleration in supernova remnants account for high-energy galactic cosmic rays?" *J. Phys. G Nucl. Phys.* (2005) **31**, 95.

[136] M. H. Lee *et al.*, "The CREAM-III Calorimeter," *Proc. of the 30th International Cosmic-Ray Conference, Merida* (2007) vol. 2, pp. 409–412.